

TECHNICAL UNIVERSITY OF CRETE

*Statistical Analysis of Seismic
Sequence Data from the Island
of Zakynthos for the Time
Period 2016-2019*

Author:

Michaela-Natalia
VASILEIADI

Supervisor:

Prof. Dionissios
HRISTOPULOS

*A thesis submitted in fulfillment of the requirements
for the degree of M.Sci*

in the

Geostatistics Laboratory
School of Mineral Resources Engineering

August 31, 2020

“I think it is much more interesting to live with uncertainty than to live with answers that might be wrong. ”

Richard Feynman

Acknowledgements

Firstly, I would like to express my deep gratitude to my advisor Prof. Dionissios Hristopoulos for the continuous support of my study and related research, for his patience, motivation, and immense knowledge. His guidance helped me in all the time of research and writing of this thesis. I could not have imagined having a better advisor and mentor for my diploma thesis. Without his guidance and constant feedback, this thesis would not have been achievable.

Besides my advisor, I would like to thank the rest of my thesis committee: Dr. Vasiliki Mouslopoulou, Prof. Antonios Vafeidis, for their invaluable advice and insightful comments.

I have also been fortunate to have a great group of friends at the Technical University of Crete. This includes my lab-mates in Geostatistics Laboratory in the School of Mineral Resources Engineering, Dr. Andrew Pavlides and Panagiota Gkafa. Thank you for helping me make this work possible. Especially, i would like to express my gratitude to Vasiliki Agou. I have learned so much from you. Your constructive criticism and collaboration have been tremendous assets throughout my study. Thank you for the moral support but also for all the fun we have had together.

I would also like to acknowledge the staff working in the National Observatory of Athens for their work on collecting and processing the seismic data used in this dissertation.

I would also like to thank Vasilis Politis for inspiring me and helping me get past all the self-doubting that inevitably crops up in the course of a Master of Science (M.Sci.). You're the first person I turn to in good times and in bad. You have given me the courage to make the next transitions in my life. For all of this, I thank you.

Last but not least, I would like to express my very profound gratitude to my mother, father and sister. Thank you for the constant support and love you have given me from childhood to now, encouragement throughout my years of studies and through the process of researching and writing this thesis ...

Contents

Acknowledgements	iii
Εκτεταμένη Περίληψη	1
1 Introduction	11
1.1 Motivation	11
1.2 Data and Study Area	12
2 Statistical Methods in Seismology	17
2.1 Probability Distributions	17
2.1.1 Poisson-distribution	17
2.1.2 The Normal Distribution	18
Skewness	19
Kurtosis	20
2.1.3 The Gamma Distribution	20
Skewness	20
Median	20
2.1.4 Weibull Distribution	22
2.1.5 Generalized Pareto Distribution (GPD)	24
2.1.6 Exponential Distribution	25
2.1.7 Log-normal Distribution	27
2.2 Cross-Validation Error Measures	29
2.3 Linear Regression	32
2.3.1 Ordinary Least Squares (OLS)	32
2.3.2 Weighted Least Squares (WLS)	33
2.4 Bootstrapping	33
2.5 Maximum Likelihood Method	34
2.5.1 Information Criteria	34
2.6 Statistical Methods Used to Estimate the Magnitude of Completeness.	35
2.6.1 Maximum Curvature (MAXC)	36
2.6.2 Goodness-of-fit (GFF)	36
2.6.3 Entire Magnitude Range (EMR)	36
2.7 Statistical Properties and Measurement of Earthquakes	37
2.7.1 Seismograph, Seismogram and Seismometer	37
2.7.2 Energy Release	38
2.7.3 Intensity	40

3	Empirical Relations and Laws of Seismology	41
3.1	The Concept of Magnitude and its Different Scales	41
3.1.1	Local Magnitude, M_L	41
3.1.2	Different Scales of Magnitude	43
	Moment Magnitude, M_w	43
	Seismic Moment, M_o	44
	Surface and Body Wave Magnitude, M_s and m_b	45
3.1.3	Saturation on Magnitude Scales	46
3.2	Law of Seismology	47
3.2.1	Gutenberg-Richter Law	47
3.2.2	Omori-Utsu Law	48
3.2.3	The ETAS Model	52
3.2.4	Bath Law	53
4	Statistical Analysis of Earthquake Magnitude	55
4.1	Empirical Relation Between Local and Moment Magnitudes	56
4.1.1	Estimates of Moment Magnitude	61
4.1.2	Estimates of Seismic Moment	62
5	Statistical Analysis of Earthquake Frequency	65
5.1	Determination of the Magnitude of Completeness	65
5.2	Estimation of b-value	68
5.2.1	Plots of Estimated b-value for Earthquakes Prior to the Main Event	71
5.2.2	Plots of Estimated b-value for Aftershock Sequence	75
6	Interevent Times Probability Distribution	79
6.1	Interevent Times Probability Distribution For earthquakes before the main event	80
6.2	Interevent Times Probability Distribution For Aftershocks	83
7	Analysis of Aftershock Frequency	87
7.1	Implementation of the Omori Law	87
7.2	Estimation of Omori-Utsu (O-U) Parameters	89
7.3	Investigation of O-U parameters	90
7.3.1	Dependence of O-U Parameters on M_c	90
7.3.2	Dependence of O-U Parameters over time	95
7.3.3	Comparison of O-U Parameters with Kefalonia and Lefkada	97
8	Conclusions and Future Directions	99
9	Appendix	103

List of Figures

1	To νησί της Ζακύνθου.	1
1.1	The 2018 Zakynthos earthquake sequence. Foreshock Mw 4.8 (yellow star and focal mechanism plot), mainshock epicenter (green star), centroid moment tensor (CMT; green square and focal mechanism plot), and activity in the first 24 hr, superimposed on bathymetry. The Cephalonia transform fault (CTF) and the subduction backstop (SBS) are shown. Three characteristic plate-velocity vectors are included. Retrieved from [73].	13
1.2	(A) Simplified map of Greece showing the Hellenic trench, the major fault systems and the study area Zakynthos Island and (B) map of western Greece with the main fault systems and the Ionian Island Zakynthos, Kefalonia and Lefkada. Retrieved from [4].	14
1.3	The results of the catastrophic earthquake in Zakynthos, 1953. Retrieved from [62]	15
1.4	Space distribution of earthquakes 2011–2018 (until the 2018 mainshock). The centroids of significant earthquakes southwest of Zakynthos, in 1997 [40], 2006 [70], and 2018 [73], occurred near two localized clusters.	16
2.1	Plot of the probability density function for the Normal Distribution.	19
2.2	Plot of the cumulative distribution function for the Normal Distribution.	19
2.3	Plot of the probability density function for the Gamma Distribution.	21
2.4	Plot of the cumulative distribution function for the Gamma Distribution.	22
2.5	Plot of the probability density function for the Weibull Distribution.	23
2.6	Plot of the cumulative distribution function for the Weibull Distribution.	23
2.7	Plot of the probability density function for the Paareto Distribution.	24
2.8	Plot of the cumulative distribution function for the Pareto Distribution.	25
2.9	Plot of the probability density function for the Exponential Distribution.	26

2.10	Plot of the cumulative distribution function for the Exponential Distribution.	27
2.11	Plot of the probability density function for the Log-Normal Distribution.	28
2.12	Plot of the cumulative distribution function for the Log-Normal Distribution.	29
2.13	Seismograph an instrument which detects and records ground motion (and especially vibrations due to earthquakes) along with timing information. Retrieved from [52].	38
2.14	Correlation between the number of earthquakes and their magnitude with an energy release equivalent (in kg of TNT). Downloaded from [29]. The right side of the figure represents the amount of high explosive (TNT) required to produce the energy released by the earthquake. Equally, the left side of the figure illustrates the magnitude scale, which is determined by the amount of energy released at the hypocenter.	39
3.1	Charles Richter with his seismograph, 1976 Caltech.	41
3.2	Procedure for calculating the magnitude. Connecting the amplitude of the seismic wave (shown on the right) with distances calculated from S minus P arrival times gives us the Richter's magnitude scale. The scale is logarithmic, which means that one increase in magnitude correspond to ten times larger amplitude. Retrieved from [66]	42
3.3	Saturation of moment magnitude, surface and body wave magnitudes. Retrieved from [66]	46
3.4	Plots of Gutenberg Richter law that show the impact of different b-values. Retrieved from [20].	48
3.5	Frequency of Earthquakes at Gifu, Japan (1890-1893). The first curve represents the monthly earthquake frequency, the second curve the 12 hours earthquake frequency and the third curve represents the yearly earthquake frequency. Retrieved from [58].	49
3.6	The top figure shows the decay of the occurrence rate of recorded shocks at Gifu (Japan), using Omori's data from October 28, 1891 (0.474 days after the main shock) until December 31, 1899. The bottom figure is a graph of the cumulative number of felt shocks using the same sets of data. The curves at the top and bottom figures represent the Omori formula and its integrated form fitted to the data from the reported period [58].	51
4.1	Plot of the cumulative number of earthquakes with magnitude greater and equal to 1.0 M_L , from 2016 to 2019. The bluish-green line corresponds to the earthquakes in Zakynthos, while the red circle represents the main event.	56

4.2	Scatter plot of the relationship between local magnitude and moment magnitude values obtained for the period from 2009 to 2019. The moment magnitude was obtained by means of weighted linear regression according to the Eq. (4.1). The bluish-green symbols (crosses) correspond to the local and moment magnitude values; the solid red line denotes the optimal fit, and the red dashed lines denote the confidence bounds.	59
4.3	Plot of the converted moment magnitude, M_w during a period of 3 years from 2016 to 2019. The conversion was carried out according to Eq. (4.1). The bluish-green circles represent the 11778 earthquake events and the big red circle corresponds to the main earthquake of Zakynthos, in 25/10/2018. The red dashed line divide the earthquakes to the before the main shock sequence and to the aftershock sequence.	62
4.4	Plot of cumulative seismic moment release, measured in dyn·cm and calculated from the empirical Eq. (4.5). The bluish-green circles represent the cumulative number of the earthquakes during the period from 2016 to 2019. The red circle stands for the main event.	64
5.1	Plot of the relationship between the b-value and the M_c for all the earthquakes. The solid blue line (on the left) illustrate that relationship for the foreshocks, while the solid purple line (on the right) illustrates the same relationship but for the aftershocks.	67
5.2	Evolution of the b-value over time before the main shock. The 6 th cluster refers to the period from April 2017 to July 2017, the 7 th cluster lasts from August 2017 until December 2017, the 8 th cluster last from January 2018 until May 2018 and the 9 th cluster starts from June and ends at September 2018.	69
5.3	Histogram of probability density function versus event magnitude for foreshocks, using logarithmic vertical scale.	72
5.4	Histogram of the number of foreshocks per magnitude and fit to the optimal exponential (GR curve).	73
5.5	Histogram of probability density function versus event magnitude for foreshocks, without main event, using logarithmic vertical scale.	74
5.6	Histogram of the number of foreshocks without the main shock of 6.6 M_L per magnitude and fit to the optimal exponential (GR curve).	74
5.7	Histogram of probability density function versus event magnitude for aftershocks, using logarithmic vertical scale.	75
5.8	Histogram of the number of aftershocks per magnitude and fit to the optimal exponential (GR curve).	76

5.9	Histogram of probability density function versus event magnitude for aftershocks, without main event, using logarithmic vertical scale.	77
5.10	Histogram of the number of aftershocks without the main shock of 6.6 M_L per magnitude and fit to the optimal exponential (GR curve).	77
6.1	Histogram of time intervals between earthquakes before the main event. Time intervals are being calculated using in minutes.	80
6.2	All distributions fitting our data. Red colour refers to Weibull distribution, yellow to gamma, blue to Pareto, black to exponential and pink to lognormal.	81
6.3	Fit of the interevent times of the earthquakes before the main event sequence to the Weibull distribution. Top left: Density histogram of the data and fit to the Weibull PDF. Top right: quantile-quantile plot. Bottom left: Cumulative distribution function. Bottom right: P-P plot.	82
6.4	Histogram of interval times between aftershocks. Time intervals are expressed in minutes.	83
6.5	Fit of the interevent times of the aftershock sequence for the five different distributions. Top left: Density histogram of the data and fit to the Weibull PDF. Top right: quantile-quantile plot. Bottom left: Cumulative distribution function. Bottom right: P-P plot. Red colour refer to Weibull distribution, yellow to gamma, blue to Pareto, black to exponential and pink to lognormal.	84
6.6	Fit of the interevent times of the aftershock sequence to the Pareto distribution. Top left: Density histogram of the data and fit to the Pareto PDF. Top right: quantile-quantile plot. Bottom left: Cumulative distribution function. Bottom right: P-P plot.	86
7.1	The decreasing rate of aftershocks since the main shock on 25, October 2018. The bluish-green circles represent the amount of earthquake events with magnitude greater than 2.5 M_L , which happened per day. The aftershock sequence in this study lasts for 220 days after the main shock.	88
7.2	Estimated Omori-Utsu Law parameters (p , c , k) for the aftershock sequence. Observed versus predicted data in Zakynthos.	89
7.3	Maximum likelihood estimates of the parameters of the modified Omori formula for the aftershocks of the 1993 Hokkaido-Nansei-Oki earthquake for various cutoff magnitudes. Retrieved from Utsu [78].	91

7.4	Dependence on p parameter with magnitude of completeness M_c . The 4.4 M_c include 22 events, while 1.8 M_c , 2 M_c and 2.2 M_c include 8541, 7423, 6111 events, respectively.	93
7.5	Dependence on c parameter with magnitude of completeness.	94
7.6	Dependence on k parameter with magnitude of completeness. With the increase in the values of M_c , fewer aftershocks are included in the formula. For 4.4 M_c we use 22 events.	94
7.7	The evolution of p , c and k parameters over time. Time window of 20 days was used.	96
9.1	Histogram of probability density function versus event magnitude for aftershocks (without main event), using logarithmic vertical scale. $M_c = 3.5$	104
9.2	Histogram of the number of aftershocks without the main shock of 6.6 M_L per magnitude and fit to the optimal exponential (GR curve). $M_c = 3.5$	105
9.3	Fit of the interevent times of the earthquakes before the main event to the Gamma distribution. Top left: Density histogram of the data and fit to the Gamma PDF. Top right: quantile-quantile plot. Bottom left: Cumulative distribution function. Bottom right: P-P plot.	106
9.4	Fit of the interevent times of the earthquakes before the main event to the Pareto distribution. Top left: Density histogram of the data and fit to the Pareto PDF. Top right: quantile-quantile plot. Bottom left: Cumulative distribution function. Bottom right: P-P plot.	107
9.5	Fit of the interevent times of the earthquakes before the main event to the Exponential distribution. Top left: Density histogram of the data and fit to the Exponential PDF. Top right: Quantile-quantile plot. Bottom left: Cumulative distribution function. Bottom right: P-P plot.	108
9.6	Fit of the interevent times of the earthquakes before the main event to the Lognormal distribution. Top left: Density histogram of the data and fit to the Lognormal PDF. Top right: quantile-quantile plot. Bottom left: Cumulative distribution function. Bottom right: P-P plot.	109
9.7	Fit of the interevent times of the aftershock sequence to the Weibull distribution. Top left: Density histogram of the data and fit to the Weibull PDF. Top right: quantile-quantile plot. Bottom left: Cumulative distribution function. Bottom right: P-P plot.	110
9.8	Fit of the interevent times of the aftershock sequence to the Gamma distribution. Top left: Density histogram of the data and fit to the Gamma PDF. Top right: quantile-quantile plot. Bottom left: Cumulative distribution function. Bottom right: P-P plot.	111

- 9.9 Fit of the interevent times of the aftershock sequence to the Exponential distribution. Top left: Density histogram of the data and fit to the Exponential PDF. Top right: quantile-quantile plot. Bottom left: Cumulative distribution function. Bottom right: P-P plot. 112
- 9.10 Fit of the interevent times of the aftershock sequence to the Lognormal distribution. Top left: Density histogram of the data and fit to the Lognormal PDF. Top right: quantile-quantile plot. Bottom left: Cumulative distribution function. Bottom right: P-P plot. 113

List of Tables

3.1	Symbols used to indicate different magnitudes.	43
4.1	Dates and coordinates for the 55 earthquake occurrences (2009–2019) used to establish the relation between local and moment magnitude scales.	57
4.2	Cross validation performance measures calculated for the WLS estimations ($y = \alpha \cdot x + \beta$) for 55 seismic events.	60
4.3	Error measures of the estimated M_w based on Eq. (4.1) versus the recorded M_w	61
5.1	Estimation of the magnitude of completeness M_c , based on three different methodologies, the MAXC, the GFF, and the EMR, with and without Bootstrapping. For the earthquakes before the main event.	66
5.2	Estimation of the magnitude of completeness M_c , based on three different methodologies, the MAXC, the GFF, and the EMR, with and without Bootstrapping. For the earthquakes after the main event.	67
5.3	Estimated b-value parameters for the foreshocks using the maximum likelihood method. The M_c is the magnitude of completeness, b stands for the Gutenberg-Richter exponent, hbint, and lbint represents the upper and the lower confidence bound for the G-R exponent, respectively. The symbol b10 stands for the G-R exponent (base 10) and hbint10, and lint10 the corresponding confidence bounds for the G-R exponent (base 10). The bold font distinguishes the M_c and the b-value used for further analysis. Graphical representation shown in Fig. 5.1.	70
5.4	Estimated b-value parameters for the aftershocks using the maximum likelihood method. The symbols are described in Table 5.3.	70
6.1	Akaike Information Criterion and Bayesian Information Criterion for the earthquakes before the main event calculated according to Eq.(2.18) and Eq.(2.19) respectively. According to the AIC and BIC criteria the best distribution model for the earthquakes before the main event is the Weibull distribution.	81
6.2	Fitting of the Weibull distribution by means of maximum likelihood	82

6.3	Akaike Information Criterion and Bayesian Information Criterion for the aftershocks calculated according to Eq. (2.18) and Eq. (2.19) respectively. According to the AIC and BIC criteria, the best distribution model for the aftershocks is the Pareto distribution.	85
6.4	Fitting of the Pareto distribution by means of maximum likelihood	86
7.1	Omori-Utsu law parameters for Zakynthos aftershock sequence, as result from the Matlab module Basic Statistical Seismology.	90
7.2	The dependence of the p value and the other two parameters on the magnitude of completeness (M_c). All aftershocks were used from 25 th of October, 2018 till the 31 st of May of 2019. N is the number of aftershock for each M_c	92
7.3	The evolution of Omori-Utsu parameters using a time window of 20 days for the aftershock sequence with M_c equal to $2.5 M_L$. The step that is used is 20 days, from the day after the main shock 25 th of October until the 31 st of May, 2019. . .	95
7.4	Comparison of the Omori-Utsu law parameters of Zakynthos with two Ionian islands. The aftershock sequence lasts for 20 days in each case. The N in the table refers to the cumulative number of earthquakes. The data used for Zakynthos was calculated while for Kefalonia and Lefkada it was retrieved from paper [11].	97
9.1	Fitting of the Gamma distribution by means of maximum likelihood	106
9.2	Fitting of the Pareto distribution by means of maximum likelihood	107
9.3	Fitting of the Exponential distribution by means of maximum likelihood	108
9.4	Fitting of the Lognormal distribution by maximum likelihood	109
9.5	Fitting of the Weibull distribution by means of maximum likelihood estimation.	110
9.6	Parameters of the Gamma distribution obtained by means of maximum likelihood estimation.	111
9.7	Fitting of the Exponential distribution by means of maximum likelihood	112
9.8	Parameters of the Lognormal distribution estimated by means of maximum likelihood.	113

TECHNICAL UNIVERSITY OF CRETE

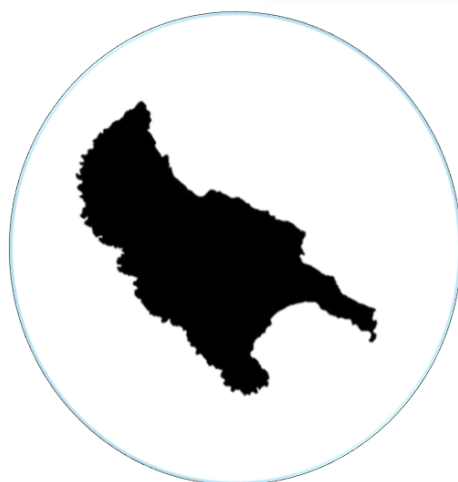
Abstract

Faculty Name
School of Mineral Resources Engineering

M.Sci

Thesis Title

by Michaela-Natalia VASILEIADI



Σχήμα 1: Το νησί της Ζακύνθου.

Εκτεταμένη Περίληψη

Για περισσότερο από έναν αιώνα οι στατιστικές ιδιότητες της γένεσης τόσο των προσεισμών όσο και των μετασεισμών έχουν γίνει αντικείμενο μελέτης απο πολλούς επιστήμονες σε σχέση με τις πολύπλοκες διαδικασίες γένεσης των σεισμών. Πολλά στοχαστικά μοντέλα, εμπειρικές σχέσεις και νόμοι έχουν προταθεί ώστε να εξηγηθεί και να αναπαρασταθεί τουλάχιστον ένα μέρος από τα παρατηρούμενα χαρακτηριστικά που εκφράζουν κάθε σεισμική ακολουθία. Για παράδειγμα, κάποιες ανωμαλίες στο ρυθμό της σεισμικότητας, με τη χρήση στατιστικών μοντέλων, μπορούν να θεωρηθούν πρόδρομα φαινόμενα ισχυρών σεισμών. Εκτός όμως από την πρόγνωση των σεισμών, η μελέτη των σεισμικών ακολουθιών αποτελεί ένα πολύ χρήσιμο εργαλείο στην προσπάθεια διερεύνησης των σεισμοτεκτονικών ιδιοτήτων του φλοιού της Γης, στην αποκάλυψη της σεισμογένεσης, της γεωμετρίας καθώς και της κινηματικής των ρηγμάτων.

Αντικείμενο της παρούσας διπλωματικής εργασίας είναι η στατιστική μελέτη των σεισμικών γεγονότων πριν τον κύριο σεισμό της Ζακύνθου ($6.6 M_L$) που έλαβε χώρα στις 25 Οκτωβρίου του 2018 καθώς και της μετασεισμικής ακολουθίας που προκλήθηκε από αυτόν.

Για την ανάλυση χρησιμοποιήθηκαν δεδομένα από τον κατάλογο σεισμών του Γεωδυναμικού Ινστιτούτου του Εθνικού Αστεροσκοπείου Αθηνών (NOA). Τα δεδομένα αυτά αναφέρονται στη χρονική περίοδο από 1 Ιουνίου του 2016 έως και 31 Μαΐου του 2019 και περιλαμβάνουν τις συντεταγμένες των σεισμών, το μέγεθος τους, το βάθος καθώς και την ακριβή ημερομηνία και ώρα καταγραφής. Αφορούν μία περιοχή μελέτης στην ευρύτερη τοποθεσία της Ζακύνθου, με συνολική έκταση περίπου 20.000 τετραγωνικά χιλιόμετρα. Η περιοχή μελέτης αποτελεί τμήμα του Ελληνικού τόξου και παρουσιάζει πολύ έντονη σεισμική δραστηριότητα. Τα δεδομένα χωρίστηκαν σε δύο φάσεις. Η πρώτη αφορά τους σεισμούς πριν από την περίοδο του ισχυρού σεισμού ($6.6 M_L$) και αναφέρεται στην χρονική περίοδο από 1 Ιουνίου, 2016 έως και 25 Οκτωβρίου, 2018 με συνολική διάρκεια 2 χρόνων και 5 μήνες. Η δεύτερη φάση αφορά την μετασεισμική περίοδο, ως αποτέλεσμα του ισχυρού σεισμού ($6.6 M_L$) και αναφέρεται στη περίοδο από 25 Οκτωβρίου, 2018 έως και 31 Μαΐου, 2019 με συνολική διάρκεια 7 μηνών. Το σύνολο των δεδομένων που μελετήθηκαν για αυτή την περίοδο περιλαμβάνουν 11778 σεισμικά γεγονότα από τα οποία 2112 αναφέρονται στους σεισμούς πριν τον κύριο σεισμό και τα υπόλοιπα 9666 στους μετασεισμούς, συμπεριλαμβανομένου και του κύριου σεισμού. Όλα τα σεισμικά γεγονότα που χρησιμοποιήθηκαν αφορούν σεισμούς με μέγεθος μεγαλύτερο και ίσο του $1 M_L$ (τοπικού μεγέθους) και αναφέρονται σε επιφανειακούς σεισμούς με ρηχό βάθος έως και 40 χιλιόμετρα.

Στην αρχή της εργασίας γίνεται μία εκτενής ανάλυση των στατιστικών εργαλείων και μεθόδων που χρησιμοποιούνται στη επιστήμη της σεισμολογίας καθώς και του θεωρητικού υποβάθρου που αφορά τα χαρακτηριστικά των σεισμών. Αναλύονται εκτενώς οι διαφορετικές κλίμακες που χρησιμοποιούνται για τη μέτρηση των σεισμών καθώς και οι εμπειρικές σχέσεις που έχουν προταθεί από

ξένους αλλά και Έλληνες επιστήμονες. Επιπρόσθετα γίνεται μία περιγραφή των βασικών νόμων αλλά και σχέσεων της σεισμολογίας καθώς και η εφαρμογή τους στην παρούσα διπλωματική.

Αφού αναλυθεί επαρκώς το στατιστικό, το σεισμικό αλλά και το θεωρητικό υπόβαθρο, ακολουθεί το τέταρτο Κεφάλαιο που ασχολείται με τη στατιστική ανάλυση των διαφόρων κλιμάκων μέτρησης του μεγέθους των σεισμών. Οι περισσότερες κλίμακες, βασίζονται σε κύματα που καλύπτουν μόνο ένα μέρος του φάσματος, τα μεγέθη των κλιμάκων αυτών αποτελούν μέτρα της ενέργειας που ακτινοβολείται στα αντίστοιχα παράθυρα συχνοτήτων και όχι της ολικής ενέργειας του σεισμού. Για αυτό τον λόγο έχει δημιουργηθεί μια κλίμακα μεγέθους η οποία δε βασίζεται σε κύματα περιορισμένου φάσματος συχνοτήτων, αλλά στο συνολικό φάσμα. Αυτή η κλίμακα ονομάζεται κλίμακα μεγέθους σεισμικής ροπής, M_w . Στην παρούσα εργασία δημιουργήθηκε μία εμπειρική εξίσωση η οποία περιγράφει τη σχέση μεταξύ του τοπικού μεγέθους (αρχικά δεδομένα) και του μεγέθους της σεισμικής ροπής. Για να δημιουργηθεί αυτή η σχέση χρησιμοποιήθηκε μια ευρύτερη χρονική περίοδος δεδομένων (2009-2019) διότι το M_w είναι περίπλοκο να καταγραφεί και να υπολογιστεί συνεπώς οι κατάλογοι σεισμών περιέχουν πολύ λίγες (ανεπαρκείς) καταγραφές αυτού του μεγέθους. Διατηρώντας την ίδια ακριβώς περιοχή μελέτης της Ζακύνθου και για μια πιο εκτεταμένη περίοδο 10 χρόνων μελετήθηκαν 55 σεισμικά γεγονότα. Η σχέση που δημιουργήθηκε από αυτά είναι αποτέλεσμα της ζυγισμένης ανάλυσης παλινδρόμησης και αφορά σεισμούς μεγέθους από $2.7 M_L$ έως και $6.6 M_L$. Αυτή η εμπειρική σχέση που κατασκευάσαμε εφαρμόστηκε στα αρχικά δεδομένα (2016-2019) της ανάλυσης μας για να εκφράσουμε τα σεισμικά γεγονότα σε μέγεθος σεισμικής ροπής (M_w). Ακολούθως για την οπτικοποίηση των αποτελεσμάτων, κατασκευάστηκαν σε R περιβάλλον προγραμματισμού τα γραφήματα (1) του μεγέθους σεισμικής ροπής ως προς τον χρόνο και (2) της αθροιστικής κατανομής της σεισμικής ροπής ως προς τον χρόνο.

Στη συνέχεια της ανάλυσης μας μελετήθηκε στο Κεφάλαιο πέντε η συχνότητα εμφάνισης σεισμών σε σχέση με το μέγεθος τους. Για τη μελέτη αυτή χρησιμοποιήθηκε ο νόμος του Gutenberg - Richter, ο οποίος αναφέρει ότι ο αριθμός των σεισμών είναι γραμμική συνάρτηση του μεγέθους των σεισμών. Μέσα από αυτή τη σχέση προσδιορίζεται η μεταβλητή b ή b -value η οποία είναι πολύ σημαντική και συνήθως σε κανονικές συνθήκες βρίσκεται κοντά στο 1. Η σημασία της οφείλεται στο γεγονός ότι μπορεί να περιγράψει τον βαθμό της ομοιογένειας των υλικών και την κατάσταση των τάσεων που επικρατούν στην εστιακή περιοχή [69]. Για την εφαρμογή όμως του νόμου αυτού είναι προαπαιτούμενη η γνώση του μεγέθους πληρότητας, M_c , που ορίζεται ως το ελάχιστο μέγεθος στο οποίο το 100% των σεισμών έχει καταγραφεί από ένα δίκτυο σεισμολογικών σταθμών. Η σωστή εκτίμηση του μεγέθους αυτού είναι κρίσιμη, καθώς μια μεγαλύτερη τιμή από την κανονική οδηγεί σε υποδειγματοληψία των δεδομένων, απορρίπτοντας χρήσιμα δεδομένα, ενώ μια χαμηλότερη τιμή οδηγεί σε λανθασμένο προσδιορισμό των σεισμικών παραμέτρων από τη χρήση ατελών δεδομένων. Για την εκτίμηση του μεγέθους αυτού, δοκιμάστηκαν 3 διαφορετικές μέθοδοι με τη χρήση ενός εργαλείου στο προγραμματιστικό περιβάλλον της Μάτλαμπ [74]. Η πρώτη μέθοδος

είναι η μέθοδος του συνολικού εύρους μεγεθών (EMR), η οποία κατασκευάζει ένα μοντέλο το οποίο περιγράφει όλο το εύρος των δεδομένων χρησιμοποιώντας την εξίσωση G-R και την αθροιστική κανονική κατανομή. Η δεύτερη είναι η μέθοδος μέγιστης καμπυλότητας (MAXC) η οποία βρίσκει το σημείο εκείνο όπου η μή αθροιστική κατανομή εμφανίζει τη μεγαλύτερη καμπύλη. Η τρίτη είναι η δοκιμή καλής προσαρμογής (GFF) όπου με αυτή τη μέθοδο υπολογίζεται η τιμή της απόλυτης διαφοράς του αριθμού του σεισμού μεταξύ πραγματικών και συνθετικών κατανομών. Αφού προσδιοριστούν τα καταλληλότερα μεγέθη πληρότητας για τους σεισμούς πριν τον κύριο σεισμό και για τους μετασεισμούς ($2.0 M_w$ και $2.5 M_w$) υπολογίζεται η παράμετρος b . Στην πρώτη περίπτωση υπολογίζεται συμπεριλαμβανομένου του κύριου σεισμού και στη δεύτερη περίπτωση υπολογίζεται η παράμετρος b χωρίς τον κύριο σεισμό. Στη συνέχεια μελετάται η εξάρτηση της παραμέτρου b από το μέγεθος M_c και στις δύο περιπτώσεις (πριν και μετά τον κύριο σεισμό). Ακολούθως εξετάζεται η εξέλιξη της τιμής της παραμέτρου b ως προς τον χρόνο μόνο για τους σεισμούς πριν τον κύριο σεισμό, χωρίζοντας τα σεισμικά γεγονότα ανα 200. Τέλος για την γραφική απεικόνιση των αποτελεσμάτων χρησιμοποιήθηκε ένας κώδικας στη Ματλαμπ κατασκευασμένο από τον κ.Χριστόπουλο [27].

Το έκτο κεφάλαιο αφορά τη στατιστική ανάλυση των χρόνων αναμονής μεταξύ διαδοχικών σεισμών. Στην ανάλυση αυτή, εφαρμόστηκαν 5 διαφορετικές κατανομές (Weibull, Gamma, Pareto, Exponential, Lognormal) στα δεδομένα των σεισμών πριν από τον κύριο σεισμό και των μετασεισμών, με στόχο την διερεύνηση της καλύτερης προσαρμογής τους. Οι χρόνοι αναμονής μεταξύ διαδοχικών σεισμών υπολογίστηκαν στο προγραμματιστικό περιβάλλον της R, αφαιρώντας τον χρόνο του προηγούμενου σεισμού από τον επόμενο. Οι χρόνοι αυτοί περιλαμβάνουν τα σεισμικά δεδομένα που ικανοποιούν το μέγεθος πληρότητας, το οποίο έχει βρεθεί $2.0 M_w$ για τους σεισμούς πριν από τον κύριο, με αριθμό 1262 και $2.5 M_w$ για τους μετασεισμούς, με αριθμό μετασεισμών 4692. Χρησιμοποιώντας αυτούς τους χρόνους (σε μονάδα μέτρησης λεπτών) κατασκευάστηκε ένα ιστόγραμμα για τους σεισμούς πριν από τον κύριο και ένα για τους μετασεισμούς. Στη συνέχεια αυτοί οι χρόνοι αναμονής υπολογίστηκαν σε ώρες και κατασκευάστηκαν 4 βασικά γραφήματα (ιστόγραμμα χρόνων, q-q γράφημα, διάγραμμα συνάρτησης κανονικής κατανομής και p-p γράφημα). Για την σύγκριση και την επιλογή του καταλληλότερου μοντέλου επιλέχθηκαν τα κριτήρια πληροφοριών Akaike (AIC) και τα πληροφοριακά κριτήρια καταλληλότητας Bayesian (BIC). Η μικρότερη τιμή που δίνουν και τα δύο κριτήρια AIC και BIC είναι η τιμή που αντιστοιχεί στην πιο κατάλληλη κατανομή.

Τέλος, στο έβδομο κεφάλαιο αναλύθηκε η συχνότητα της μετασεισμικής ακολουθίας της Ζακύνθου. Ειδικότερα εφαρμόστηκε ο Νόμος του Omori-Utsu και προσδιορίστηκαν οι παράμετροι του νόμου. Για τη μετασεισμική ακολουθία χρησιμοποιήθηκαν όλοι οι σεισμοί από τις 25 Οκτωβρίου, 2018 έως τις 31 Μαΐου, 2019 με μέγεθος μεγαλύτερο από το μέγεθος πληρότητας, το οποίο έχει υπολογιστεί παραπάνω. Αφαιρώντας λοιπόν όλους τους μετασεισμούς με μέγεθος μικρότερο του $2.5 M_w$, μένουν 4692 σεισμικά γεγονότα πάνω στα οποία εφαρμόζεται

το μοντέλο του Omori-Utsu για 220 μέρες. Το συγκεκριμένο μοντέλο εφαρμόστηκε πολύ καλά στα δεδομένα, δίνοντας τις εξής παραμέτρους: $p = 1.57$, $k = 30531.70$, $c = 35.79$. Στη συνέχεια μελετήθηκε η εξάρτηση των παραμέτρων αυτών (1) από το μέγεθος πληρότητας και (2) από τον χρόνο. Ως προς την εξάρτηση από το μέγεθος πληρότητας βρέθηκε ότι η τιμή του p επηρεάζεται καθώς με την αύξηση του M_c συνήθως μειώνεται. Ως προς την εξάρτηση από τον χρόνο, υπολογίστηκαν κάθε φορά διαφορετικοί παράμετροι του νόμου Omori-Utsu και χρησιμοποιώντας ένα παράθυρο 20 ημερών. Επιπλέον, συγκρίθηκαν τα αποτελέσματα των παραμέτρων της Ζακύνθου (1) με τα αποτελέσματα των παραμέτρων της μετασεισμικής ακολουθίας του σεισμού στην περιοχή Hokkaida-Nansei-Oki στη Ιαπωνία και (2) με τα αποτελέσματα των παραμέτρων των σεισμικών ακολουθιών της Κεφαλονιάς και της Λευκάδας. Οι τρεις αυτές συγκρίσεις έγιναν διότι (1) ο σεισμός της περιοχής Hokkaida-Nansei-Oki, Ιαπωνία είχε παρόμοια χρονική διάρκεια μετασεισμικής δραστηριότητας (262 μέρες) και περιλάμβανε παρόμοιο αριθμό μετασεισμών, ενώ (2) η Κεφαλονιά και η Λευκάδα (δύο νησιά στο Ιόνιο) βρίσκονται πάνω από το Ελληνικό Τόξο, όπως και η Ζάκυνθος, συνεπώς εμφανίζουν παρόμοια σεισμοτεκτονικά χαρακτηριστικά και οι μετασεισμικές τους ακολουθίες είχαν προκληθεί από σεισμούς με παρόμοιο μέγεθος $6.1 M_L$ και $6.5 M_L$, ακολούθως.

Τα πιο σημαντικά συμπεράσματα που προκύπτουν από την ανάλυση είναι τα ακόλουθα :

Η εξίσωση που δημιουργήθηκε χρησιμοποιώντας τη μέθοδο της ζυγισμένης ανάλυσης παλινδρόμησης για να περιγραφεί η σχέση μεταξύ του τοπικού μεγέθους με το μέγεθος σεισμικής ροπής, μπορεί να υποεκτιμά (υπό περιπτώσεις) τα αποτελέσματα σε σχέση με τις εμπειρικές σχέσεις Ξένων αλλά και Ελλήνων σεισμολόγων. Παρόλα αυτά, η σχέση αυτή εκφράζει μία αρκετά εστιασμένη περιοχή, γύρω από τη Ζάκυνθο και περιγράφει με τον καλύτερο τρόπο τα δεδομένα αυτά από το 2009-2019. Είναι σημαντικό να αναφερθεί ότι τα δεδομένα αυτά μπορεί να διέπονται από τυχαία αλλά και συστηματικά σφάλματα, τα οποία εισάγονται στα δεδομένα κατά την διαδικασία καταγραφής και επεξεργασίας τους. Τα τυχαία σφάλματα προκύπτουν από τον ανθρώπινο παράγοντα που υπεισέρχεται στην παρατήρηση των χρόνων άφιξης των κυμάτων και σε πιθανές προσωρινές βλάβες του σεισμολογικού δικτύου ή και στην αντικατάσταση των παλαιών οργάνων με νέα σεισμόμετρα. Τα συστηματικά σφάλματα σχετίζονται με τις αβεβαιότητες του μοντέλου που χρησιμοποιείται για τον υπολογισμό των χρόνων διαδρομής καθώς και σε αλλαγές του τρόπου υπολογισμού των μεγεθών (χρήση διαφορετικών εμπειρικών σχέσεων) στο πέρασμα του χρόνου (διάρκεια μελέτης 10 χρόνων). Επίσης πολλά σφάλματα μπορεί να δημιουργηθούν από το φαινόμενο του κορεσμού του τοπικού μεγέθους. Αυτό σημαίνει ότι για μεγάλους σεισμούς το τοπικό μέγεθος υποεκτιμά το πραγματικό μέγεθος του σεισμού. Τα μήκη κύματος των κυμάτων αυτών είναι μικρά σε σχέση με τις διαστάσεις των ρηγμάτων με αποτέλεσμα να μην επηρεάζεται το πλάτους τους από την αύξηση των διαστάσεων του ρήγματος.

Όσον αφορά την εκτίμηση του M_c και την εφαρμογή του νόμου G-R για τον

υπολογισμό της παραμέτρου b-value. Οι τρεις διαφορετικές μέθοδοι που χρησιμοποιήθηκαν μας δίνουν πολύ κοντινά αποτελέσματα για τους σεισμούς πριν τον κύριο σεισμό με μέση τιμή $M_c = 2.1 \pm 0.1 M_w$ και για τη μετασεισμική ακολουθία $M_c = 2.5 \pm 0.1 M_w$. Απο την ανάλυση της σχέσης του M_c με το b-value παρατηρήθηκε ότι υπάρχει μία εξάρτηση και ότι με την αύξηση του M_c αυξάνεται και η τιμή του b-value. Και στις δύο περιπτώσεις, πριν και μετά τον κύριο σεισμό το b-value βρέθηκε κοντά στο 1 με b-value = 1.18 πριν το σεισμό και b-value = 1.00 για μετά. Οι τιμές αυτές είναι κοντά στο 1 το οποίο σημαίνει ότι η περιοχή μελέτη μας έχει το αναμενόμενο σεισμικό υπόβαθρο. Παρόλαυτα θα περιμέναμε οι τιμές του b-value πριν το σεισμό να είναι μικρότερες και μετά τον σεισμό μεγαλύτερες σύμφωνα με τη βιβλιογραφία. Το αντίστροφο αυτό φαινόμενο μπορεί να εξηγηθεί με την πιθανή ύπαρξη σημοσεισμικής δραστηριότητας. Συγκεκριμένα παρατηρήθηκε ότι πριν τον Μάρτιο του 2017 εμφανίζεται μία έντονη αύξηση της τιμής του b-value με μέγιστη τιμή κοντά στο 1.52, φαινόμενο που υποδηλώνει την πιθανή ύπαρξη σημοσεισμών [5]. Επιπλέον, πολλοί σεισμολόγοι υποστηρίζουν ότι πριν απο ένα μεγάλο σεισμό υπάρχει μία μικρή πτώση στην τιμή του b-value. Αυτό το φαινόμενο παρατηρήθηκε στο γράφημα 5.2 όπου τα σεισμικά γεγονότα πριν τον κύριο σεισμό χωρίστηκαν σε 10 ομάδες με 200 σεισμικά γεγονότα το καθένα. Συγκεκριμένα απο τον Δεκέμβριο, 2017 μέχρι και τον Μαΐο, 2018 παρατηρήθηκε μία πτώση της τιμής του b-value, η οποία θα μπορούσε να θεωρηθεί προάγγελος του κυρίου σεισμού.

Η στατιστική ανάλυση των χρόνων αναμονής μεταξύ διαδοχικών σεισμών έδωσε τα ακόλουθα αποτελεσματα. Η κατανομή η οποία περιγράφει καλύτερα τους χρόνους αναμονής των σεισμών πριν τον κύριο σεισμό είναι η κατανομή Weibull. Ενώ κατανομή που εφαρμόζει καλύτερα στους χρόνους αναμονής των μετασεισμών είναι η Pareto. Οι κατανομές αυτές θα μπορούσαν να προβλέψουν τη συμπεριφορά της μετασεισμικής ακολουθίας.

Τέλος, στην ανάλυση της μετασεισμικής ακολουθίας με την εφαρμογή του νόμου Omori-Utsu (O-U), παρατηρήθηκε πολύ καλή εφαρμογή των αρχικών δεδομένων της Ζακύνθου με τα δεδομένα πρόβλεψης του νόμου. Οι παράμετροι εκτιμήθηκαν ως $p = 1.57$, $k = 30531.70$ και $c = 35.79$, τιμές ανάμενόμενες σύμφωνα με τη βιβλιογραφία. Απο τη ανάλυση της εξάρτησης των παραμέτρων και συγκεκριμένα της παραμέτρου p καταλήξαμε στα εξής συμπεράσματα : (1) Υπάρχει εμφανής εξάρτηση του μεγέθους πληρότητας με τη παράμετρο p και συγκεκριμένα στην παρούσα μελέτη είναι αντιστρόφος ανάλογα. (2) Ως προς την εξάρτηση απο τον χρόνο, παρατηρήθηκε ότι τις πρώτες 20 με 40 ημέρες της μετασεισμικής ακολουθίας η τιμή p εκτιμάται αρκετά χαμηλή (0.38 και 0.40) ενώ μετά το πέρας των 3 μηνών εμφανίζει τιμές κοντά και μεγαλύτερες από το 1. Αυτό μπορεί να συμβαίνει είτε διότι η μετασεισμική ακολουθία δεν ενεργοποιήθηκε αμέσως είτε γιατί μετά απο 3 μήνες έχει επανέλθει η κανονική σεισμικότητα της περιοχής και έχει δημιουργηθεί μία αλληλοκάλυψη της μετασεισμικής ακολουθίας με το κανονικό σεισμικό υπόβαθρο. Στη συνέχεια, από τη σύγκριση των αποτελεσμάτων μας με την Ιαπωνία καταλήξαμε στο ότι στα αποτελέσματα της Ζακύνθου η παράμετρος p εμφανίζει αρκετά μεγαλύτερες διακυμάνσεις ως προς το μέγεθος πληρότητας σε σχέση με τις διακυμάνσεις της παραμέτρου p ως προς M_c

που έχουν υπολογιστεί από τον Utsu για την σεισμική ακολουθία της περιοχής Hokkaida-Nansei-Okii. Από τη σύγκριση των αποτελεσμάτων των δύο Νησιών του Ιονίου με τη Ζάκυνθο καταλήγουμε στα εξής: (1) Θεωρώντας μετασεισμική ακολουθία με διάρκεια 20 ημερών η Ζάκυνθος και η Κεφαλονία εμφανίζουν και οι δύο αρκετά χαμηλές τιμές p (0.38, 0.46) και παρόμοια μικρή τιμή παραγωγικότητας k , 172.35 και 229.1, αντίστοιχα. Ενώ η Λευκάδα εμφανίζει τιμή της παραμέτρου $p = 1.08$ μία τιμή κοντά στο 1 και μεγαλύτερη από της προαναφερόμενες. Οι παράμετροι του νόμου Omori-Utsu δεν είναι ακόμη ξεκάθαρο από πού προέρχονται και από τι εξαρτώνται, συνεπώς χρειάζεται παραπάνω διερεύνηση των παραμέτρων αυτών.

Abstract

Earthquakes are one of the most dangerous natural disasters that can cause widespread damage and loss of human life. For more than a century the complex generating mechanisms and the statistical properties of both foreshock and aftershock sequences have been studied by many scientists. Stochastic models, empirical relations, and seismological laws have been proposed to explain and represent at least some of the observed characteristics of seismic sequences.

The aim of this dissertation is the statistical analysis of the seismic sequence before the main earthquake ($6.6 M_L$) of Zakynthos, Greece that took place on October 25, 2018 and the aftershock sequence that resulted from it. The data used in this analysis were obtained from the earthquake catalog of the Institute of Geodynamics of the National Observatory of Athens (NOA). They refer to the period from 1/06/2016 to 31/05/2019 and extend over an area which is part of the Hellenic Trench and has intense seismic activity.

The relation between earthquake magnitude scales was studied, and an empirical relation between local magnitude (M_L) and moment magnitude (Mw) was established using weighted linear regression analysis. In order to establish this relation and due to insufficient data in the seismic catalogs with recordings on the moment magnitude scale, it was necessary to study a data set covering a more extended period (2009-2019). The empirical relation was used to express earthquake magnitudes in the moment magnitude (Mw) scale, and the plots of moment magnitude and cumulative seismic moment evolution over time were created in the R programming environment.

Then, the frequency of earthquakes in relation to their magnitude was studied (Gutenberg-Richter law), and the b-value parameter was estimated. A prerequisite for the Gutenberg-Richter analysis is the determination of the magnitude of completeness (M_c), which was estimated with three different methods: (1) by the method of entire magnitude range (EMR), (2) by the method of maximum curvature (MAXC) and (3) with the Goodness of fit (GFF). Furthermore, the dependence of the b-value parameter on the magnitude of completeness (M_c) and the variation of this parameter over time before the main earthquake were examined. The interevent times distribution between successive earthquakes was subsequently studied, for both prior and after the main event, by applying 5 different probability distributions (Weibull, Gamma, Pareto, Exponential and Lognormal). The Akaike information criterion (AIC) and the Bayesian information criterion (BIC) were used to compare the distribution models and to select the optimal model. The distribution that provides the best fit for the interevent times before the main event is the Weibull distribution, while the one that gives the best fit for the aftershock sequence is the Pareto distribution.

Finally, the frequency of seismic events in the Zakynthos aftershock sequence was investigated by applying Omori-Utsu's (O-U) law; the parameters of this law were estimated as $p = 1.57$, $k = 30531.70$ and $c = 35.79$. In addition, the dependence of the O-U parameters (1) on the magnitude of completeness and (2) on time was studied. The results of the parameters

of Zakynthos were compared (1) with the results of the parameters of the aftershock sequence in Hokkaido-Nansei-Oki, Japan (1993), and (2) with the results of the parameters of the aftershock sequences of the Kefalonia (26/1/2014) and Lefkada (17/11/2015) main events.

The most important conclusions derived in this thesis are summarized below:

1. The empirical equation of M_w with M_L is in good agreement with the empirical relations proposed by seismologists, but in some cases it may underestimate the moment magnitude.

2. The implementation of the Gutenberg-Richter law and the estimation of the b-value parameter give expected values close to 1 for the earthquakes before the main event but also for the aftershock sequence. Analyzing the b-value parameter over time, we observed an increase in its value from September 2016 until April 2017. This observation indicates the existence of swarm activity. On the other hand, from May 2018 until shortly before the main earthquake, there was a drop in b-value which could be viewed as a precursor to the main earthquake.

3. The aftershock sequence is in good agreement with Omori-Utsu's law, and the O-U parameters are close to literature results.

4. The O-U exponent p was found to depend on time (proportionally) and on the magnitude of completeness (inversely proportionally).

5. The O-U exponent p estimated for the Japan earthquake shows small dependence on the magnitude of completeness in contrast with the Zakynthos p parameter which depends on M_c .

6. Assuming an aftershock sequence with duration of 20 days the values of the O-U exponent p for Zakynthos and Kefalonia are smaller than one (0.38 and 0.48 respectively), while the respective parameter for Lefkada $p = 1.08$ is close to one.

Chapter 1

Introduction

1.1 Motivation

During the 20th century, earthquakes, both directly and indirectly, have caused much suffering and damage to mankind. In Greece, more than 200 deaths have been recorded during that period, but more than 2000 people were injured [72]. Earthquakes have a direct social relevance because of their significant influence on human societies.

The genesis of earthquakes is an unsolved mystery in the earth sciences, due to the complexity of understanding, monitoring, and accurately predicting them. The underlying physical mechanisms are yet unknown. Unlike the weather, which can be predicted with some precision for a couple of days in advance, earthquake forecasting remains an elusive goal, because of the lack of direct observations and the fact that the governing equations are still unknown.

Additionally, earthquakes generally occur suddenly thus, they are considered the most feared natural hazards. Floods develop gradually, hurricanes can be tracked, a variety of precursory phenomena precedes volcanic eruptions, and measurable atmospheric conditions cause tornados. Earthquakes, however, occur without warning and often without precursory indicators.

This thesis is motivated by the fascinating unknown of this phenomenon, earthquake, and the innate need to apply geostatistical approaches to understand the triggering mechanism and tackle the problems it can bring. Preventing the disasters that society has to handle after every significant event, by predicting where and when an earthquake will struck, also motivates this thesis.

1.2 Data and Study Area

The study area is the island of Zakynthos (Greece), one of the Ionian Islands, located in the western part of Greece. Zakynthos is the third largest island of the Ionian Islands, has a population of 39.737, and covers an area of 405.55 km² [24].

On October 25, 2018 22:54 UTC, a significant earthquake of 6.6 M_L magnitude occurred in Zakynthos Island, which is located at a complex plate boundary region. It struck approximately 40 km to the NW of the Strofades island and 36 km to the SW of Zakynthos. According to the manual solution of National Observatory of Athens[53], it was a shallow crustal event with a focal depth at 10 km. EMSC determined the epicenter of the earthquake at 37.53°N 20.62 °E, south of Zakynthos island coast.

Limited structural damages were reported mainly on the dock of the Zakynthos harbour and at the Strofades monastery [36]. Tsunami alert messages, based on the earthquake parameters, were issued within ten minutes after the event by both the Italian and the Greek Tsunami Service Providers. The earthquake generated a small tsunami recorded by some tide gauges, including those located at Katakolo and Kyparissia in Greece, and Crotone and Le Castella in Italy.

The aftershock activity lasted for a long time, through which the permanent seismological networks of Greece recorded a lot of weak events. During the first ten (10) days, the seismicity was denser, while in this period the largest aftershocks took place. The 15 strongest events that followed the main event ranged between 4.4 M_L and 5.5 M_L magnitude, while the majority of those occurred in depth shallower than 13 km.

According to Sokos *et al.* [73] and Mouslopoulou *et al.* [49], the 2018 mainshock consisted of two fault segments: a low-dip thrust, and a dominant, moderate-dip, right-lateral strike slip, both in the crust. Slip vectors, oriented to Southwest, are consistent with plate motion. The sequence results from rupture of upper-plate faults shown in fig. 1.1 with varying strike and kinematics [49].

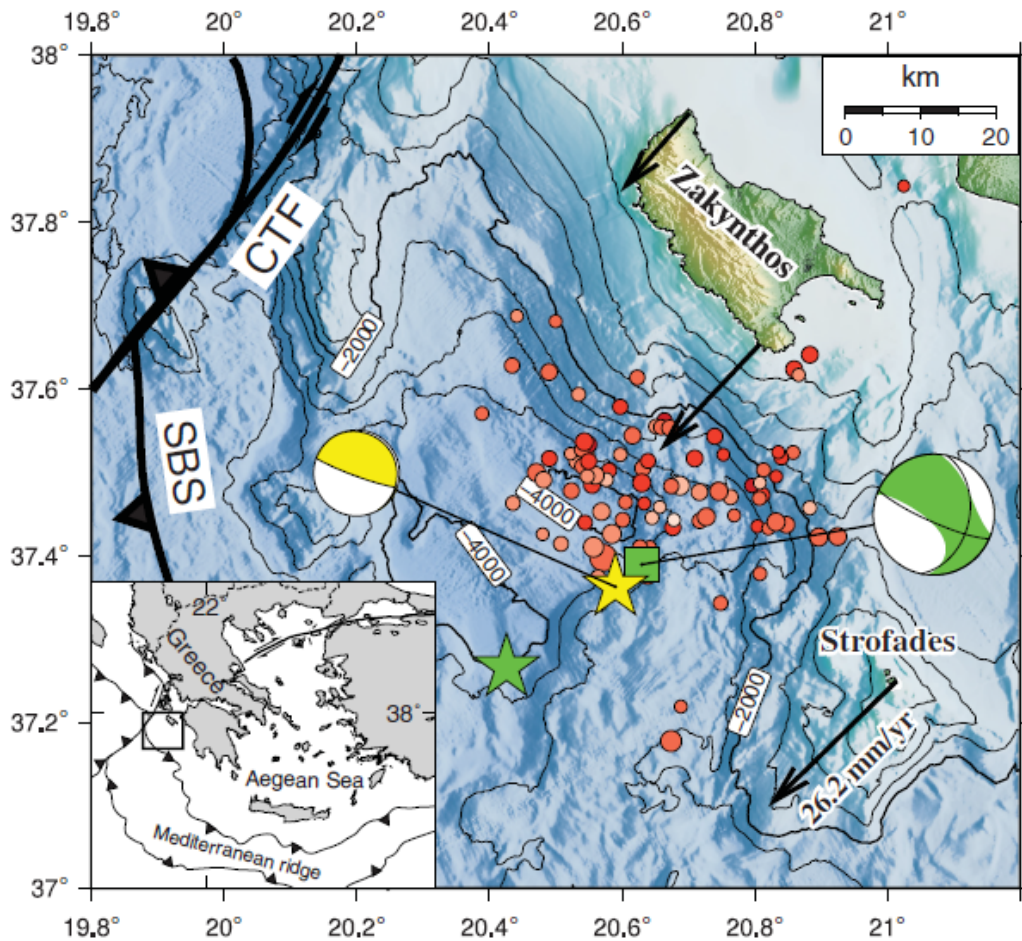


FIGURE 1.1: The 2018 Zakynthos earthquake sequence. Foreshock Mw 4.8 (yellow star and focal mechanism plot), mainshock epicenter (green star), centroid moment tensor (CMT; green square and focal mechanism plot), and activity in the first 24 hr, superimposed on bathymetry. The Cephalonia transform fault (CTF) and the subduction backstop (SBS) are shown. Three characteristic plate-velocity vectors are included. Retrieved from [73].

Seismicity of Zakynthos

Zakynthos Island is located within Greece in the Ionian Sea, at the western part of the Hellenic Trench. It is divided into the western part of Zakynthos, which lies in the Pre-Apulian Zone and the eastern part, which lies in the Ionian Zone, the most western zones of Greece. These two zones are divided by the Ionian thrust fault [35]. The Pre-Apulian zone consists of an eastward dipping succession of Upper Cretaceous to Miocene carbonates overlain by Pliocene-Quaternary alluvia.

Zakynthos is located very close to the convergent boundary between African and Eurasian plates, as shown in Fig. 1.2, and is undergoing very rapid and intense ground deformations (around 26 mm/yr) [64]. The island has a complex palaeogeographic history due to the westward migration of external Hellenides, which played the key role in the syn and post collisional phases.

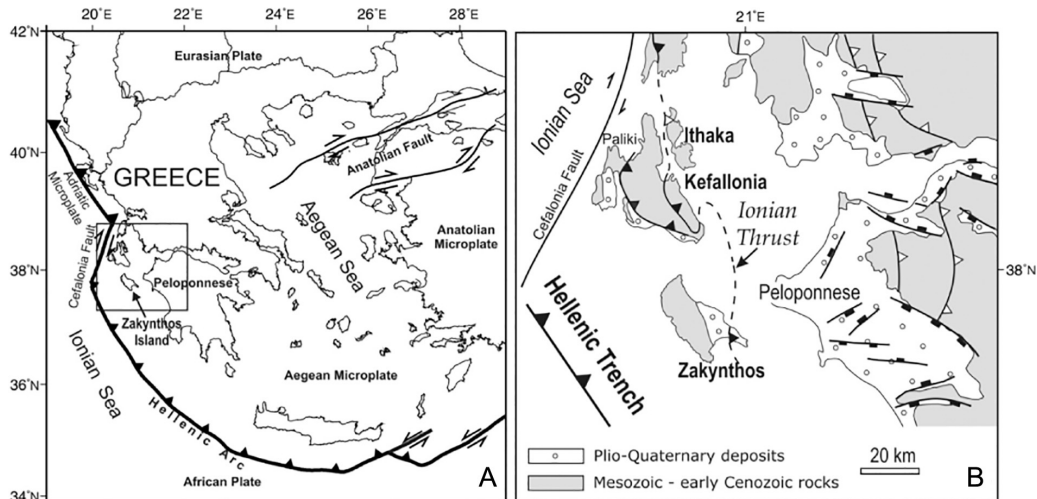


FIGURE 1.2: (A) Simplified map of Greece showing the Hellenic trench, the major fault systems and the study area Zakynthos Island and (B) map of western Greece with the main fault systems and the Ionian Island Zakynthos, Kefalonia and Lefkada. Retrieved from [4].

The specific tectonic characteristics of Zakynthos create an intense crustal deformation in the Central Ionian Sea, leading to earthquakes ranging between moderate and strong. All those attributes classify the Ionian Sea as a seismotectonically complex area of high seismicity.

The most destructive earthquake in Greece in the last century occurred there, in the area of the Ionian Islands on August 12, 1953, with a magnitude equal to 7.2 M_w , causing a total destruction of the town of Zakynthos, shown in figure 1.3. The third most destructive earthquake, which is studied in this thesis, occurred on October 25, 2018, 65 years after.



FIGURE 1.3: The results of the catastrophic earthquake in Zakynthos, 1953. Retrieved from [62]

The most significant events since the 20th century are listed in Fig. 1.4 and include those events on November 18, 1997 ($6.5 M_w$), SW of Zakynthos Island, December 2, 2002 ($5.5 M_w$), a sequence of earthquakes during October 2005 ($5.6 M_w$) and April 2006 (5.5 – $5.7 M_w$) south of Zakynthos, June 8, 2008 ($6.4 M_w$) at Andravida (Peloponnisos), January 26, 2014 ($6.1 M_w$) at Paliki (Cephalonia) and November 17, 2016 ($6.4 M_w$) in Lefkas. Clustering is noticeable in the figure. One cluster occurred in 2011 and 2015 at the place of the 2006 Zakynthos sequence, and one cluster was repeatedly activated three times (twice in 2016 and once in 2017) very near the 1997 and 2018 events. With the white star the epicenter of every major earthquake is presented in Fig.1.4.

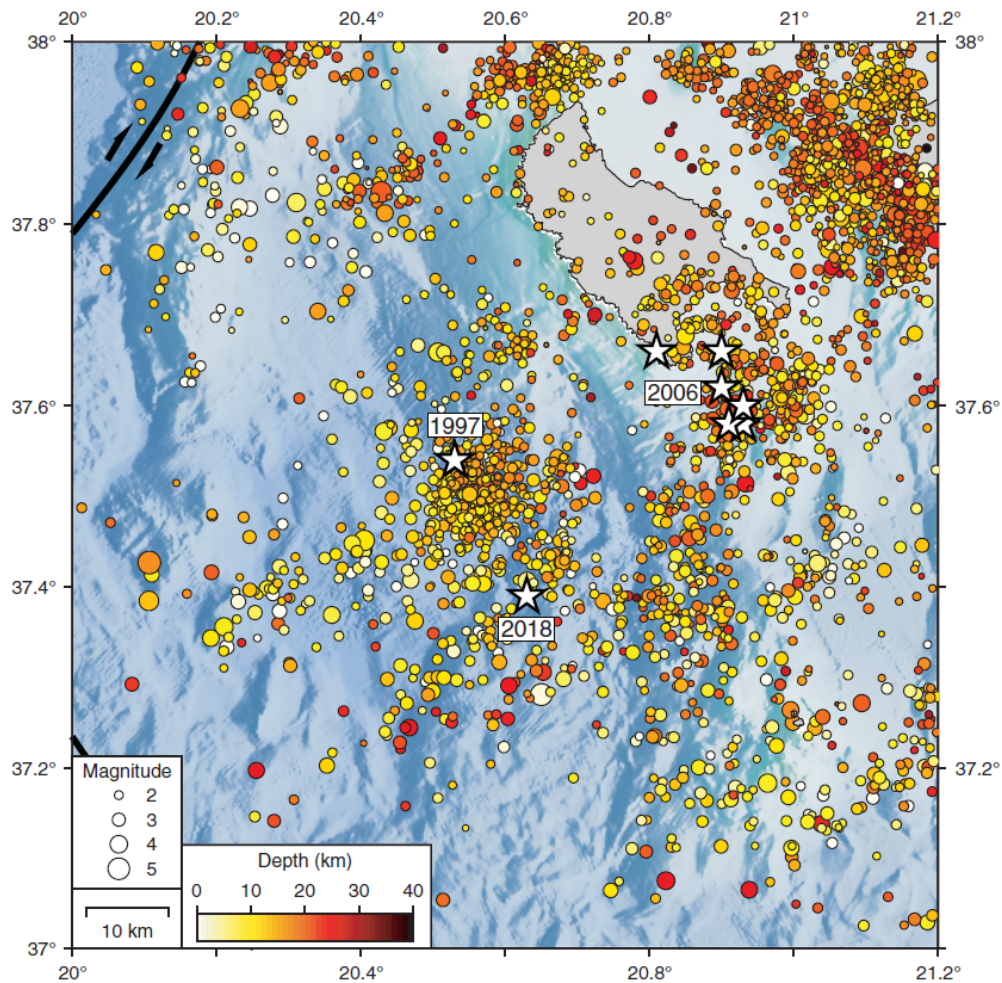


FIGURE 1.4: Space distribution of earthquakes 2011–2018 (until the 2018 mainshock). The centroids of significant earthquakes southwest of Zakynthos, in 1997 [40], 2006 [70], and 2018 [73], occurred near two localized clusters.

The complete and detailed knowledge of the historical earthquakes, the past earthquake environmental effects and the respective seismic intensities has become significant in recent years due to the fact that among others it serves as a valuable tool for revealing and highlighting sites of significant earthquake related hazards. The more we learn about a specific area's past seismicity, the more we understand and we can predict and prevent a priori large catastrophes.

Chapter 2

Statistical Methods in Seismology

From a statistical point of view, an earthquake catalog is the available data on earthquakes in a space-time window. Statistical analysis can then be used to find a suitable model for the underlying earthquake process. Such a model provides a theoretical description of the seismic activities in the study region and makes it possible to estimate the probabilities of future events. Therefore, fitting an appropriate statistical model to a given earthquake catalog is of great importance in the probabilistic assessment of seismic hazard. In this Chapter, a variety of statistical tools and methods are described, which were used to understand and model better the behaviour of an earthquake. In addition, the properties of an earthquake and how those are measured, are explained; as they appear prerequisite to the analysis. By applying and testing different statistical methods on the earthquake events, we extract crucial information that help us to understand, explain and even predict earthquakes.

2.1 Probability Distributions

An earthquake sequence can be modeled as a stochastic variable via statistical analysis. The first step that has to be carried out is the investigation of the best fitted distribution to the data of the sequence data. Tomohiro Hasumi *et al.* [76], shown that the time interval distribution for the earthquakes occurring on a single fault can be described by the Weibull distribution, and that the Weibull exponent increases with the increase of the magnitude threshold. In the following sections various probability distributions, including the Poisson, Normal, and Pareto and some others are presented.

2.1.1 Poisson-distribution

A Poisson distribution is a probability distribution that characterizes discrete events occurring independently of one another in time.

The distribution is popular for modeling the "number of times an event occurs in an interval of time or space".

A discrete random variable X is said to have a Poisson distribution with parameter $\lambda > 0$, if, for $k = 0, 1, 2, \dots$, the probability mass function of X is given by:

$$f(k; \lambda) = \Pr(X = k) = \frac{\lambda^k e^{-\lambda}}{k!}, \quad (2.1)$$

where e is Euler's number ($e = 2.71828\dots$) and $k! = 1 \times 2 \times 3 \dots k$ is the factorial of the integer number k .

The positive real number λ is equal to the expected value of X , as well as to its variance

$$\lambda = E(X) = \text{Var}(X).$$

The Poisson distribution can be applied to systems with a large number of possible events, each of which is rare. The number of such events that occur during a fixed time interval is, under the right circumstances, a random number with a Poisson distribution.

In earth science, we can use Poisson distribution to forecast earthquakes since big earthquakes are rare, assuming that earthquakes are independent and homogeneous events. However, many seismologist [86] state that almost no catalog fits the Poisson distribution exactly. For research purposes its role as a base-line model for 'standard seismicity' has been replaced by the ETAS model (see Section 3.2.3), which provides a much better approximation to the clustering properties of smaller earthquakes.

2.1.2 The Normal Distribution

The normal distribution, also known as the Gaussian distribution, is the most important distribution in statistics. It is often encountered in natural phenomena as a result of the Central Limit Theorem. The latter—loosely expressed—states that the normal distribution is an attractor for averages of identically distributed random variables so long as their probability distributions do not have heavy tails. Its crucial property is that any affine combination of independent normal random variables is in addition normal. An affine combination of vectors x_1, \dots, x_n is a vector $\sum_{i=1}^n a_i x_i = a_1 x_1 + a_2 x_2 + \dots + a_n x_n$, called a linear combination of x_1, \dots, x_n , in which the sum of the coefficients is equal to 1, thus, $\sum_{i=1}^n a_i = 1$. The probability density function (pdf) of a normal distribution [1] is given as follows:

$$f(x; \mu, \sigma^2) = \frac{1}{\sigma\sqrt{2\pi}} e^{-\frac{1}{2}\left(\frac{x-\mu}{\sigma}\right)^2}, \quad (2.2)$$

where μ is a location parameter, equal to the mean, and σ is the standard deviation. For $\mu = 0$ and $\sigma = 1$ we refer to this distribution as the standard normal distribution. In many connections it is sufficient to use this simpler form since μ and σ simply may be regarded as a shift and scale parameter, respectively. In Fig. 2.1 and Fig. 2.2 different types of the normal distribution are presented.

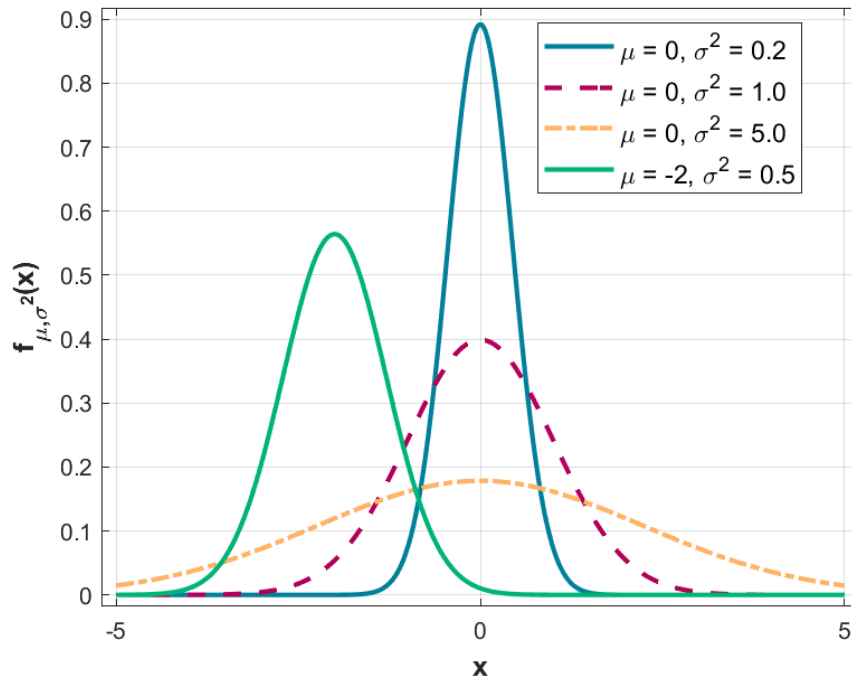


FIGURE 2.1: Plot of the probability density function for the Normal Distribution.

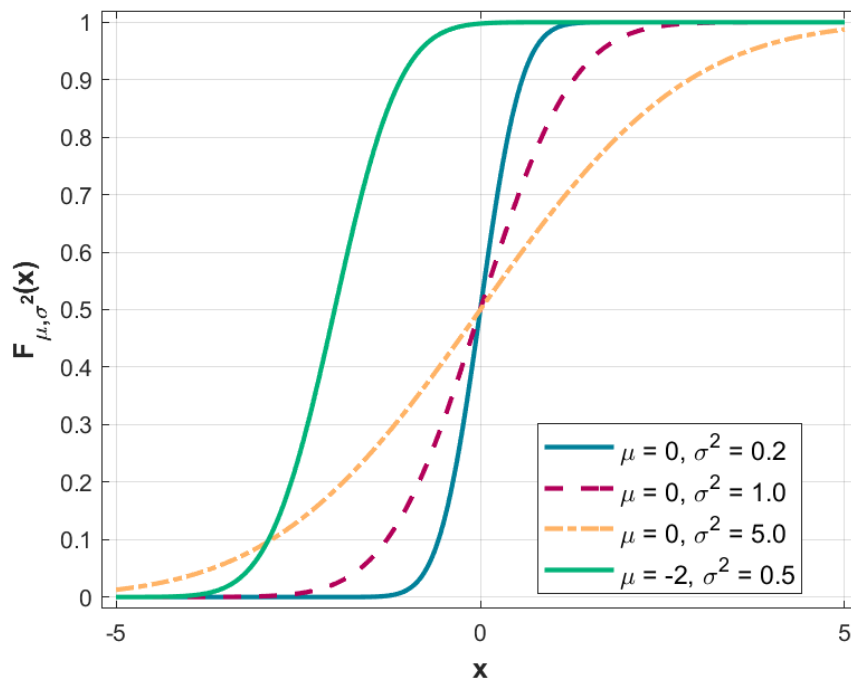


FIGURE 2.2: Plot of the cumulative distribution function for the Normal Distribution.

Skewness

Skewness is defined in terms of the centered third-order moment of the distribution, is a measure of the symmetry or asymmetry of the probability

density function. The skewness of the normal distribution and all other symmetric distributions is equal to zero[1]. Any data with a symmetric empirical distribution should also have a skewness near zero.

The skewness of a distribution is defined as

$$s = \frac{\mu_3^2}{\mu_2^3} = 0. \quad (2.3)$$

Kurtosis

Kurtosis is defined in terms of the centered fourth-order moment of the distribution, and is a measure of whether the data are more or less concentrated near the peak relative to a normal distribution. The kurtosis for the standard normal distribution is equal to three, calculated by

$$\text{kurtosis} = \frac{\mu_4}{\mu_2^2} = 3. \quad (2.4)$$

2.1.3 The Gamma Distribution

The Gamma distribution is a two parameter family of continuous probability distributions. It can be considered as the generalization of the exponential distribution.

A random variable X that is gamma-distributed with shape a and scale b is denoted as:

$$X \sim \Gamma(a, b) \equiv \text{Gamma}(a, b). \quad (2.5)$$

The corresponding probability density function in the shape-rate parametrization is

$$f(x; \alpha, \beta) = \frac{\beta^\alpha x^{\alpha-1} e^{-\beta x}}{\Gamma(\alpha)} \quad \text{for } x > 0 \quad \alpha, \beta > 0, \quad (2.6)$$

where $\Gamma(\alpha)$ is the gamma function.

Skewness

Skewness of the gamma distribution is equal to $2/\sqrt{a}$, and depends only on the shape parameter a . The gamma distribution approaches a normal distribution when a is large (approximately when $a > 10$).

Median

Unlike the mode and the mean which have readily calculable formulas based on the parameters of the gamma distribution, the median does not obey to a closed form equation. The median for this distribution is defined as the value ν such that

$$\frac{1}{\Gamma(a)b^a} \int_0^\nu x^{a-1} e^{-\frac{x}{b}} dx = \frac{1}{2}. \quad (2.7)$$

$$v \approx \mu \frac{3a - 0.8}{3a + 0.2}. \quad (2.8)$$

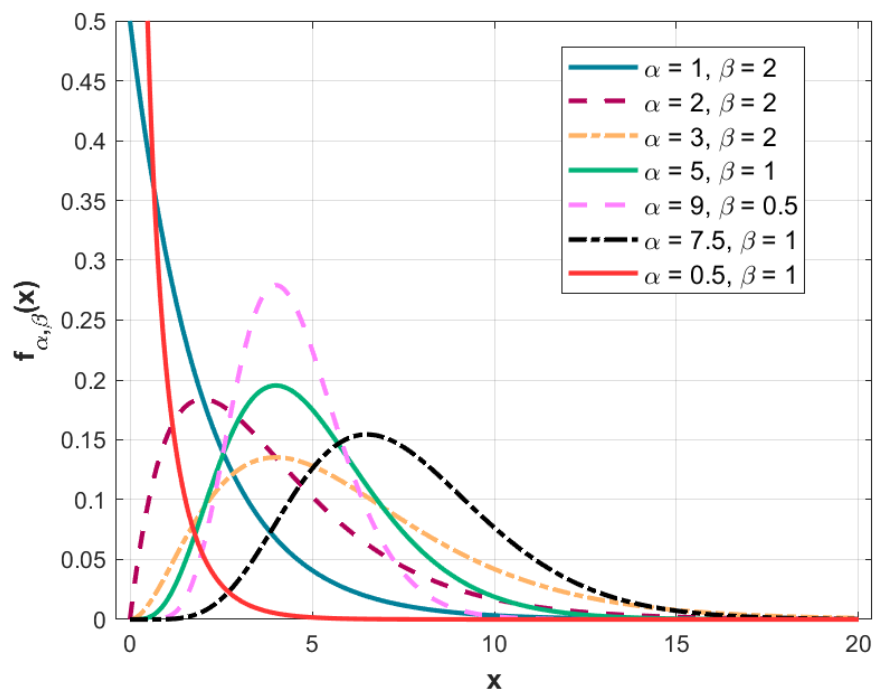


FIGURE 2.3: Plot of the probability density function for the Gamma Distribution.

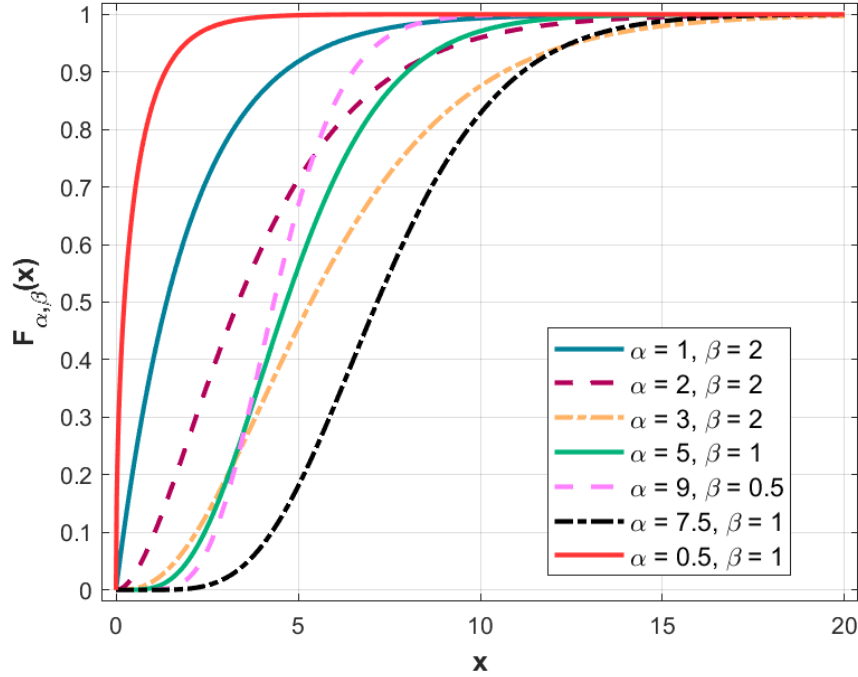


FIGURE 2.4: Plot of the cumulative distribution function for the Gamma Distribution.

If X_i follows a $\text{Gamma}(a_i, b)$ distribution for $i = 1, 2, \dots, N$ (i.e., all distributions have the same scale parameter b), then

$$\sum_{i=1}^N X_i \sim \text{Gamma} \left(\sum_{i=1}^N a_i, b \right), \quad (2.9)$$

where \sim denotes equality in distribution, provided all X_i are independent.

2.1.4 Weibull Distribution

The Weibull distribution is a continuous probability distribution and can be considered as the generalization of the exponential distribution. The probability density function of a Weibull random variable is:

$$f(x; \lambda, k) = \begin{cases} \frac{k}{\lambda} \left(\frac{x}{\lambda}\right)^{k-1} e^{-(x/\lambda)^k} & x \geq 0, \\ 0 & x < 0, \end{cases} \quad (2.10)$$

where $k > 0$ is called shape parameter and $\lambda > 0$ is called the scale parameter of the distribution. Weibull distributions with $k < 1$ have a decreasing failure rate, whereas Weibull distributions with $k > 1$ have an increasing failure rate. A value $k = 1$ indicates a constant failure rate over time [10].

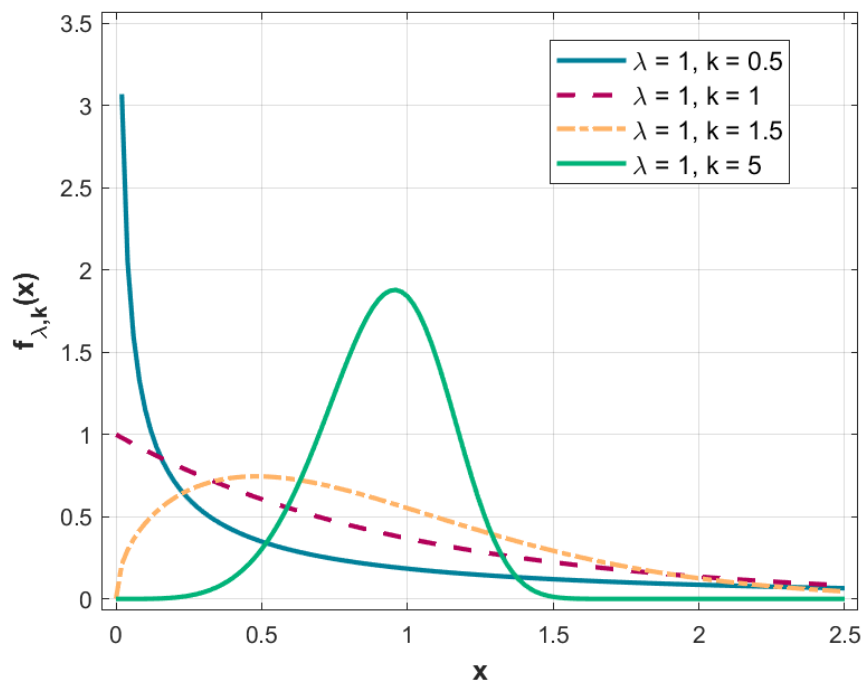


FIGURE 2.5: Plot of the probability density function for the Weibull Distribution.

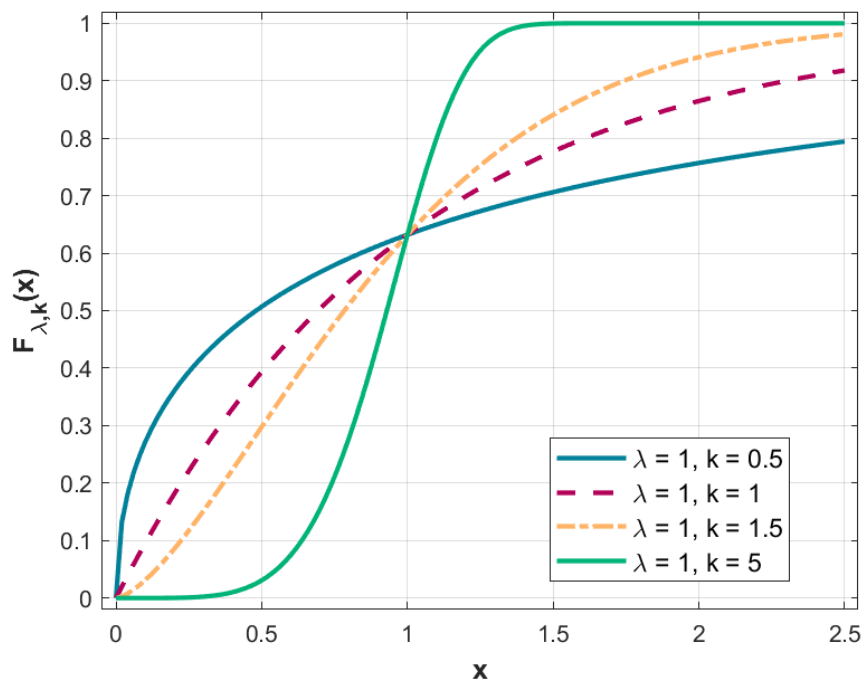


FIGURE 2.6: Plot of the cumulative distribution function for the Weibull Distribution.

2.1.5 Generalized Pareto Distribution (GPD)

The Pareto distribution is a family of distributions with two parameters. It has been successfully used to describe statistical problems related to finance, environmental phenomena such as the sizes of earthquakes or hydrology, or the interevent times or distances between such environmental disturbances. It is often used to model the tails of another distribution [68].

The probability density function (pdf) of $X \sim GPD(\mu, \sigma, \xi)$ is:

$$f_{(\mu, \sigma, \xi)}(x) = \frac{1}{\sigma} \left(1 + \frac{\xi(x - \mu)}{\sigma} \right)^{\left(-\frac{1}{\xi} - 1\right)},$$

where the support of x is $x \geq \mu$ when $\xi \geq 0$, and $\mu \leq x \leq \mu - \sigma/\xi$ when $\xi < 0$.

The cumulative distribution function of $X \sim GPD(\mu, \sigma, \xi)$ ($\mu \in \mathbb{R}$, $\sigma > 0$, and $\xi \in \mathbb{R}$) is

$$F_{(\mu, \sigma, \xi)}(x) = \begin{cases} 1 - \left(1 + \frac{\xi(x - \mu)}{\sigma} \right)^{-1/\xi} & \text{for } \xi \neq 0, \\ 1 - \exp\left(-\frac{x - \mu}{\sigma}\right) & \text{for } \xi = 0, \end{cases}$$

where the support of X is $x \geq \mu$ when $\xi \geq 0$, and $\mu \leq x \leq \mu - \sigma/\xi$ when $\xi < 0$.

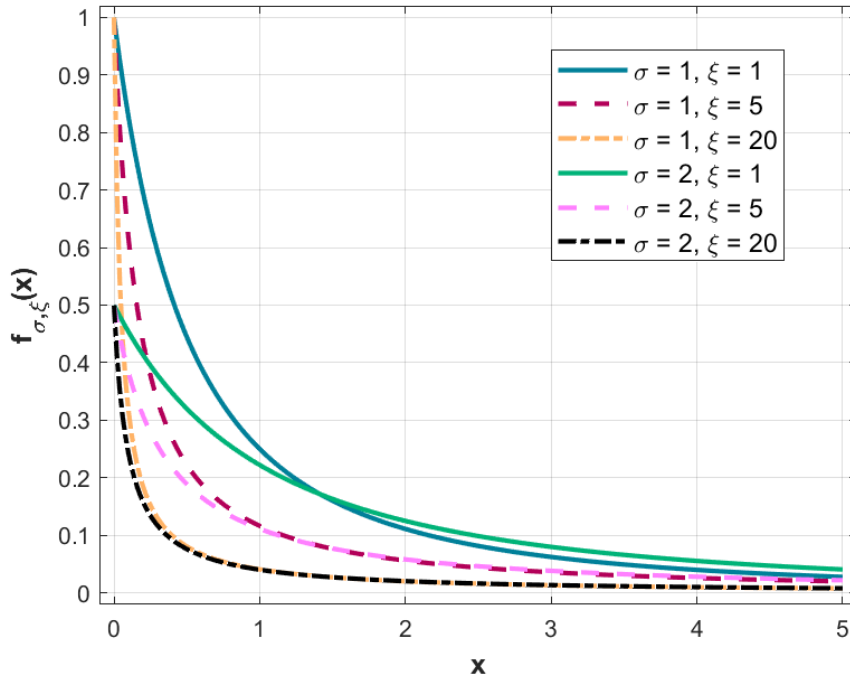


FIGURE 2.7: Plot of the probability density function for the Paareto Distribution.

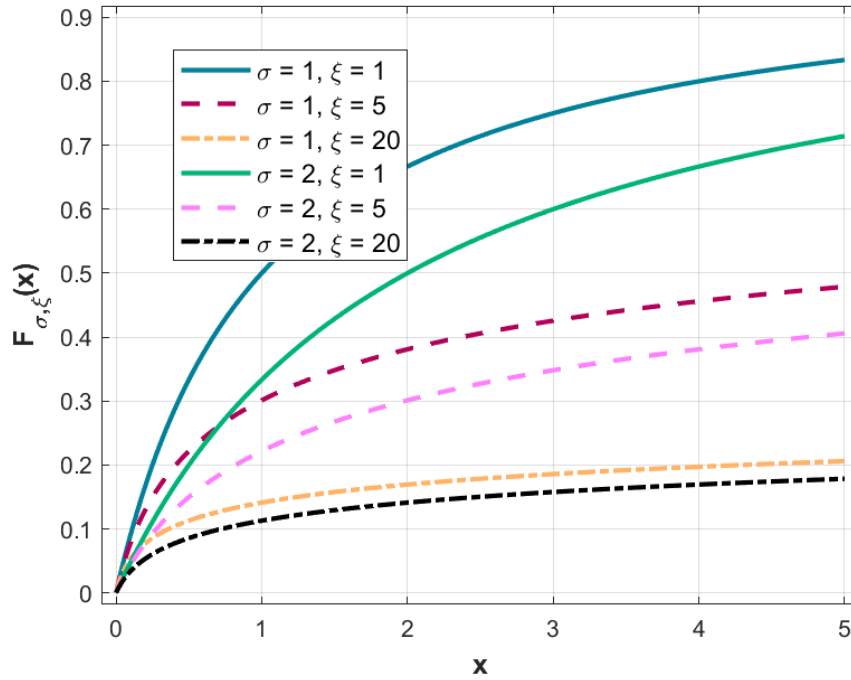


FIGURE 2.8: Plot of the cumulative distribution function for the Pareto Distribution.

2.1.6 Exponential Distribution

The probability density function (pdf) of the exponential distribution is

$$f(x; \lambda) = \begin{cases} \lambda e^{-\lambda x} & x \geq 0, \\ 0 & x < 0 \end{cases}$$

where $\lambda > 0$ is usually the rate parameter. The distribution is supported on the interval $[0, \infty)$. If a random variable X has this distribution, we write $X \sim \exp(\lambda)$.

The cumulative distribution function is given by

$$F(x; \lambda) = \begin{cases} 1 - e^{-\lambda x} & x \geq 0, \\ 0 & x < 0. \end{cases}$$

The mean or expected value of an exponentially distributed random variable X with rate parameter λ is given by

$$E[X] = \frac{1}{\lambda}.$$

In light of the examples given above, this makes sense: if you receive phone calls at an average rate of 2 per hour, then you can expect to wait half an hour for every call.

The variance of X is given by

$$\text{Var}[X] = \frac{1}{\lambda^2}$$

so the standard deviation is equal to the mean.
The moments of X , for $n \in \mathbb{N}$ are given by

$$E[X^n] = \frac{n!}{\lambda^n}.$$

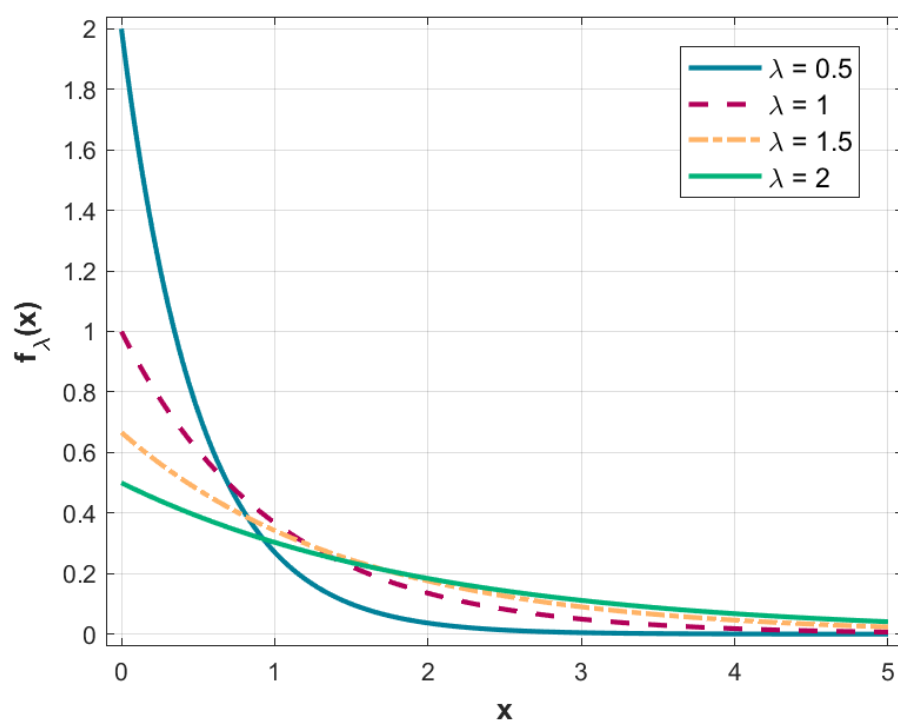


FIGURE 2.9: Plot of the probability density function for the Exponential Distribution.

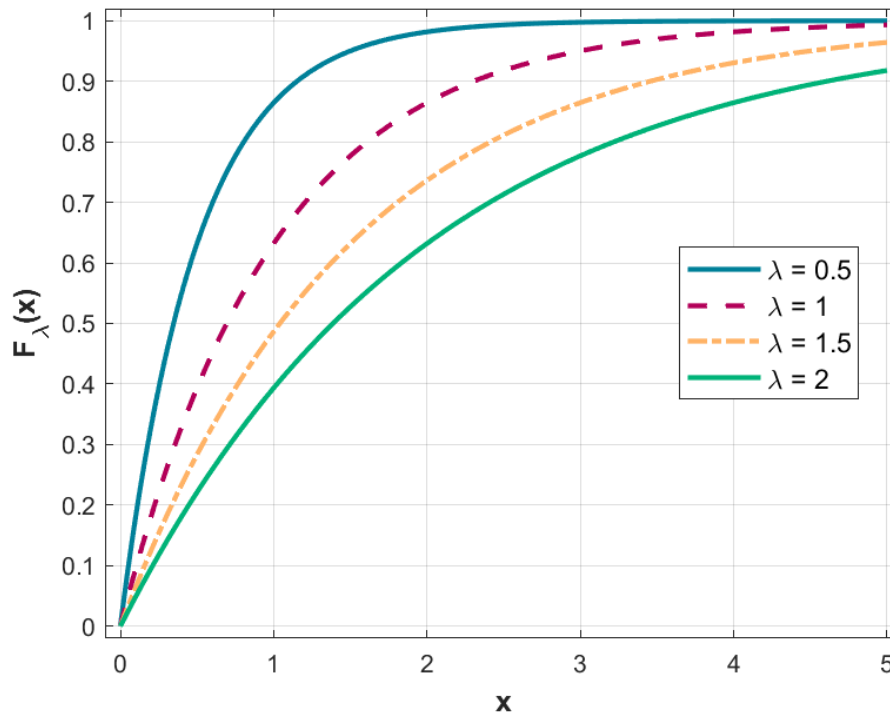


FIGURE 2.10: Plot of the cumulative distribution function for the Exponential Distribution.

2.1.7 Log-normal Distribution

In probability theory, a log-normal or lognormal distribution is a continuous probability distribution of a random variable whose logarithm is normally distributed. Thus, if the random variable X is log-normally distributed, then $Y = \ln(X)$ has a normal distribution. Equivalently, if Y has a normal distribution, then the exponential function of Y , $X = \exp(Y)$, has a log-normal distribution. A random variable which is log-normally distributed takes only positive real values [31].

Let Z be a standard normal variable, and let μ and $\sigma > 0$ be two real numbers. Then, the distribution of the random variable

$$X = e^{\mu + \sigma Z}$$

is called the log-normal distribution with parameters μ and σ . These are the expected value (or mean) and standard deviation of the variable's natural logarithm, not the expectation and standard deviation of X itself [31].

The probability density function (pdf) of a lognormal distribution is

$$f_x(x) = \frac{1}{x} \cdot \frac{1}{\sigma\sqrt{2\pi}} \exp\left(-\frac{(\ln x - \mu)^2}{2\sigma^2}\right),$$

where μ and σ are the expected value (or mean) and standard deviation, respectively.

The cumulative distribution function is given by

$$F_X(x) = \Phi \left(\frac{(\ln x) - \mu}{\sigma} \right),$$

where Φ is the cumulative distribution function of the standard normal distribution [31].

This may also be expressed as follows:

$$\frac{1}{2} \left[1 + \operatorname{erf} \left(\frac{\ln x - \mu}{\sigma\sqrt{2}} \right) \right] = \frac{1}{2} \operatorname{erfc} \left(-\frac{\ln x - \mu}{\sigma\sqrt{2}} \right),$$

where erfc is the complementary error function and μ and σ are the expected value (or mean) and standard deviation.

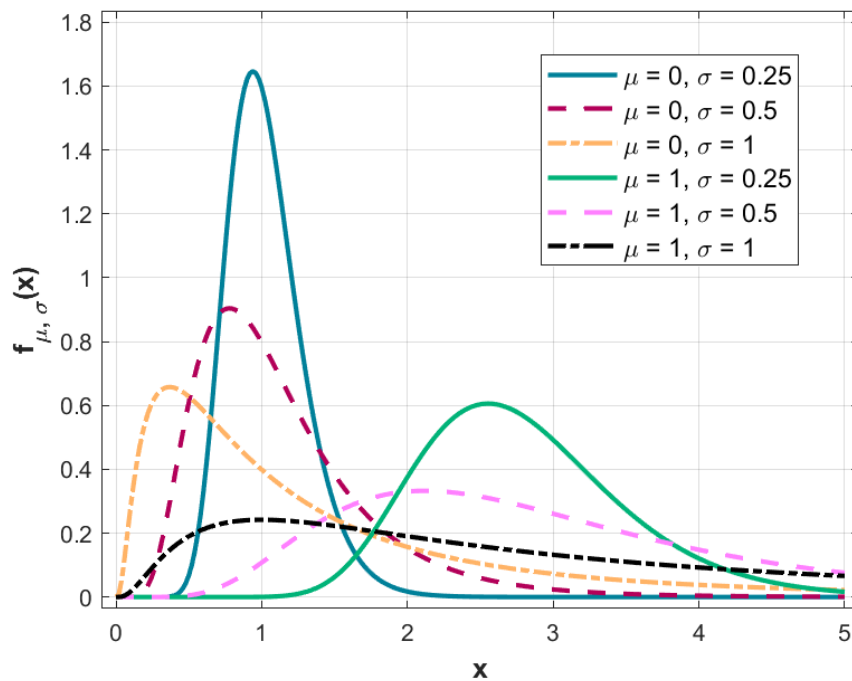


FIGURE 2.11: Plot of the probability density function for the Log-Normal Distribution.

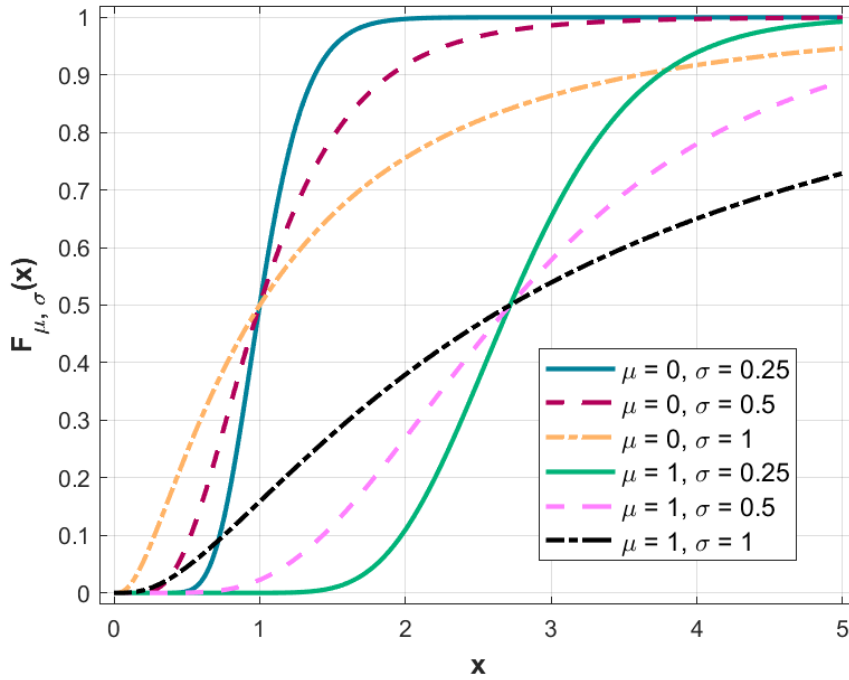


FIGURE 2.12: Plot of the cumulative distribution function for the Log-Normal Distribution.

2.2 Cross-Validation Error Measures

In order to assess the model performance certain statistical measures need to be evaluated. These measures include: the mean error (bias) (ME), the mean absolute error (MAE), the mean absolute relative error (MARE), the root mean square error (RMSE), the root mean square relative error (RMSRE), Pearson's linear correlation coefficient (RP) and Spearman (rank) correlation coefficient (RS). Below we define these measures in the case of leave-one-out cross validation. For the following measures, $x^*(\mathbf{s}_i)$ and $x(\mathbf{s}_i)$ are, respectively, the estimated (based on the $N - 1$ data that do not include point \mathbf{s}_i) and true value of the field at point \mathbf{s}_i , $\overline{x(\mathbf{s}_i)}$ denotes the spatial average of the data and $\overline{x^*(\mathbf{s}_i)}$ the spatial average of the estimates, while N is the number of observations.

Mean error (bias) (ME)

Mean error represents a systematic error in the process of data collection. It results in misleading results. This can occur in any of a number of ways, from calibration errors, sample bias to underestimation of earthquake magnitude due to the inability of measuring the total released energy (saturation).

The mean error (or bias) is calculated as follows:

$$\epsilon_{\text{bias}} = \frac{1}{N} \sum_{i=1}^N [x^*(\mathbf{s}_i) - x(\mathbf{s}_i)]. \quad (2.11)$$

Mean absolute error (MAE)

Mean absolute error (MAE) is a measure of errors between paired observations expressing the same phenomenon. The mean absolute error is calculated as follows:

$$\epsilon_{\text{MA}} = \frac{1}{N} \sum_{i=1}^N |x^*(\mathbf{s}_i) - x(\mathbf{s}_i)|. \quad (2.12)$$

Mean absolute relative error (MARE)

Mean absolute relative error (MARE) is a measure of prediction accuracy of a forecasting method in statistics, for example in trend estimation, In addition used as a loss function for regression problems in machine learning. The mean absolute relative error is calculated as follows:

$$\epsilon_{\text{MAR}} = \frac{1}{N} \sum_{i=1}^N \left| \frac{x^*(\mathbf{s}_i) - x(\mathbf{s}_i)}{x(\mathbf{s}_i)} \right|. \quad (2.13)$$

Root mean square error (RMSE)

Root mean square error (RMSE) is a frequently used measure of the differences between values (sample or population values) predicted by a model or an estimator and the values observed. The RMSE represents the square root of the second sample moment of the differences between predicted values and observed values or the quadratic mean of these differences. These deviations are called residuals when the calculations are performed over the data sample that was used for estimation and are called errors (or prediction errors) when computed out-of-sample. The root mean square error is calculated as follows:

$$\epsilon_{\text{RMS}} = \sqrt{\frac{1}{N} \sum_{i=1}^N [x^*(\mathbf{s}_i) - x(\mathbf{s}_i)]^2}. \quad (2.14)$$

Root mean square relative error (RMSRE)

Root mean square relative error (RMSRE) is relative to what it would have been if a simple predictor had been used. More specifically, this simple predictor is just the average of the actual values. Thus, the relative squared error takes the total squared error and normalizes it by dividing by the total squared error of the simple predictor. By taking the square root of the relative squared error one reduces the error to the same dimensions as the quantity being predicted. The root mean square relative error is calculated as follows:

$$\epsilon_{\text{RMSR}} = \sqrt{\frac{1}{N} \sum_{i=1}^N \left[\frac{x^*(\mathbf{s}_i) - x(\mathbf{s}_i)}{x(\mathbf{s}_i)} \right]^2}. \quad (2.15)$$

Pearson's Linear correlation coefficient (RP)

The correlation coefficient, ρ , is the statistic that is most commonly used to summarize the relationship between two variables. The formula for Pearson's linear correlation coefficient ρ is [30]

$$\rho_{X,Y} = \frac{\text{cov}(X, Y)}{\sigma_X \sigma_Y} = \frac{E[(X - \mu_X)(Y - \mu_Y)]}{\sigma_X \sigma_Y}.$$

In case of cross-validation for a sample of size N , ρ is defined as

$$\bar{\rho}_{X,X^*} = \frac{\sum_{i=1}^N [x(\mathbf{s}_i) - \bar{x}(\mathbf{s}_i)] [x^*(\mathbf{s}_i) - \bar{x}^*(\mathbf{s}_i)]}{\sqrt{\sum_{i=1}^N [x(\mathbf{s}_i) - \bar{x}(\mathbf{s}_i)]^2} \sqrt{\sum_{i=1}^N [x^*(\mathbf{s}_i) - \bar{x}^*(\mathbf{s}_i)]^2}}.$$

The correlation coefficient measures the dispersion of estimates with respect to the observed values. This relation can best be illustrated in terms of a scatterplot. If $\rho = +1$, the scatterplot is a straight line with a positive slope; if $\rho = -1$, the scatterplot is a straight line with a negative slope. For $|\rho| < 1$ the scatterplot appears as a cloud of points that becomes more diffuse as $|\rho|$ decreases from 1 to 0 [30].

Spearman (rank) correlation coefficient (RS)

It is important to note that ρ provides a measure of the linear relationship between two variables. If the relationship between two variables is not linear, the correlation coefficient may be a very poor summary statistic. It is often useful to supplement the linear correlation coefficient with another measure of the strength of the relationship, the rank correlation coefficient. To calculate the rank correlation coefficient, one applies Eq. (2.2) to the ranks of the data values rather than to the original sample values:

$$\rho_{rank} = 1 - \frac{6 \sum_{i=1}^N (R_{x_i} - R_{y_i})^2}{N(N^2 - 1)}, \quad (2.16)$$

where R_{x_i} is the rank of x_i among all the other x values. The rank is usually calculated by sorting the x values in ascending order; the rank of a given value is equal to its order of appearance in the sorted list. The lowest x value appears first on a sorted list and therefore receives a rank of 1; the highest x value appears last on the list and receives a rank of N .

Large differences between ρ_{rank} and ρ are often quite revealing about the existence of extreme pairs on the scatterplot. Unlike the traditional correlation coefficient, the rank correlation coefficient is not strongly influenced by extreme pairs. Large differences between the two may be due to the location of extreme pairs on the scatterplot. A high value of ρ_{rank} and a low value of ρ may be due to the fact that a few erratic pairs have adversely affected an otherwise good correlation. If, on the other hand, it is ρ that is quite high while ρ_{rank} is quite low, then it is likely that the high value of ρ is due largely to the influence of a few extreme pairs.

Differences between ρ and ρ_{rank} may In addition reveal important features of the relationship between two variables. If the rank correlation coefficient is +1, then the ranks of the two variables are identical: the largest value of x corresponds to the largest value of y , and the smallest value of x corresponds to the smallest value of y .

The value of ρ is often a good indicator of how successful we might be when trying to predict the value of one variable from the other with a linear equation. If $|\rho|$ is large, then for a given value of one variable, the other variable is restricted to only a small range of possible values. On the other hand, if $|\rho|$ is small, then knowing the value of one variable does not help us very much in predicting the value of the other [30].

2.3 Linear Regression

Regression analysis is a powerful and commonly used statistical method that allows to examine the relationship between two or more variables of interest. Linear regression attempts to find a relation between two variables by fitting a linear equation to observed data. More precisely, it is the process of finding a line that best fits the data points available on the plot. In that way we can use it to predict output values for inputs that are unavailable in the data set we have, with the confidence that those outputs would fall on the line. The simplest form of the regression equation with one response variable and one predictor variable is defined by the formula

$$y = a + b \cdot x, \quad (2.17)$$

where y denotes the estimated response or dependent variable score, a is a constant, b is the regression coefficient, and x is the score on the predictor or independent variable.

While there are many types of regression analysis, at their core they all examine the influence of one or more predictor variables on a response variable. For more than one independent variable, the process is called multiple linear regression [16].

In linear regression, the relations are modeled using linear predictor functions whose unknown model parameters are estimated from the data. Such models are called linear models. Most commonly, the conditional mean of the response given the values of the explanatory variables (or predictors) is assumed to be an affine function of those values; less commonly, the conditional median or some other quantile is used [16].

2.3.1 Ordinary Least Squares (OLS)

The most commonly tested and the simplest technique for establishing a linear relation between two variables is the Ordinary least squares (OLS) fitting. OLS regression is a statistical method of analysis that estimates the relationship between one or more independent variables and a dependent variable. The method estimates the relationship by minimizing the sum of

the squares in the difference between the observed and predicted values of the dependent variable configured as a straight line.

The sum of squared residuals (SSR), also called the error sum of squares (ESS) or residual sum of squares (RSS), is a measure of the overall model fit:

$$S(b) = \sum_{i=1}^n (y_i - x_i^T b)^2 = (y - Xb)^T (y - Xb),$$

where T denotes the matrix transpose, and the rows of X, denoting the values of all the independent variables associated with a particular value of the dependent variable, are $X_i = x_i^T$. The value of b which minimizes this sum is called the OLS estimator for β [23].

2.3.2 Weighted Least Squares (WLS)

In this study weighted least squares method was used to determine a relation between two different magnitude scales. It is also called Weighted Linear Regression and it is consider an extension of Ordinary Least Squares regression in which the errors covariance matrix ¹ is allowed to be different from an identity matrix. Non-negative weights are attached to data points. It is used when we have a situation where data points should not be treated equally.

The determination of the correct weight can be a really challenging task. Usually as ideal weight is consider the reciprocal of the variance of the error. However, this is in most situations incalculable and other approaches must be used.

The squared predictor or the reciprocal of a predictor if the variance is proportional to a predictor. It needs experience combined with trial and error to determine what works. Values based on literature, theory or previous research.

In most cases, observations with large variances should have relatively small weights and observations with small variances should have relatively large weights. Specifying a column of weights does not affect the degrees of freedom. However, if you specify a weight of zero for one or more observations, it will remove it from the analysis and thus decreases your degrees of freedom [42].

2.4 Bootstrapping

In statistics, bootstrapping is any metric or test that is based on random sampling with replacement. Bootstrapping is a technique that allows assigning measures of accuracy (defined in terms of variance, bias, prediction error, confidence intervals or some other such measure) to sample estimates.

¹is a square matrix giving the covariance between each pair of elements of a given random vector. [80].

It allows estimation of the sampling distribution of almost any statistic using random sampling methods [79].

Simplicity is a great advantage of bootstrap. It is a straightforward way to derive estimates of confidence intervals and standard errors for complex estimators of complex parameters of the distribution. Such as percentile points, odds ratio, proportions and correlation coefficients. Bootstrap is an appropriate way to check and control the stability of the results [14]. Despite the fact that for most problems it is impossible to know the precise confidence interval, bootstrap method is asymptotically more accurate. Especially, in comparison with the standard intervals obtained using assumptions of normality and sample variance. In addition, bootstrapping is a convenient method because it avoids the cost of repeating the experiment to get other different groups of sample data.

While bootstrapping is, under some conditions, asymptotically consistent, it does not give general finite-sample guarantees. It is possible for the results to depend on the representative sample [14]. The apparent simplicity may conceal the fact that important assumptions are being made when undertaking the bootstrap analysis (e.g. independence of samples) where these would be more formally stated in other approaches. In addition bootstrapping method can be time-consuming.

2.5 Maximum Likelihood Method

The Maximum likelihood estimation method (*MLE*) is an indispensable tool used for parameter estimation and is preferred for a variety of mathematical modelling techniques when the data is non-normal [43]. Suppose that x_i are independent and identically distributed values, then the likelihood is defined as:

$$L(\theta) = \prod_{i=1}^n f(x_i | \theta),$$

where $L(\theta)$ signifies the observing probability for the given data as a function of θ . In order to maximize the product of the previous function, we maximize the log likelihood, using the fact that the logarithm is an increasing function:

$$l(\theta) = \sum_{i=2}^n \log(f(x_i | \theta)),$$

This method can be performed on data so as to extract as much information as possible [43].

2.5.1 Information Criteria

Information criteria are useful for model selection. In this thesis those criteria are used to determine which distribution model is most appropriate for a given set of interevent times between successive earthquakes. The mathematical expressions of these criteria are written below:

- AIC : Akaike Information Criterion
The AIC approach aims to clarify the best fitted model of the observed data via the principles of MLE and negative entropy ¹.

$$AIC = -2 \log L(\theta) + 2k \quad (2.18)$$

- BIC : Bayesian Information Criterion
The BIC approach aims to identify the best fitted model of the observed data by comparing probabilities, under the consideration that each of the candidate models is the true model [7].

$$BIC = -2 \log L(\theta) + k \log(n) \quad (2.19)$$

Concisely, both criteria can be used in order to reassure the robustness of a model's fit. These criteria are giving optimal model selection results under defined conditions, whereas fail to fully describe the complexity of a real model problem. Hence, the understanding of the nature of the problem is necessary.

2.6 Statistical Methods Used to Estimate the Magnitude of Completeness.

The magnitude of completeness is defined as the lowest magnitude above which all of the earthquakes in a specific area are detected. A correct estimate of M_c is crucial, since a value too high leads to under-sampling, by discarding usable data, while a value too low leads to erroneous seismicity parameters.

In seismicity studies, it is frequently necessary to use the maximum number of events available for high-quality results.

There are two methods for calculating the M_c . The first is based on the properties of the seismic network, while the second is based on earthquake lists. In addition there are two groups of M_c estimation methods based on earthquake lists. The first assumes that during night there is a lower detectability limit of earthquakes, due to the lack of noise [83]. Therefore, the M_c is determined by calculating the ratio of the frequency of earthquakes that were occurred by day to those occurred by night. The second is based on the auto-correlation of the process of generating earthquakes. In this way, the frequency-magnitude distribution of earthquakes can be simulated by the Gutenberg-Richter power law (G-R).

In this analysis, three different methods were chosen, based on earthquake lists method, to estimate the magnitude of completeness. Those statistical methods are the Maximum curvature method (MAXC), the Goodness-of-fit (GFF), and the Entire magnitude range (EMR) method.

¹Measure of divergence of normality [7].

2.6.1 Maximum Curvature (MAXC)

The Maximum Curvature technique (MAXC) [84] is a fast and straightforward way to estimate the magnitude of completeness M_c by defining the point of the maximum curvature by computing the maximum value of the first derivative of the frequency-magnitude curve. In practice, this matches the magnitude bin with the highest frequency of events in the non-cumulative FMD. Despite the easy applicability of this approach, M_c is underestimated in the case of gradually curved FMDs, and the use of other techniques providing more conservative estimates, such as GFF or EMR, has been suggested [81], [83]). However, Mignan *et al.* [47] showed that MAXC does not underestimate M_c when considering a local data set in which heterogeneities in M_c are minimized. The MAXC technique has, moreover, the advantage of requiring fewer events than other techniques to reach a stable result [47].

2.6.2 Goodness-of-fit (GFF)

The Goodness-of-fit test (GFF), proposed by Wiemer and Wyss [81], calculates the magnitude of completeness (M_c) by comparing the observed frequency magnitude distribution (FMD) with synthetic ones. The goodness-of-fit is evaluated by the parameter R, the absolute difference of the number of events in each magnitude bin between the observed and synthetic G-R distributions. Synthetic distributions are calculated using the estimated a and b-values of the observed data set.

The measurements of goodness of fit of a statistical model is an essential step on data analysis in order to examine if the initial hypotheses about the observation process fit a model adequately as well as if we can consider it consistent with those hypotheses.

2.6.3 Entire Magnitude Range (EMR)

Woessner and Wiemer [83] proposed a method to estimate the magnitude of completeness (M_c) that uses the entire magnitude range (EMR), thus including events below M_c . They provided a model consisting of two parts: the G-R law for the complete part, and the cumulative normal distribution for the incomplete part of the non-cumulative FMD. The model attempts to reproduce the entire frequency-magnitude distribution, thus fits the incompletely observed part, a technique, which has been questioned.

The main distinction is whether they are parametric (GFT, EMR) or non-parametric (MAXC). Parametric techniques are based on fitting the FMD while non-parametric techniques are based on the evaluation of changes in the FMD (e.g., possible breaks in the slope). The above methods provide reasonable values for all data sets and can be used for the magnitude of completeness determination.

2.7 Statistical Properties and Measurement of Earthquakes

Any sudden movement of the Earth's lithosphere is defined as an earthquake. Characteristics such as the size, the duration, the focal depth, the vibrations caused by an earthquake, e.g; vary each time and are those to describe the singularity of each earthquake. An earthquake can be roughly characterized by magnitude size and intensity measure. To keep track of an earthquake, the seismic waves, which are released need to be measured by precise devices, called seismographs. Magnitude is determined in seismograms from measurements on seismographs and describes the energy, released at the source of the earthquake. At the same time, intensity measures the strength of vibration produced by the earthquake at a certain location.

2.7.1 Seismograph, Seismogram and Seismometer

It is essential to perceive how earthquakes are being recorded in order to understand how they are measured. To record seismic waves and measure their intensity, geologists use special measuring devices sensitive to vibrations which called seismographs. Seismographs can detect movements of the Earth's surface.

Generally, a seismograph consists of a weight, called mass attached to a fixed base, and works on the principle of a pendulum: a heavy, inert mass with a certain resistance to movement, inertia, due to its weight is suspended from a frame by a spring that allows movement. The energy from any seismic activity excites this "proof mass" as it is called by geophysicists, making it vibrate. The base moves and the mass does not. The relative motion between the mass and the frame provides a measurement of the vertical ground motion. A rotating drum is attached to the frame and a pen is attached to the mass, recording any ground motion in a seismogram (Fig. 2.13).

The wide variety of ground motion, both in terms of the amplitude and the vibration period of oscillation make it impossible for a single seismographs to record all different types of motion. Therefore, gathering the records of many stations, geologists can investigate the propagation of seismic waves and study the distribution of seismic energy in space and time.

Nowadays research seismographs are electronic and are called seismometers. As a substitute for the drum and the pen, the relative motion between the weight and the frame generates an electrical voltage that is recorded by a computer. By modifying the arrangement of the spring, frame, and weight, seismographs are able to record motions in all directions. Furthermore, seismographs commonly record ground motions caused by a wide variety of natural and human-made sources, such as cars and trucks on the highway, trees blowing in the wind and ocean waves crashing on the beach. That ground motion is considered as noise and it needs to be removed from the seismogram.

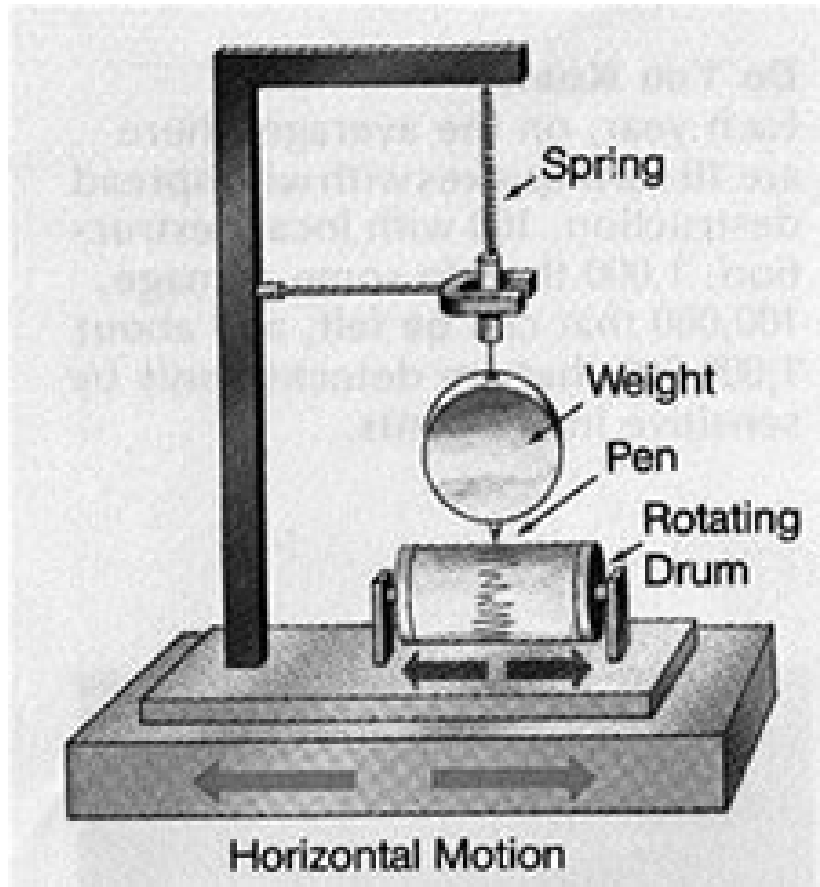


FIGURE 2.13: Seismograph an instrument which detects and records ground motion (and especially vibrations due to earthquakes) along with timing information. Retrieved from [52].

2.7.2 Energy Release

All earthquakes in nature are radiating energy in the form of different kinds of seismic waves. Those seismic waves consist of individual characteristics that reflect the surface they travel through, which in this case is the Earth's crust, and the nature of the rupture.

The determination of magnitude, occurred by an earthquake, generally involves identifying specific kinds of these waves and then measuring some of their characteristics, such as its amplitude, timing, frequency, orientation, or duration [19]. As the energy is released from an earthquake, it transmit in many different frequencies. In order to calculate an accurate value of energy or magnitude, it is necessary to include all those frequencies of shaking for the entire event.

Seismologists have determined that the energy radiated by an earthquake is a function of both the duration and the amplitude of the waves of the earthquake. A very small event is over in less than a second, while for a greater earthquake, the fault may continue to slip for more than 300 seconds.

Using the empirical formula, developed by Bath [8], the energy release

can be roughly estimated by converting the moment magnitude to energy according to this equation:

$$\log E = 5.24 + 1.44M_w, \quad (2.20)$$

where M_w is the moment magnitude (see 3.1.2) and E , energy is expressed in units of joules. This equation was established for earthquakes with moment magnitude greater than 5 M_w .

By applying equation (2.20), the energy released by a 5 M_w earthquake is about 2.8×10^{12} joule. A 6 M_w earthquake releases 7.8×10^{13} joules, and a 7 M_w radiates 2.1×10^{15} joules.

For comparison reasons the bomb dropped on Hiroshima released about 7.4×10^{12} joules.

Some other empirical studies [33] have stated that, energy is proportional to local magnitude according to this relation:

$$E = 10^{1.5M_L},$$

where M_L (see 3.1.1) is the local magnitude.

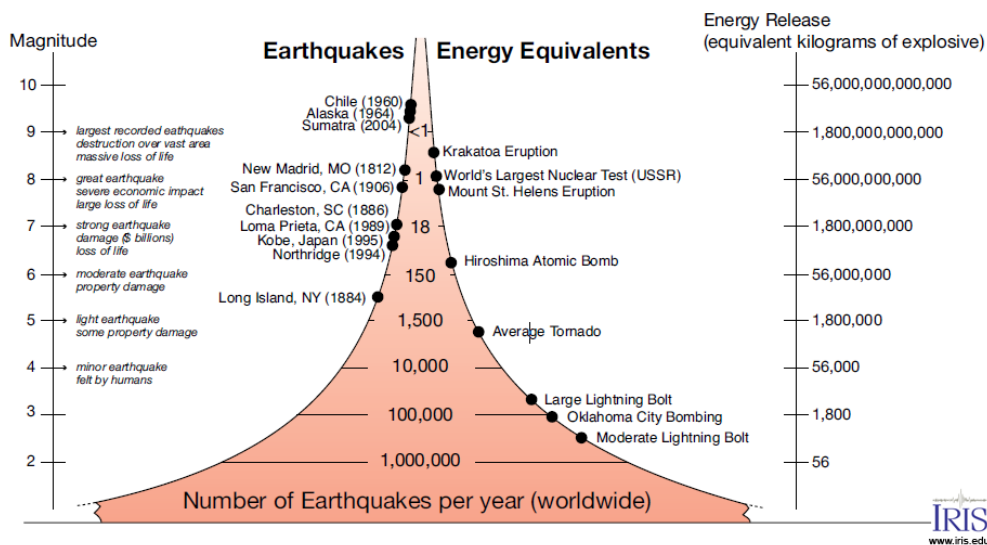


FIGURE 2.14: Correlation between the number of earthquakes and their magnitude with an energy release equivalent (in kg of TNT). Downloaded from [29]. The right side of the figure represents the amount of high explosive (TNT) required to produce the energy released by the earthquake. Equally, the left side of the figure illustrates the magnitude scale, which is determined by the amount of energy released at the hypocenter.

In the Fig. 2.14 we can observe the exponential increase of the energy radiate in comparison with the increasing magnitude values. We notice the number of earthquakes strike worldwide per year and compare it with the magnitude and the energy released. For example, each year approximately

1000000 earthquakes with magnitude 2 M_L are recorded while for 5 M_L around 1500. An earthquake of 5 M_L and 7 M_L can be as deadly as the energy released from approximately 1800000 kg and 1800000000 kg of explosive, respectively. In addition, some catastrophic earthquakes that have marked history during the centuries are presented.

2.7.3 Intensity

Apart from the energy released when an earthquake occurs, another measurement can describe it, this is the intensity of the earthquake. Every earthquake comes in hand with a ground motion shaking. That shaking is measured as the intensity of an earthquake. The shaking at each location depends on the distance from the fault rupture area and varies from one area to another. However, intensity can be affected not only by the rupture distance of each different location but in addition from the direction the earthquake ruptured and the different type of surface morphology and geology. Whereas the magnitude of an earthquake is one value that describes the size, there are many intensity values for each earthquake distributed across the geographic area around the earthquake epicenter.

The intensity scale used, is called the Mercalli Intensity Scale. Intensities are expressed in Roman numerals, for example, VI, X, etc. It starts from intensity one (I) described as “Not felt” and ends up in intensity twelve (XII) described as “Extreme”. Traditionally, the intensity is a subjective measure derived from observations and reports which are made not by instruments but by humans. Those observations describe the felt shaking and structural damage. Those observations have been particularly useful in estimating the relative severity of historical earthquakes that were not recorded by any seismographs or did not occur in populated areas.

The correlation between magnitude and intensity is not absolute. It depends on several factors, including the hypocenter’s depth, the distance from the epicenter, the terrain, and faults. For example, an earthquake, according to USGS, [77] with a magnitude 4.5 in Salta, Argentina, 2011, was 164 km deep and had a maximum intensity of I. While an earthquake in Barrow in Furness, England, 1865 which was measured as a 2.2 magnitude with a depth about 1 km, had a maximum intensity of VIII [46].

Chapter 3

Empirical Relations and Laws of Seismology

In order to study earthquakes and apply the laws of seismology we must first find a way to measure the size of earthquakes. The relative size that characterizes an earthquake is defined as magnitude. Magnitude is based on the measurement of the maximum motion recorded by a seismograph or seismometer. Several scales have been defined for numerous reasons and are explained in detail in the following chapter.

3.1 The Concept of Magnitude and its Different Scales

Charles Richter [65] was the pioneer to conceive the idea of the local magnitude scale of earthquakes, labeled as M_L , in 1935 and published it in the Bulletin of the Seismological Society of America.



FIGURE 3.1: Charles Richter with his seismograph, 1976 Caltech.

3.1.1 Local Magnitude, M_L

According to Richter [66], the magnitude of an earthquake M_L is defined as the logarithm (to base 10) of the maximum amplitude A_0 traced on a

seismogram by a standard torsion horizontal-component seismograph, at distant 100 km from the epicentre.

The original formula is:

$$M_L = \log_{10} A - \log_{10} A_0(\Delta) = \log_{10}[A/A_0(\Delta)], \quad (3.1)$$

where A is the maximum excursion of the Wood–Anderson seismograph, A_0 is the distance-correction function that reflects the overall attenuation attributes in the region of interest, and Δ is the distance from the event (in kilometers unless otherwise specified).

Because of the logarithmic basis of the scale, each whole number increase in magnitude represents a tenfold increase in measured amplitude (shown in Fig. 3.2). In terms of energy, each whole number increase corresponds to an increase of about 31.6 times the amount of energy released, and each increase of 0.2 corresponds to approximately a doubling of the energy released.

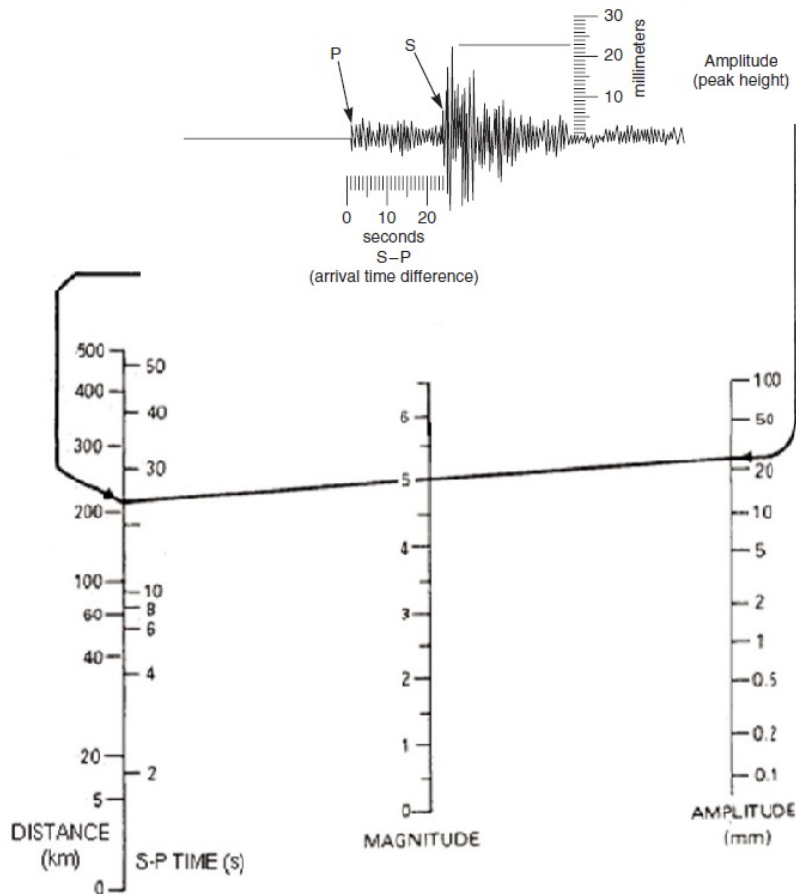


FIGURE 3.2: Procedure for calculating the magnitude. Connecting the amplitude of the seismic wave (shown on the right) with distances calculated from S minus P arrival times gives us the Richter's magnitude scale. The scale is logarithmic, which means that one increase in magnitude correspond to ten times larger amplitude. Retrieved from [66]

As the number of seismograph stations was increased all around the world, it became apparent that the Richter's local magnitude scale, was strictly valid only for certain frequency and distance ranges. In order to take advantage of that global growth, new magnitude scales (Fig. 3.1) that are an extension of Richter's original definition were created. The different magnitude scales represent various ways of deriving the size of an earthquake from different information of seismic waves. The logarithmic scale is retained to all magnitudes and they are adjusted so that the mid-range approximately correlates with the original Richter scale or local magnitude scale.

TABLE 3.1: Symbols used to indicate different magnitudes.

Magnitude definition	
M_L	local magnitude
M_s	surface wave magnitude
M_w	moment magnitude
M_o	seismic moment
M_e	energy magnitude
m_b	body magnitude

Since 2005, the International Association of Seismology and Physics of the Earth's Interior [28] has standardized the measurement procedures and equations (described in the following section) for the principal magnitude scales, M_L , M_s , m_s and M_w .

3.1.2 Different Scales of Magnitude

Moment Magnitude, M_w

In 1979, Hanks and Kanamori introduced the scale of moment magnitude, which became the most commonly used method of describing the size of an earthquake [22]. Moment magnitude measures the size of events in terms of how much energy is radiated. Specifically, moment magnitude relates to the amount or better the distance of movement along a fault or fracture and the area of the fault or fracture surface. Since moment magnitude can describe something physical about the event, calculated values can be easily compared to magnitude values for other events. As it is derived from the seismic moment, M_o is a reliable estimate of the magnitude since it is calculated using much longer periods; the attenuation is not greatly affected by near-surface structure [33]. Further, full waveform modelling eliminates the variability of the radiation pattern. The formula that Kanamori [34] proposed is the following :

$$M_w = \frac{2}{3} \log_{10} M_o - 10.7, \quad (3.2)$$

where M_o is the seismic moment of earthquake in dyn·cm. The moment magnitude has the advantages (as a measure of size in earthquakes) that it

does not saturate at the top of the scale, and has a sounder theoretical basis than other magnitude scales. The saturation process is described in section 3.1.3.

Seismic Moment, M_o

The seismic moment M_o is an indispensable earthquake parameter because it measures the total deformation at the source. Seismic moment is measured in units of Newton meters (N·m) or Joules, or (in the older CGS system) dyne·centimeters (dyn·cm).

It is a quantity, generated by a slipping fault, which is used to measure the amount of energy released by an earthquake [38]. The seismic moment is roughly defined as:

$$M_o = \text{rigidity} \cdot \text{fault area} \cdot \text{fault slip.} \quad (3.3)$$

The rigidity (or resistance) is a number that characterizes the stiffness of rocks near the fault, while fault area and fault slip can be estimated from the analysis of seismograms.

Historically, the first calculation of an earthquake's seismic moment from its seismic waves was made by Keiiti Aki for the 1964 Niigata earthquake [2]. First, he used data from distant stations of the World-Wide Standardized Seismograph Network (WWSSN) to analyze long-period (200 seconds) seismic waves (wavelength of about 1000 km) to determine the magnitude of the earthquake's equivalent double couple. Additionally, he drew upon the study of Burridge and Knopoff on dislocation to determine the amount of slip, the energy released, and the stress drop (essentially how much of the potential energy was released) [15]. In that way, he derived the Eq. (3.3), which relates an earthquake's seismic moment to its physical parameters. Hence, according to Aki Eq. (3.3) is defined more detailed as:

$$M_o = \mu \cdot \bar{u} \cdot S, \quad (3.4)$$

where μ is the rigidity (or resistance) when moving a fault with surface area S over an average dislocation (distance) \bar{u} . Modern formulations replace $\bar{u} \cdot S$ with the equivalent $\bar{D} \cdot A$, known as the “potency” or “geometric moment”.

Kanamori studied great earthquakes from all around the world, spanning 15 years from 1950 to 1965, and established a new magnitude relation between seismic moment and moment magnitude [34]:

$$\log M_o = \frac{3}{2} M_w + 10.7, \quad (3.5)$$

where M_o is the seismic moment in dyn·cm (equal to $10^7 Nm$) and M_w the moment magnitude. The constants in this equation allows the moment magnitude scale to describe great earthquakes while matching other magnitude scales such as the local magnitude and the surface wave magnitude, at smaller scale magnitudes. An earthquake with M_w equal to or greater than 8.0, which on average occurs about every 1.5 years, is classified as a

great earthquake. An alternative definition for seismic moment M_o is given in terms of the torque that results in inelastic (permanent) displacement or distortion of the earth's lithosphere [37]. Nevertheless, the seismic moment is regarded as the fundamental measure of an earthquake's size and is considered as more direct than other parameters.

Surface and Body Wave Magnitude, M_s and m_b

For large earthquake events, government earthquake monitoring agencies, such as the United States Geological Survey [77] and the Japan Meteorological Agency, often provide initial earthquake magnitudes to the public by using the body-wave and surface-wave scales first. Earthquake magnitude calculations using these methods are less complex than determining the moment magnitude, M_o and they allow these agencies to rapidly report an earthquake's relative size to the public. As time and resources allow, earthquake magnitudes are adjusted later by using the moment magnitude scale.

The surface wave magnitude M_s , according to Gutenberg [19] is defined, for shallow focus earthquakes, as:

$$M_s = \log_{10} A + \alpha \log_{10}(\Delta) + \beta, \quad (3.6)$$

where A is the maximum amplitude of the ground motion for surface waves having 20 s period, and Δ is the distance from the event. Representative values of α and β for the horizontal component of Rayleigh waves from shallow earthquakes are 1.66, and 1.82, respectively [75].

For deep earthquakes, Eq. (3.6) is not applicable and body wave magnitudes must be defined. The most commonly used formula, proposed by Gutenberg and Richter (1956) [66], to calculate the body wave magnitude m_b is:

$$m_b = \log_{10}(A/T) + Q(h, \Delta), \quad (3.7)$$

where A is the maximum amplitude (μm), T is the measured wave period (*sec*) and Q is an empirical function of focal depth that depends on distance from the event Δ and depth of the event h (tables of Q are used) .

The empirical relation between m_b and M_s for shallow earthquakes is defined as [75] :

$$m_b = 2.5 + 0.63M_s. \quad (3.8)$$

Surface wave magnitude, M_s is found to be a strong function of wave frequency and tends to an upper limit for great earthquakes while, the moment magnitude, M_w provides a more uniform scale. The empirical relations were extended to cover earthquakes of significant focal depth and to enable independent magnitude estimates from body and surface wave observations.

3.1.3 Saturation on Magnitude Scales

Most magnitude scales are incomplete because they are obtained from partial seismic wave-train generated by an earthquake. This results in a systematic underestimation of magnitude in certain cases, a condition called saturation.

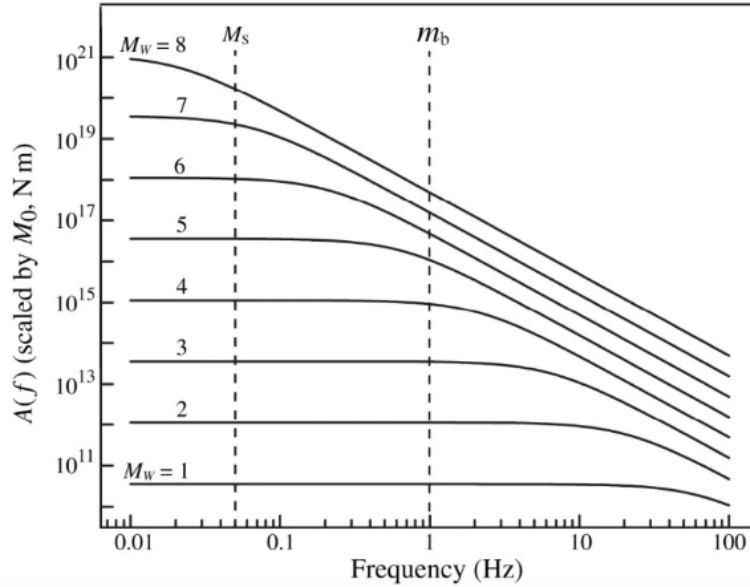


FIGURE 3.3: Saturation of moment magnitude, surface and body wave magnitudes. Retrieved from [66]

The effect of underestimating the magnitude, in different scales, is illustrated in Fig. 3.3 and reflect the underestimation of the dimensional size or strength (potential shaking) of the earthquake. Magnitude saturation also occurs in body-wave magnitude (m_b) and surface-wave magnitude (M_s) estimations as earthquake magnitudes approach or exceed magnitude 8. More accurately, a systematic underestimation of magnitude concerning a true non-saturating moment grows linearly and everywhere, with the same slope proportional to M_0 . The underestimation of a non-reference magnitude is then due to the slower increase of its related measurement amplitudes with growing M_w when they are measured at frequencies outside the displacement plateau. For example, for earthquake events estimated using the original Richter scale, those that are greater than 6.5 are miscategorized as 6.5 M_L earthquake events. Magnitude saturation was the reason that the Chile earthquake of 1960 was initially registered as a 8.3 magnitude event on the surface-wave magnitude scale before it was recalculated a few years later with the moment magnitude scale as a 9.5 magnitude event.

Although local magnitude, M_L may saturate for large earthquakes, it was introduced as a way to quantify earthquake size by measuring the peak value of ground motion at local to regional distance. The fact that the local magnitude is computationally inexpensive to calculate has made it an indispensable part of routine processing in seismological observatories. On the contrary, moment magnitude, M_w is based on the seismic moment M_0 ,

a physical quantity proportional to the energy released by a seismic source, therefore it does not saturate even for very large earthquakes [22].

Seismicity studies require homogeneous earthquake catalogs, that is, catalogs in which earthquake magnitudes are expressed on the same scale and preferably in the moment magnitude scale, M_w . Unfortunately, the calculation of seismic moment, M_0 , which leads to M_w is more demanding computationally and is usually achieved after inversion of regional or teleseismic wave forms of earthquakes exhibiting significant energy in lower frequencies (< 0.1 Hz). As a result, moment magnitudes are available for only a limited number of strong and recent earthquakes. To overcome this problem, many seismologists proposed empirical relations. Papazachos [60] proposed relations custom made for the Greek region. Thus, it is easier to estimate moment magnitudes for earthquakes in Greece using empirical relations.

3.2 Law of Seismology

The statistical description of various phenomena such as the random seismicity distribution over time, or the fact that smaller earthquakes occur more frequently than large ones, are fundamental concepts for estimating seismic hazards. Seismologists that observe those phenomena and try to describe them, establish different empirical relations that are frequently used nowadays.

3.2.1 Gutenberg-Richter Law

In 1956, Charles Francis Richter and Beno Gutenberg were measuring the magnitudes of earthquakes when they noticed that smaller earthquakes were more frequent than large ones. They were the first to notice the linear relation between the magnitude of an earthquake and the frequency that is triggered. Later that year, they published the relationship between earthquake magnitude and frequency, widely known as the Gutenberg and Richter Law, with publication title "Magnitude and Energy of Earthquakes", 1956 [13].

In any region on the Earth, the logarithm of the total number of earthquakes greater than any magnitude, is proportional to the magnitude. That observation conducts the empirical relation between magnitudes and the frequency of earthquake occurrences [20]. The Gutenberg and Richter Law, also known as Gutenberg-Richter Law or G-R Law, satisfy the following formula:

$$\log N = a - bM, \quad (3.9)$$

where N is the cumulative number of earthquakes with magnitude greater than the minimum magnitude of completeness (M_c), and a and b are constants. Constant a is a measure of the activity level of seismicity and b , which is also known as b-value, is the slope of the frequency magnitude distribution, which is typically close to one [66].

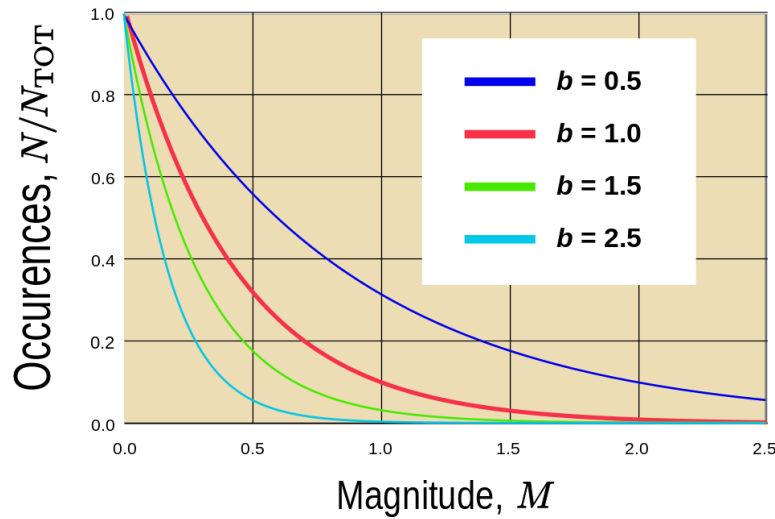


FIGURE 3.4: Plots of Gutenberg Richter law that show the impact of different b-values. Retrieved from [20].

The G-R magnitude distribution is possibly the most widely used statistical relationship in seismology. Its slope, b or b-value, characterizes the ratio of small to large magnitudes. In Fig. 3.4 is illustrated the impact of different b-values following the G-R law. Gutenberg and Richter were the first to estimate these constants known as seismicity parameters [20]. The parameters exhibit significant variations from region to region as they depend on the level of seismicity, the period of observation, the length of the considered area, and the size of the earthquakes. The b-value usually varies between 0.5 and 1.5, but during earthquake swarms, it can reach values as high as 2.5 [5].

On the other hand, some scientist proposed that the b-value for tectonic earthquakes does not differ significantly from 1.0. This opinion was derived from the observation that the distribution of the seismic moment, whose logarithm is proportional to the magnitude, is very stable in space and time [32]. Either way, this empirical relation is a powerful tool for describing and predicting earthquakes, and it is still widely used in seismology studies.

3.2.2 Omori-Utsu Law

In the late nineteenth century, the Japanese seismologist Fusakichi Omori, a devoted student of John Milne, discovered the first law of earthquake physics. On 28 October 1891, an earthquake with the magnitude 8 M_w took place in Japan. Milne's seismographs registered numerous aftershocks. Their analysis allowed Omori to formulate a law in 1894 that bears his name. It is worth mentioning that he was only 26 at that time. The Omori law states that after a strong earthquake, the frequency of aftershocks, decays with time, on average, according to the hyperbolic law which states that the rate of aftershocks decreases hyperbolically with time [58].

In seismology, when analyzing aftershock sequence it is common to replace Omori's Law (3.10) with the modified version proposed by Utsu. It is defined as:

$$n(t) = \frac{k}{(c + t)^p} \quad (3.11)$$

where p is a third constant which modifies the decay rate and typically falls near one in most cases.

This modified version of Omori's law, proposed by Utsu is commonly referred as the O-U law, or modified Omori formula. The power law exponent p , varies from location to location and from case to case, but usually has values near 1 [78].

From a physical point of view, such spatiotemporal clustering of earthquakes indicates that a large earthquake somehow triggered the following ones, which are called aftershocks or aftershock sequence. It is proven that earthquakes, independent of their sizes, can trigger other earthquakes and there is no physical distinction in the relaxation mechanism between aftershocks and other earthquakes. This implies a significant challenge if one wants to verify the Omori–Utsu law and estimate its parameters, since one must first determine which earthquakes are connected, either directly or indirectly, in order to identify aftershock sequences. Estimating the parameters in the Omori–Utsu law is especially important since the time delay before the onset of the power law aftershock decay rate (the c value) is thought to give direct insight into the state of the underlying stress field in the brittle seismogenic layer [51].

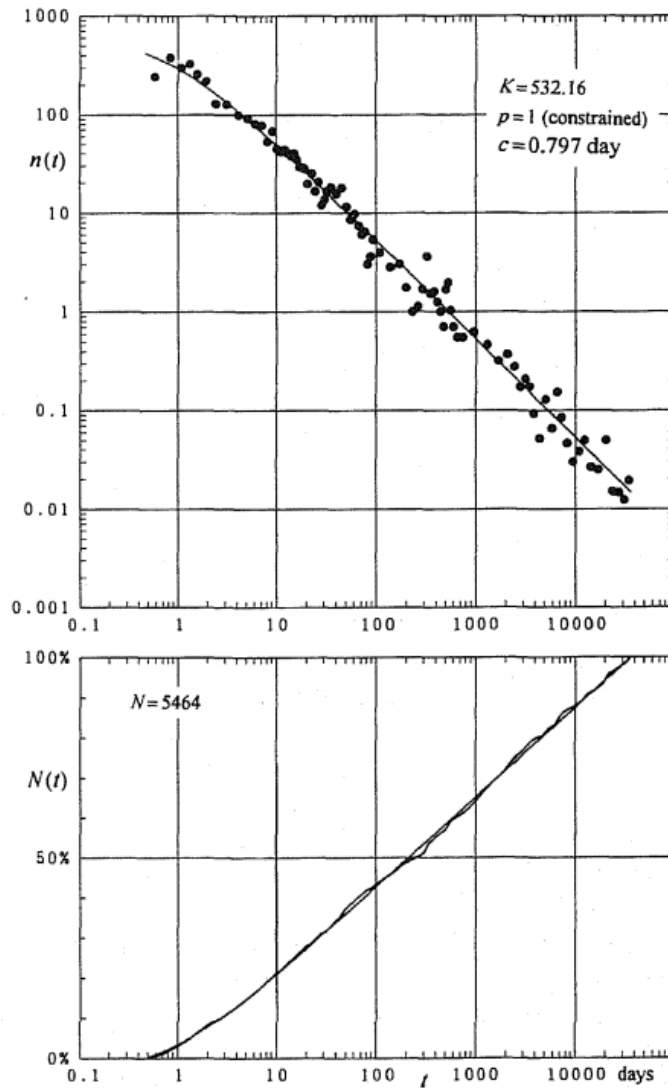


FIGURE 3.6: The top figure shows the decay of the occurrence rate of recorded shocks at Gifu (Japan), using Omori's data from October 28, 1891 (0.474 days after the main shock) until December 31, 1899. The bottom figure is a graph of the cumulative number of felt shocks using the same sets of data. The curves at the top and bottom figures represent the Omori formula and its integrated form fitted to the data from the reported period [58].

According to Eq. (3.10) and (3.11), the rate of aftershocks decreases quickly with time. The rate of aftershocks is proportional to the inverse of time. That means that the main earthquake and this relation can be used to predict the probability of future aftershock occurrence. Whatever the probability of an aftershock is on the first day and assuming that p is equal to 1, the second day will have 1/2 the probability of the first day and the tenth day will have approximately 1/10 the probability of the first day. These patterns characterize only the statistical behavior of aftershocks.

The actual times, locations, and numbers of the aftershocks are stochastic while tending to follow these patterns. Because of the law's empirical nature, values of the parameters are obtained by fitting to data after a main shock has occurred, and they imply no specific physical mechanism in any given case. In addition to the empirical Omori formula, a theoretical one has been also obtained, as the solution of a differential equation describing the evolution of the aftershock activity, where the interpretation of the evolution equation is based on the idea of deactivation of the faults in the vicinity of the main shock of the earthquake [71]. More recently, [67] a published study proposed a double power law model that shows the number density decay after an intense earthquake, by applying a fractional solution of the reactive equation.

3.2.3 The ETAS Model

The initials standing for Epidemic Type Aftershock Sequence, ETAS model, is the most popular stochastic model used to describe earthquake occurrence, forecast earthquakes, and detect fluid/magma signals or induced seismicity.

The temporal ETAS model was suggested by Ogata (1988) [57] with the conditional intensity function of:

$$\lambda(t) = \mu + K_0 \sum \frac{\exp[a(m - m_0)]}{(t - t_i + c)^p}, \quad (3.12)$$

where μ (shocks per unit time) represents the rate of background seismicity, the summation is taken over aftershocks occurring before time t , and m_0 represents the cut-off magnitude of the fitted data. In the above equation, the coefficient α (magnitude⁻¹) is a measure of the efficiency of a shock in generating aftershock activity relative to its magnitude, k_0 represents the productivity of an event of threshold magnitude m_0 , and c (unit of time) and p are the parameters in the Omori-Utsu law for describing the decay of the aftershock sequence.

According to some studies [21], the published algorithms have never been rigorously tested, leading to the conclusion that the ETAS model estimation might result ambiguous values. However, other scientists [86] have stated that the most critical point about ETAS is not what the model can describe, but the phenomena that the model cannot describe. One of the main outcomes of model building is determining aspects of the observed process that the model cannot describe. Even though spatiotemporal models are more

challenging to implement and apply to earthquake data, they are much more robust in analyzing seismicity than their simple temporal-only counterparts.

3.2.4 Bath Law

Apart from the Omori–Utsu and the G-R law, a third empirical scaling law for aftershocks sequences was proposed by Bath in 1966 [8].

Bath’s law states that the average magnitude difference between a main shock and its largest aftershock is ≈ 1.2 , independent of the main shock magnitude [8]:

$$\Delta m = (m_M - m_A) \quad (3.13)$$

with m_M the magnitude of the mainshock, m_A the magnitude of the largest detected aftershock, and Δm approximately a constant typically taken 1.2. Many studies have validated Bath’s law, with however large fluctuations of a difference (Δm) between 0 and 3 from one sequence to another one.

In our analysis, we have tested the Bath Law and between the four largest earthquakes of the aftershock sequence we result with an average difference equal to $1.327 M_L$. The difference between the main shock and its largest aftershock was found $\Delta m = 1.1 M_L$.

This empirical law plays a fundamental role in some stochastic aftershock models, such as the branching aftershock sequence (BASS) model [50], but not in others like the epidemic-type-aftershock sequence (ETAS) model (see section 3.2.3). According to a study [26], the origin of Bath’s law is to be found in the selection procedure used to define mainshocks and aftershocks rather than in any difference in the mechanisms controlling the magnitude of the mainshock and of the aftershocks. In addition, this law is often interpreted as evidence that mainshocks are physically different from other earthquakes and have a different magnitude distribution.

However, from a societal viewpoint, Bath’s law’s importance is found in the fact that it predicts the expected size of the potentially most destructive aftershock that follows the mainshock.

Chapter 4

Statistical Analysis of Earthquake Magnitude

After clarifying to a great extent the concept of magnitude and its different variations or forms in section 3.1, we examined the existing empirical relations and created a new relation between the local and the moment magnitude. The local magnitude (M_L) was derived from the catalog, while the moment magnitude (M_w) and the seismic moment (M_o), which are unknown, were estimated in this Chapter. To decide upon the most suitable regression analysis model, we must first observe how the seismic events are distributed in time.

For the following calculations, the seismic data sequence with magnitudes $M_L \geq 1$ for the time period from 1/6/2016 to 31/5/2018, including the main shock, was used. The cumulative number of earthquakes in the region of Zakynthos during those three years is illustrated in Fig. 4.1 (created in R environment). Right after the main shock of 6.6 M_L that stroke Zakynthos in October 25th, 2018, a sharp increase in the number of seismic events followed. This increase means that this strong earthquake of 6.6 M_L , was able to trigger many smaller earthquakes in this broad area of Zakynthos, creating an aftershock sequence. According to Mouslopoulou *et al.* [49], the majority of those aftershocks mark the activation of other faults. This phenomenon is investigated by many scientists [78, 20, 60], and many empirical laws and relations have derived from it.

For the particular dataset, the aftershock period is seven months, where the total number of aftershocks recorded equals to 9666. Thus, approximately 82% of the total earthquakes studied in this analysis refer to aftershock events. Moreover, it is noteworthy that the aftershocks (82%) occurred during the last 20% percent of the total investigation period (3 years). The complementary 18% describes the seismic events before the main shock, distributed over 80% of the time (2 years and five months).

As mentioned before, the most common measure to characterize the size of an earthquake is the local magnitude scale, M_L . Because of the numerous combinations of wave types and recording instruments, any earthquake can have several magnitudes assigned to it. Although local magnitude may saturate for large (> 6.5) earthquakes (see section 3.1.3), it is expected not to affect events of lower magnitude. Because the majority of the seismic events

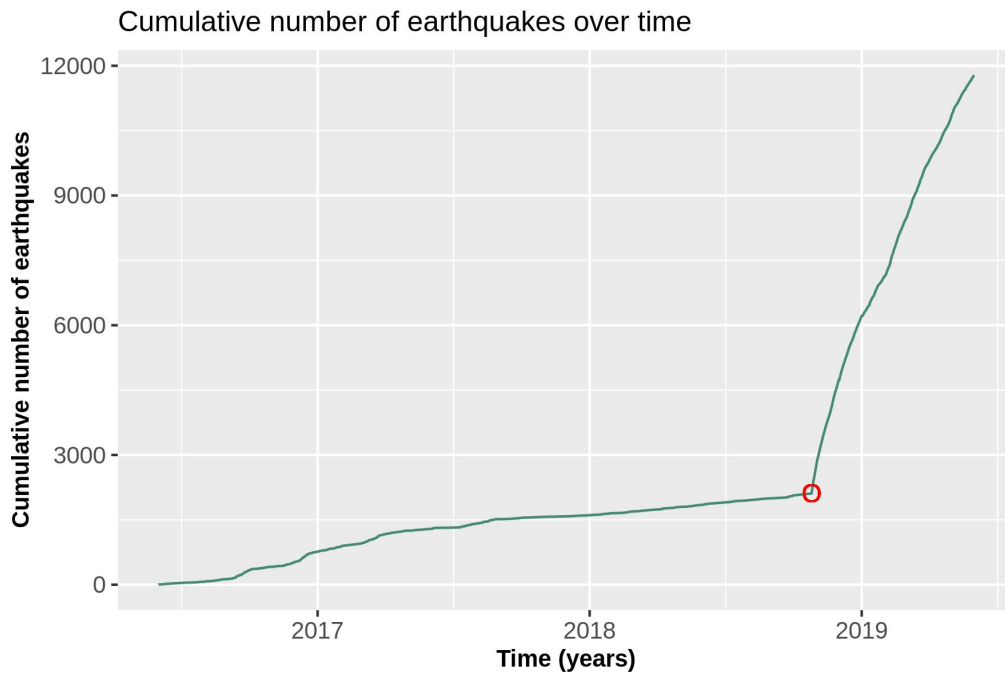


FIGURE 4.1: Plot of the cumulative number of earthquakes with magnitude greater and equal to 1.0 M_L , from 2016 to 2019. The bluish-green line corresponds to the earthquakes in Zakyntos, while the red circle represents the main event.

for this study correspond to magnitude smaller than 6.5, we can characterize them as reliable. The fact that the calculation of local magnitude is computationally inexpensive established it as an indispensable part of routine processing in seismological observatories. However, since the magnitude scale is mainly empirical, there are many problems regarding the association of the fault parameters with the physical model.

To overcome the aforementioned shortcomings, it is urgent to establish more relationships between the different magnitude scales or find more reliable ways to describe the size of an earthquake. Moment magnitude is the most common scale method used to calculate the relative size of earthquakes (especially for the large ones) because it avoids the problem of magnitude saturation, which lies in measurements of the earthquake's total energy.

4.1 Empirical Relation Between Local and Moment Magnitudes

For the study area, during 2016-2019, 11778 events were recorded in terms of the local magnitude scale, while only 14 of them were also calculated in moment magnitude scale (M_w) and registered in the NOA earthquake catalogs. That amount of earthquakes measured in M_w is insufficient, making it nearly impossible for any statistical analysis. Computing complexity may be

one reason for the shortage of moment magnitude data, while the strength may be another one since strong events are required for the calculation.

Considering the small amount of linked data (14), backdated seismic data from 2009 to 2019 (10 years) were acquired, corresponding to the same domain as the case study. Hence, the statistical analysis of the relation between the magnitude scales became possible. The additional data available from the earthquake catalog of the Institute of Geodynamics of the National Observatory of Athens [53] for the backdated seven years (2009-2015) were 41, summing up to 55 linked data for the entire ten year period (2009-2019). The data listed in Table 4.1 is used to establish the mathematical relationships coupling local M_L and moment M_w magnitude.

Moreover, Table 4.1 has information on other parameters than local and moment magnitude. The first four columns accommodate information about the origin date (GMT), the latitude, the longitude, and the depth (km). The local magnitude is presented in the fifth column and has values ranging between 2.7 and 6.6 M_L , while the moment magnitude shown in the sixth column varies from 3.4 to 6.7 M_w .

TABLE 4.1: Dates and coordinates for the 55 earthquake occurrences (2009–2019) used to establish the relation between local and moment magnitude scales.

Date (Y-M-D)	Latitude(°)	Longitude(°)	Depth (km)	M_L	M_w
2018-10-30	37.45	20.45	5.5	5.5	5.8
2018-10-27	37.47	20.64	5.1	4.6	4.4
2018-10-26	37.42	20.59	6.7	4.5	4.4
2018-10-26	37.37	20.53	7.3	4.6	5.1
2018-10-26	37.47	20.52	10.0	4.2	4.5
2018-10-26	37.36	20.51	3.1	4.8	5.1
2018-10-25	37.34	20.51	9.9	6.6	6.7
2018-10-25	37.35	20.55	5.0	4.9	4.8
2018-10-17	37.33	20.56	4.1	4.2	4.1
2018-02-21	37.79	20.34	17.7	4.8	4.7
2017-09-28	37.53	20.89	12.8	4.1	4.1
2017-06-19	37.99	21.20	9.7	4	4.1
2017-02-28	37.90	20.15	7.0	4.1	4.1
2016-10-03	37.76	21.19	28.7	3.9	4.5
2016-03-29	37.34	20.06	12.9	5.2	5.2
2015-12-13	37.81	21.16	27.6	3.9	3.9
2015-12-12	37.83	21.16	28.9	4.6	4.5
2015-07-06	37.34	20.91	12.1	3.9	3.9
2015-07-06	37.49	20.34	10.8	4.1	4
2014-02-06	37.81	21.17	10.7	4.1	4.2
2014-01-18	37.85	21.03	25.1	3.7	3.6
2014-01-11	37.84	21.01	7.4	4.7	4.8
2013-09-09	38.03	20.77	21.9	4.3	4.4
2013-07-28	37.95	20.98	17.9	3.9	4

2013-02-17	37.16	20.52	14.6	5	4.9
2012-11-10	37.89	20.90	12.6	3.9	4
2012-08-11	37.68	20.84	20.7	3.9	4.2
2012-06-05	37.34	20.45	22.4	3.9	4.2
2012-05-03	37.79	21.05	21.0	3.7	4
2012-02-14	37.69	20.77	12.8	4.3	4.3
2011-12-05	37.85	20.10	5.5	3.6	3.7
2011-10-25	37.96	20.83	14.5	3.9	4
2011-08-14	37.33	20.25	13.1	3.8	3.8
2011-08-06	37.30	20.13	17.7	3.8	4.1
2011-06-24	37.56	20.95	15.4	4.2	4.5
2011-06-04	37.94	21.09	14.4	4	4
2011-05-26	37.93	21.16	16.8	4.5	4.6
2011-05-26	37.94	21.14	17.4	3.8	3.6
2011-05-26	37.93	21.14	15.7	2.7	3.6
2011-05-25	37.93	21.12	13.4	4.9	4.8
2011-02-04	38.05	21.23	16.8	3.6	3.6
2011-01-31	37.37	20.49	22.0	3.4	3.9
2011-01-17	37.82	21.07	15.0	3.9	4.2
2010-12-18	37.28	20.22	24.0	4.7	4.6
2010-11-04	37.30	20.18	15.0	3.8	3.9
2010-10-08	38.03	21.02	15.0	3.9	3.8
2010-08-15	37.14	20.81	17.0	4.4	4.5
2010-06-20	37.40	20.28	18.0	3.8	4.1
2010-05-22	37.40	20.27	18.0	3.7	3.9
2010-05-03	37.46	20.40	16.0	4	3.4
2010-04-20	37.47	20.52	19.0	4.2	4
2010-03-19	37.96	20.96	13.0	4	4.1
2010-01-28	37.42	20.79	18.0	3.7	3.7
2010-01-25	37.74	20.88	16.0	3.7	3.7
2010-01-21	37.15	20.73	10.0	3.7	3.6

Detailed studies on different least-squares linear regression techniques and other regression techniques for magnitude scales are carried out by many scientists, to establish relationships between different magnitude scales. For example, the standard least-squares, minimizes the square of the vertical offsets to the best fit line, or the inverted standard least-squares, which minimizes the square of the horizontal offsets, while the orthogonal regression, minimizes the square of the perpendicular offsets to the best fit line. Methodologies such as the above have been widely utilized for the comparison of the different magnitude estimates. While the most simple and commonly applied method for establishing a linear relationship between two magnitude scales is the Linear least squares fitting, Castellaro [9] support that orthogonal regression is a more appropriate technique to deal with least-squares magnitude scales in which dependent and independent variables are both affected by uncertainty.

In this study, a generalization of ordinary least squares (OLS or generalized least squares GLS), as well as the weighted least squares (WLS) linear regression methodologies, were applied. As explained in section 2.17 in WLS the errors covariance matrix is allowed to be different from the identity matrix. With the correct weight, this procedure minimizes the sum of weighted squared residuals to produce residuals with a constant variance. The weight adopted for this study is the square root of each value of moment magnitude. We chose the square root because we wanted to emphasize the larger seismic events, measured in M_w scale, as they tend to be the most reliable measures [22]. In addition, large earthquakes recorded in local magnitude scale tend to be underestimated due to saturation. The regression outcome, which describes those 55 seismic events (2009-2019), results in the following equation:

$$M_w = 0.924 \cdot M_L + 0.401, \quad (4.1)$$

for earthquakes inside the local magnitude range $2.7 \leq M_L \leq 6.6$.

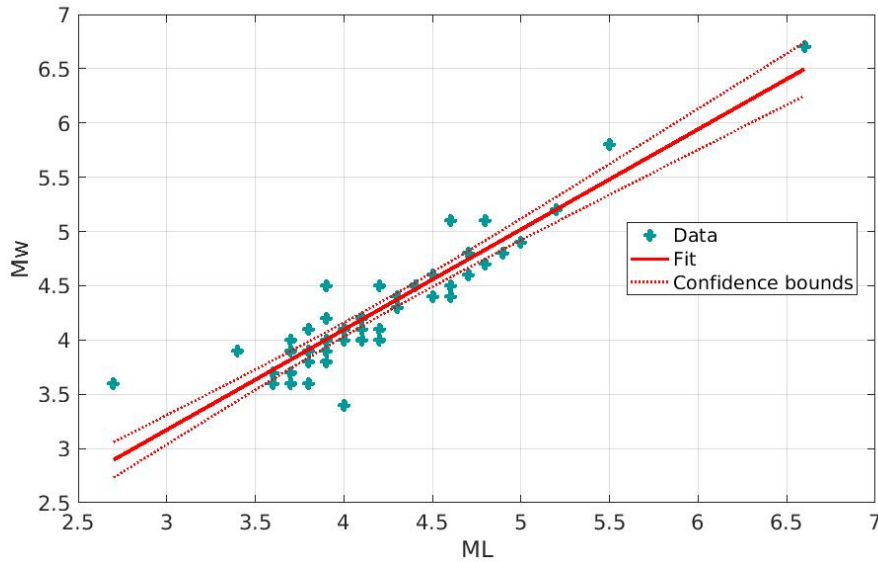


FIGURE 4.2: Scatter plot of the relationship between local magnitude and moment magnitude values obtained for the period from 2009 to 2019. The moment magnitude was obtained by means of weighted linear regression according to the Eq. (4.1). The blueish-green symbols (crosses) correspond to the local and moment magnitude values; the solid red line denotes the optimal fit, and the red dashed lines denote the confidence bounds.

The validation measures presented in Table 4.2, combined with Fig. 4.2, create a complete “image” of the WLS model’s performance. It is apparent

TABLE 4.2: Cross validation performance measures calculated for the WLS estimations ($y = \alpha \cdot x + \beta$) for 55 seismic events.

Values	Estimate	Standard Error
β	0.401	0.212
α	0.924	0.050

that the two magnitude scales are convey a strong dependence since they both follow along the solid red line. The coefficient of determination R^2 is estimated as 0.866 and the p-value of this model is found $8.13e^{-25}$. Very small p-values, as in this case, indicates high significance of the statistical results. The confidence levels (95%) appear narrower for magnitudes values from 3.5 to 5, as in this range, we have the majority of the seismic events. Extreme values seem to deviate from the suggested model, indicating that the further we go from the median magnitude value, the higher the uncertainty. The standard error for the scale parameter α of the linear model equals 0.212, while the offset parameter β is 0.050, which results in the equation:

$$M_w = (0.92 \pm 0.05) \cdot M_L + (0.40 \pm 0.21). \quad (4.2)$$

Many seismologists have also proposed relationships between local and moment magnitude scales. The most common and widely used equation follows the simple relation stating that moment magnitude is equal to the local magnitude increased by 0.5 magnitude [39]. It is routinely applied to the seismic events in Greece in cases where moment magnitude is not available. It is expressed as:

$$M_w = M_L + 0.5, \quad (4.3)$$

where M_w refers to the moment magnitude and M_L refers to the local magnitude.

Additionally, Papazachos [60] applied regression analysis to 245 seismic events, concerning the period from 1969 to 1987 (18 years), and proposed the following equation for Greece

$$M_w = (0.97 \pm 0.02) \cdot M_L + (0.58 \pm 0.09), \quad (4.4)$$

for earthquakes inside the local magnitude range $3.0 \leq M_L \leq 6.0$.

Both aforementioned Eqs. (4.3) and (4.4) result in higher M_w values opposed to results based on Eq. (4.1) proposed in this study. Therefore, to assess the performance of the proposed equation, certain statistical measures need to be evaluated. The error measures are presented in Table 4.3.

Where mean error (ME) also know as bias was calculated using Eq. (2.11), mean absolute error (MAE) was calculated using Eq. (2.12) and mean absolute relative error (MARE) (INF if z contains zeros) was calculated using Eq. (2.13). The root mean square error refers as RMSE calculated by

TABLE 4.3: Error measures of the estimated M_w based on Eq. (4.1) versus the recorded M_w .

ME	MAE	MARE	RMSE	RMSRE	R	R_S	ErrMin	ErrMax
0.083	0.171	0.044	0.246	0.070	0.921	0.876	-0.600	0.900

Eq. (2.14) while the root mean square relative error refer as (RMSRE). The Pearson's linear correlation coefficient (R), calculated by Eq. (2.2), equals 0.92, which translated to a high linear correlation. The Spearman (rank) correlation coefficient (R_S), estimated by Eq. (2.16), is equal to 0.88, a high value indicating a strong monotonic correlation. Furthermore, MAE and RMSE yielded low values, indicating a good model. Finally, both differences between minimum prediction and minimum sample value (ErrMin) and between maximum prediction and maximum sample value (ErrMax) result in low values proving the high performance of the model.

4.1.1 Estimates of Moment Magnitude

After creating the empirical Eq. (4.1) to connect M_L with M_w and validate its reliability, we applied it to the initial 11778 seismic events of our study, which were registered in local magnitude M_L , and calculated the corresponding moment magnitude M_w .

This empirical relationship was created by using earthquakes with magnitude higher than 2.7 M_L ; consequently, it can describe sequences above that limit more accurately. However, in this analysis, the formula was applied to the complete dataset, including events lower than the 2.7 limit, starting with 1.0 M_L magnitude. Further research is needed to determine such relationships for smaller magnitudes.

In addition Eq. (4.1), might underestimate the moment magnitudes, which will be referred to as converted moment magnitudes from now on. For example the 6.6 M_L main shock, according to NOA was estimated [53] at 6.7 M_w , while with Eq. (4.2) developed herein, it was estimated ranging between 6.0 to 7.0 M_w . If we apply other proposed relationships such as Eq. (4.3) or Eq. (4.4), we will result in greater converted moment magnitude values. Respectively, the main shock is estimated at 7.1 M_w according to Eq. (4.3) and between (6.76 - 7.20) M_w according to Eq. (4.4). Nonetheless, the proposed Eq. (4.1) found to be the most appropriate for those specific seismic events in this particular 20000 km^2 area of Zakynthos and will be used to illustrate the distribution of converted moment magnitude over time fig. 4.3.

In Fig 4.3 the main event of 6.5 converted moment magnitude, is marked with a red circle, while the seismic events are illustrated with the bluish-green color. The more opaque the colour the denser earthquakes were recorded. By observing this figure, we notice a relative decrease in the number of earthquakes from August 2017 until right before the main shock. As many seismologists propose, it is common to observe an inactive period preceding

strong earthquakes. It is called seismic quiescence and can be used to prelude a strong earthquake [17]. After this strong earthquake of 6.5 converted M_w , the frequency of the earthquake aftershocks has increased. This is expected, as large earthquakes trigger strong aftershock sequences. It is also apparent since the aftershocks for the case study are 9666 (80% of the total events) for a significantly shorter time period (20% of the total time), as opposed to the 2112 earthquakes before the main shock.

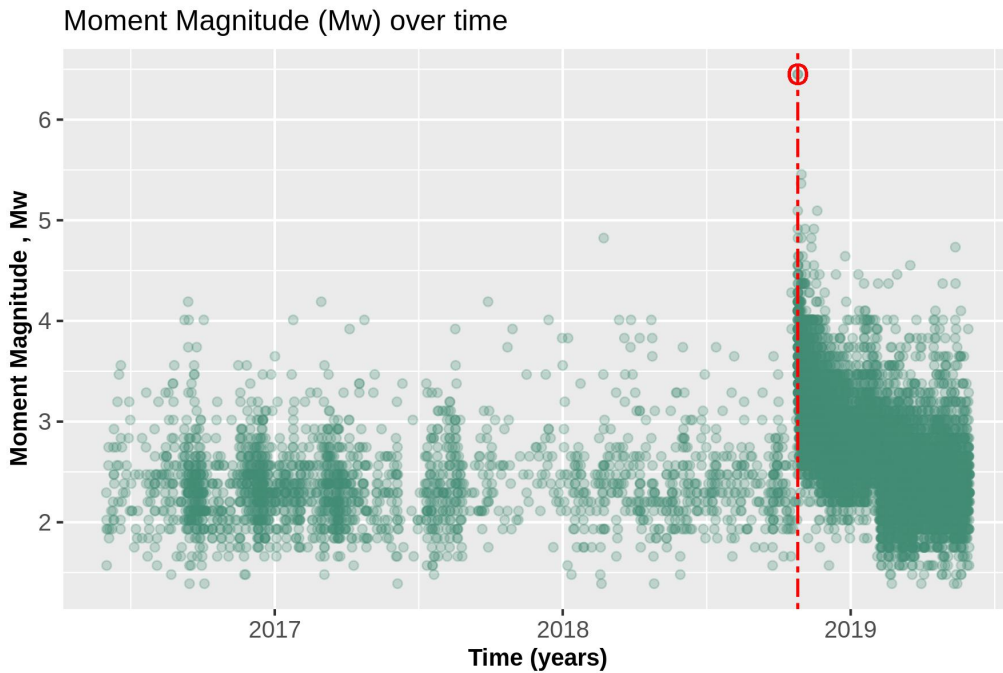


FIGURE 4.3: Plot of the converted moment magnitude, M_w during a period of 3 years from 2016 to 2019. The conversion was carried out according to Eq. (4.1). The bluish-green circles represent the 11778 earthquake events and the big red circle corresponds to the main earthquake of Zakynthos, in 25/10/2018. The red dashed line divide the earthquakes to the before the main shock sequence and to the aftershock sequence.

4.1.2 Estimates of Seismic Moment

Moment magnitude uniquely speaks to the physics of the fracture though the seismic moment (see section 3.1.2), which need to be estimated in the following analysis. The converted moment magnitude M_w is used in a formula established by Papazachos, to estimate the unavailable seismic moment values. It is common to calculate the moment magnitude using the seismic moment and not the opposite, as the seismic moment is a quantity, generated by a slipping fault, which is used to measure the amount of energy released by an earthquake. However, by reversing the procedure, we can extract the seismic moment quantity. In this section, the seismic moment

M_o , also unavailable from the catalog, was calculated from the converted M_w . Essentially, M_o is a measure of the energy that brings forth permanent displacement or distortion of the earth's crust. It is necessary to estimate its value as the potential destructiveness of an earthquake depends, among other factors, on how much of the energy in total is converted into seismic waves [6].

To estimate the seismic moment, we utilize moment magnitude (M_w) and Eq. (4.5) developed by Papazachos [61] and presented in the book "The Earthquakes of Greece". In this analysis, Papazachos studied 169 seismic events in Greece, where he applied linear regression analysis (assuming a slope equal to 3/2 [34]) and concluded to the following regression model:

$$\log M_o = \frac{3}{2}M_w + 15.99. \quad (4.5)$$

The equation proposed by Papazachos is inspired by Hiroo's Kanamori equation and consist of a modification of his original one. Kanamori's proposed equation [33] is widely used in seismology and is described as:

$$\log M_o = \frac{3}{2}M_w + 10.7, \quad (4.6)$$

The Eq. (4.5) was applied in this analysis as it refers to the Greece region. Moreover, it is more representative since it describes shallow earthquakes such as the Zakynthos events. Using a model derived from the same seismotectonic environment and described by the same seismic characteristics (shallow depth) as those observed in Zakynthos, will result in more accurate values.

By applying the selected empirical equation to the converted moment magnitudes, we result in the seismic moment values, measured in dyn·cm. Following, we illustrate in Fig. 4.4 the cumulative seismic moment over time.

The calculated cumulative seismic moment in dyn·cm is displayed, from 2016 to 2019. The thicker the green color appears, the more frequent the earthquakes are. The red circle represents the main earthquake in Zakynthos, on October 25th, 2018. In the period before the mainshock, we notice an apparent lower cumulative energy release compared to that after the mainshock. One ambiguous phase and three clear temporal phases are determined, each one refer to a pattern of tectonic seismic series. The first phase (the ambiguous one) starts in June 2016 and finishes near November 2016, and includes about 420 earthquakes. In this phase, the reduced release of energy may indicate a change in the recording quality or even describe the insufficiency of the seismic station's recording means. The second phase spans from November, 2016, to 15th of February, 2018 and represent a stable energy release. In the third phase, from 16th of February, 2018 until October 25th, 2018, there is a profound increase in energy release. This might be the result of increased seismic activity. On the other hand, it might also indicate the installment of new seismic equipment. The most probable scenario is that the energy release spike comes from the third stronger earthquake recorded on the dataset before the main event, which happened on February

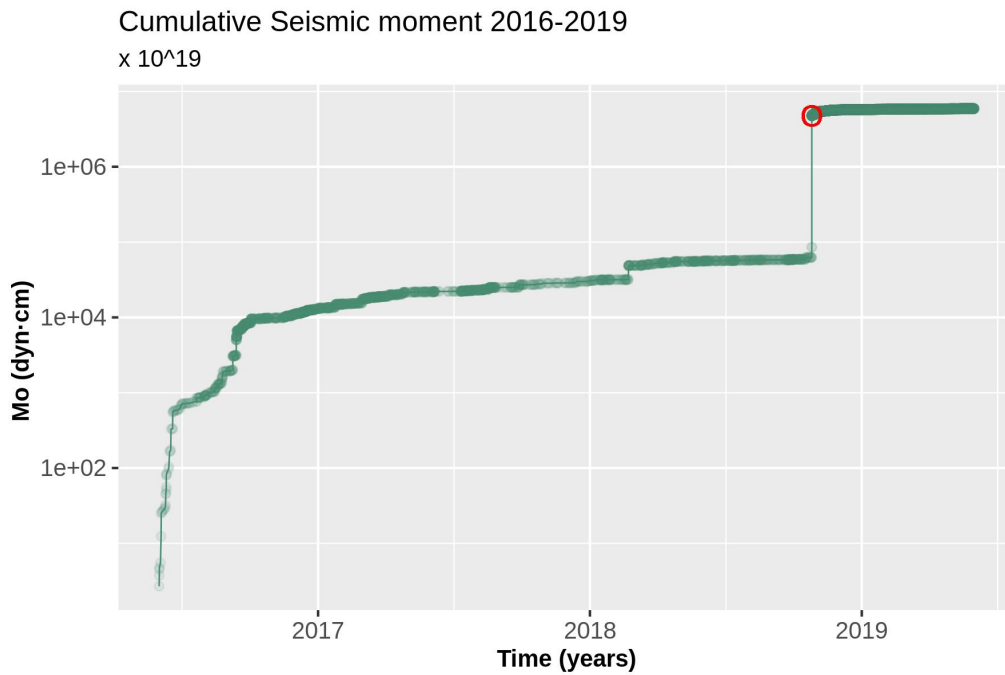


FIGURE 4.4: Plot of cumulative seismic moment release, measured in dyn·cm and calculated from the empirical Eq. (4.5). The bluish-green circles represent the cumulative number of the earthquakes during the period from 2016 to 2019. The red circle stands for the main event.

21st 2018, with 4.8 M_w . Finally, the last phase spans from October 25th, 2018 to May 2019, which includes 9666 events that sum up to almost 82% of the total number of earthquakes. The released energy and the released seismic moment in this fourth phase are by far the strongest, although accumulated over a smaller duration. The strongest earthquake of the entire seismic sequence with magnitude 6.5 M_w was recorded during this fourth phase. The total released seismic moment for the whole sequence equals $5.91 \cdot 10^{25}$ dyn·cm.

Chapter 5

Statistical Analysis of Earthquake Frequency

This chapter aims to investigate the frequency of earthquakes concerning their magnitude scale. We accomplish this by applying the Gutenberg Richter Law (see section 3.2.1) to estimate the b-value both for the earthquakes prior to and after to the main event. The seismic events, used in this section refer to the scale of the converted moment magnitude (M_w). The b-value in the Gutenberg Richter relationship provides vital information for understanding the background seismicity, and seismotectonics, and can be used for seismic hazard analysis. Firstly, it is necessary to estimate the magnitude of completeness M_c to achieve an appropriate b-value. Magnitude of completeness is a crucial parameter as it gives the minimum magnitude above which all earthquakes within our region are reliably recorded. For conciseness, with the term foreshocks, we will describe all the earthquakes before the main event starting from June 1st, 2016 until the main shock on October 25th, 2018. Aftershocks, consist of all the earthquakes from October 25th, 2018 till May 31st, 2019.

5.1 Determination of the Magnitude of Completeness

The magnitude of completeness is defined as the lowest magnitude above which all of the earthquakes in a specific area are detected. This definition assumes that a percentage of earthquakes smaller than M_c are not recorded by the network: (1) because they are too small to be recorded from several stations, (2) because seismic network operators have decided that earthquakes below a specific limit will not be analyzed, or (3) in the case of an aftershock sequence, some earthquakes are too small to detect because they are overlapping with the larger ones. The correct estimate of M_c is crucial, since a value too high leads to under-sampling, by discarding usable data; while a value too low leads to erroneous seismicity parameter values and thus to a biased analysis, due to the data incompleteness.

In seismicity studies, there are several different methods for calculating the magnitude of completeness. Here, we will focus on three different methods based on earthquake lists method (see Section 2.6): (1) the Maximum

curvature method (MAXC), (2) the Goodness-of-fit (GFF), and (3) the Entire magnitude range (EMR) method. For the calculation of the different M_c estimates, we used a Matlab module called Basic Statistical Seismology [74].

The maximum curvature technique (MAXC), which is described in Section 2.6.1, works by finding the point where the non-cumulative distribution has the highest curvature [82].

The goodness of fit (90%, 95%) (GFF), described in Section 2.6.2, compares observed frequency magnitude distribution (FMD) with synthetics on a per bin basis.

The entire magnitude range (EMR), described in Section 2.6.3, uses a model that fits the whole data range by using the power G-R law for the complete part and cumulative normal distribution for the incomplete part of the non-cumulative frequency magnitude distribution (FMD) [56].

The main distinction is whether they are parametric (GFF, EMR) or non-parametric (MAXC). Parametric techniques are based on fitting the frequency magnitude distribution (FMD), while non-parametric techniques are based on the evaluation of changes in the FMD (e.g., possible breaks in the slope). In the present study, there is no consensus about which technique optimally calculates M_c , since as shown in the tables all of them provide similar results. Wiemer and Woessner [83] found that bootstrap uncertainty decreases with increasing sample size, and that both MAXC and EMR approaches result in reasonable values in small data sets.

In an aftershock sequence, some events are too small to be detected within the larger aftershock activity, as the noise is higher [56]. This results in a M_c value higher for the aftershock period (shown in Table 5.2). Temporal changes in M_c originate not only from a large aftershock sequences but also from the evolution of the seismic network (pseudo permanent changes) or are due to swarm activity.

Depending on the method, Tables 5.1, and 5.2 summarize the results on M_c for the foreshocks and aftershocks sequences, respectively. The results are divided into two sections, with and without the use of the bootstrapping method. Bootstrapping methodology uses random sampling methods and it is briefly described in Section 2.4, MAXC refers to the maximum curvature, and GFF and EMR refer to the goodness of fit and the entire magnitude range, respectively.

TABLE 5.1: Estimation of the magnitude of completeness M_c , based on three different methodologies, the MAXC, the GFF, and the EMR, with and without Bootstrapping. For the earthquakes before the main event.

Method	MAXC	GFF	EMR
Bootstrapping	2.1	2.0	2.0
No Bootstrapping	2.2	2.2	2.1

Evident in Tables 5.1, 5.2, the application of the three methodologies yielded similar results. The average difference between those methods for the M_c , both for the foreshock and the aftershock periods, is approximately

TABLE 5.2: Estimation of the magnitude of completeness M_c , based on three different methodologies, the MAXC, the GFF, and the EMR, with and without Bootstrapping. For the earthquakes after the main event.

Method	MAXC	GFF	EMR
Bootstrapping	2.5	2.4	2.4
No Bootstrapping	2.4	2.6	2.5

$\pm 0.1M_w$. Seismologists [84, 81, 56], accept equally the GFF, EMR, and MAXC methodologies, thus every result shown on Tables 5.1, 5.2 can be used for further analysis. In addition, those values are close to the respective M_c values obtained in a recent study by Mouslopoulou *et al.* [49], which refers to the same area in a similar time window. They estimated the M_c prior to the mainshock at 2.0 ± 0.1 , which is close to our estimated 2.1 ± 0.1 . For the aftershock period Mouslopoulou *et al.* [49] found that M_c abruptly increases to 3.5 after the mainshock while it returns to pre-mainshock values close to 2.0 about 120 days after the mainshock. While we reckoned one M_c value for the aftershock sequence equal to $M_c = 2.5 \pm 0.1$. The determination of the initial value for the magnitude of completeness plays an important role in the predicted b-value.

The magnitude of completeness (M_c) in the ZES prior to the mainshock is 2.0 ± 0.1 , it abruptly increases to 3.5 after the mainshock (Fig. 2b) while it returns to pre-mainshock values (2.0) about 120 days after the mainshock (Fig. 2b).

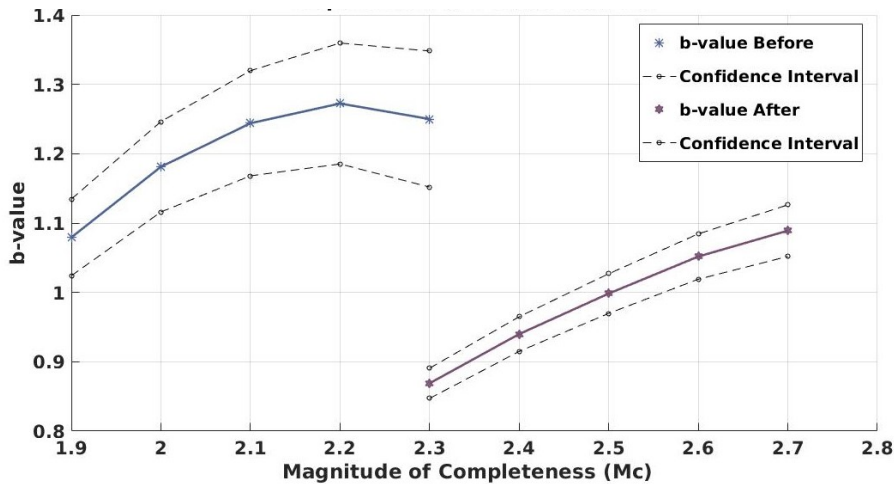


FIGURE 5.1: Plot of the relationship between the b-value and the M_c for all the earthquakes. The solid blue line (on the left) illustrate that relationship for the foreshocks, while the solid purple line (on the right) illustrates the same relationship but for the aftershocks.

In Fig. 5.1, the dependence of b-value against the magnitude of completeness, is illustrated. For the foreshock sequence, the resulting values of M_c vary from 1.9 to 2.3, with the corresponding b-values ranging between

1.08 and 1.25. Although the above methods obtained the optimal M_c values, which vary from 2.0 to 2.2, we estimate and plot a more extensive value range to examine the relationship between the magnitude of completeness against b-value. An M_c equal to 2.0 give a b-value equal to 1.18 and an M_c equal to 2.2 give a b-value equal to 1.27. If we take into account the entire range of the confidence intervals, the b-value for the foreshocks when magnitude of completeness M_c is set to 2, can range between 1.12 and 1.25.

Subsequently, the M_c estimations of 2.4, 2.5 and 2.6, derived from the MAXC, GFF and EMR methods, are illustrated in the same way Fig. 5.1. To demonstrate the dependence of b-value with magnitude of completeness for the aftershock period, we set M_c in the range 2.3 to 2.7. The confidence intervals of b-value for the aftershock sequence are significantly narrower, compared to the foreshock intervals. This can be explained because the seismic events of the foreshock are by far fewer from the aftershock seismic events. Hence, this leads to a more complete data set, allowing the model to estimate the b-value better and display lower fluctuations.

Moreover, the M_c is found consistently higher, $0.4 M_w$, in the aftershock period, probably due to the large aftershock activity in 2018. It is common to expect a temporary increase in the magnitude of completeness values after a big earthquake [32, 25]. Moreover, studies on typical background seismicity periods have shown that M_c changes over time, and more specifically, decreases. That decrease may be attributed to the continuously increasing number of seismographs established and the employment of improved methodologies to the estimation [82].

5.2 Estimation of b-value

After deciding upon the magnitudes of completeness, we proceed in the following analysis. To estimate the parameter b-value from the Gutenberg-Richter Law we used the three different M_c calculated in Section 5.1. The code used was created by Dionisis Hristopoulos in 2011 in the Matlab programming environment [27].

The b-value for any region can be computed using several methods, such as linear regression or maximum likelihood. In this module, the maximum likelihood method was used as it is the most robust and widely accepted method [2]. The maximum likelihood methodology weights all the earthquakes equally in the estimation of the parameter values. On the contrary, the estimates based on the least squares method are biased towards the ends of the distribution. All the data from the seismic catalog greater or equal to each M_c were used. The analysis was performed for two different versions of the same dataset, with or without the mainshock's inclusion.

Despite the simple meaning of b-value—an indicator of the relative proportion of smaller and larger earthquakes in a seismic catalog—the accurate estimation within uncertainty bounds can have significant implications in

seismic hazard studies, faulting and earthquake physics. The b-value is considered to be characteristic for any given region, and many authors support that it decreases slightly before large earthquakes [69, 44, 55].

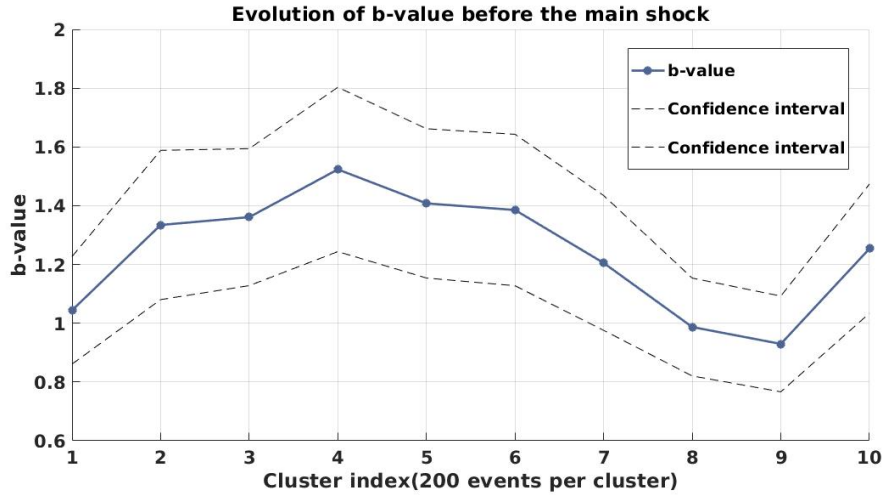


FIGURE 5.2: Evolution of the b-value over time before the main shock. The 6th cluster refers to the period from April 2017 to July 2017, the 7th cluster lasts from August 2017 until December 2017, the 8th cluster last from January 2018 until May 2018 and the 9th cluster starts from June and ends at September 2018.

Figure 5.2 illustrates the b-value of the events from June 2016 to 25 October 2018, divided into 10 clusters. Each cluster includes 200 events except from the last one (10th cluster), which includes the remainder from the seismic catalog, resulting in 113 events. In the 10th cluster the last event considered (the 113th) is the main shock. For every 200 events, one b-value was estimated using the maximum likelihood method. Thus, the b-value for each cluster is represented in chronological order from 2016 to 2018. Essentially, we can see the evolution of the b-value across a two year and five month period. According to Fig. 5.2, from the first until the 7th cluster, b-value ranges mostly between 1.0–1.5. Those values are falling into the expected b-value range for a normal sequence. However, after the 8th cluster, a slight decrease of the b-value is observed, and specifically below 1. This decrease, according to seismologists, might indicate a probable trigger for a large earthquake. The 10th cluster was not taken into account, as it contains the main shock and a smaller sample. A point of interest that could drive further studies is whether the evolution of the b-value and more accurately, its systematic decrease, can be used as a guideline for the prediction of an imminent earthquake.

Tables 5.3 and 5.4 contain the b-values estimated for the foreshock and the aftershock sequence, calculated via the maximum likelihood method — each different magnitude of completeness result in different b-value (Fig. 5.1). The M_c is referring to the magnitude of completeness, b stands for the Gutenberg-Richter exponent.

For further analysis, we selected to use for the foreshock sequence $M_c = 2.0$, and for the aftershock sequence $M_c = 2.5$. We based our decision on the fact that those values were inside the optimal value range computed from the maximum likelihood method (Tables 5.1, 5.2), and simultaneously yielded the closest to one b-values (Tables 5.3, 5.4).

TABLE 5.3: Estimated b-value parameters for the foreshocks using the maximum likelihood method. The M_c is the magnitude of completeness, b stands for the Gutenberg-Richter exponent, hbint, and lbint represents the upper and the lower confidence bound for the G-R exponent, respectively. The symbol b10 stands for the G-R exponent (base 10) and hbint10, and lint10 the corresponding confidence bounds for the G-R exponent (base 10). The bold font distinguishes the M_c and the b-value used for further analysis. Graphical representation shown in Fig. 5.1.

M_c	b	lbint	hbint	b10	lbint10	hbint10
1.9	2.49	2.36	2.61	1.08	1.02	1.14
2.0	2.72	2.57	2.87	1.18	1.11	1.25
2.1	2.86	2.68	3.04	1.24	1.17	1.32
2.2	2.93	2.73	3.13	1.27	1.19	1.36
2.3	2.88	2.65	3.10	1.25	1.15	1.35

TABLE 5.4: Estimated b-value parameters for the aftershocks using the maximum likelihood method. The symbols are described in Table 5.3.

M_c	b	lbint	hbint	b10	lbint10	hbint10
2.3	2.00	1.95	2.05	0.87	0.85	0.89
2.4	2.16	2.11	2.22	0.94	0.95	0.97
2.5	2.30	2.23	2.37	1.00	0.97	1.03
2.6	2.42	2.35	2.50	1.05	1.01	1.09
2.7	2.51	2.42	2.60	1.09	1.05	1.13

On average, b-value is close to 1 for most seismically active regions on Earth, but in some cases varies between 0.5 and 1.5 [81]. This means that for a given frequency of magnitude 4.0 or larger events to occur, there will be 10 times as many magnitude 3.0 or larger earthquakes, and 100 times as many magnitude 2.0 or larger earthquakes. In this study, for all the examined M_c values (5.1), b-value varies between 0.94 and 1.27, falling within the expected range. However, a detailed mapping of b-value often reveals significant deviations (Fig. 5.2). A notable example is the variation of the estimated b-values during earthquake swarms, where b-value can become as

high as 2.5 [5]. On the other hand, high b-values are reported for areas with increased geological complexity, indicating the importance of multi fracture areas [69].

5.2.1 Plots of Estimated b-value for Earthquakes Prior to the Main Event

Our results indicate that the b-value estimates for the earthquakes before the main event are within the expected values. The histogram of probability density function (PDF) for foreshock sequence Fig. 5.3 was created with $M_c = 2.0$, and the b-value estimate corresponds to this magnitude of completeness. According to the data values shown in Fig. 5.3, larger magnitudes seem to deviate more from the theoretical line drawn based on the G-R law with a b-value equal to 1.18. This observation is especially true for earthquakes with magnitude greater than five, which are located outside the confidence bounds, diverging from the Gutenberg Richter model. Particularly, for a magnitude greater than 6.5 we have only one earthquake, the main shock and for a magnitude near 5 only two earthquakes. While from the other hand for a magnitude near 4 we have around 27 events and for a magnitude near 3 around 70 events and continues to increase with a decrease of magnitude. Nevertheless, the data marked with the cyan circle displays the expected behavior in terms of the frequency, presenting a difference by one order of magnitude for the frequency when the magnitude differs by 1 unit (for earthquakes less than $5.5 M_w$).

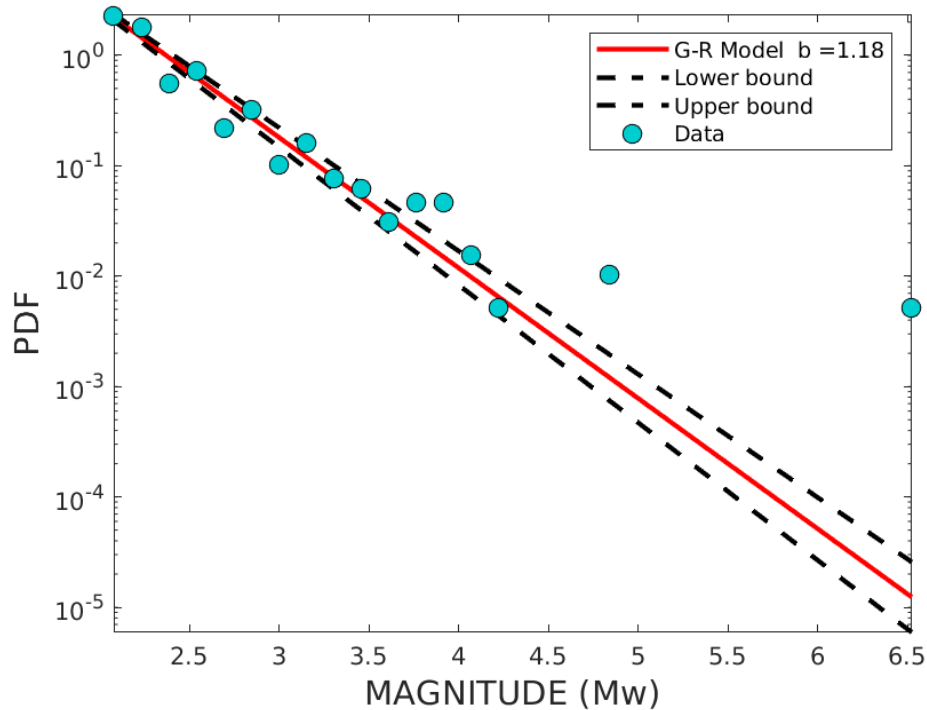


FIGURE 5.3: Histogram of probability density function versus event magnitude for foreshocks, using logarithmic vertical scale.

In the histogram presented in Fig. 5.4 we can observe the number of earthquakes before the main event versus the magnitude. Apparently, most earthquakes have magnitude near 2.0, which is also the estimated minimum magnitude for the foreshocks. From the initial 2112 seismic events refer to the earthquake prior to the main event only 1260 meet the $M_c = 2.0$. They are represented with the cyan columns in the histogram. The orange line fitting the data matches the Gutenberg Richter curve.

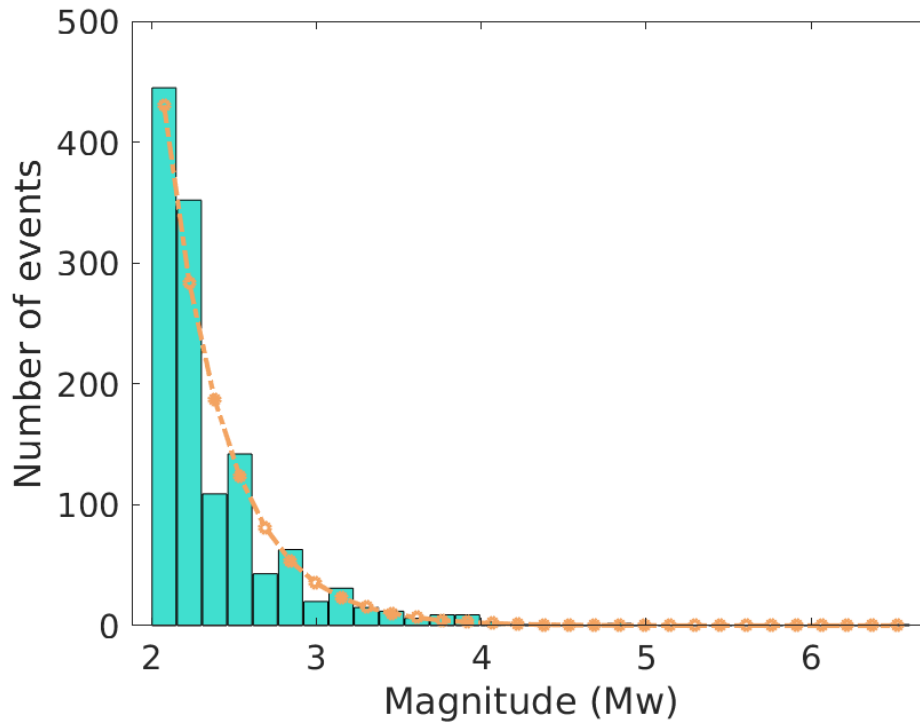


FIGURE 5.4: Histogram of the number of foreshocks per magnitude and fit to the optimal exponential (GR curve).

By removing the main shock from the foreshocks' data set, the estimated b-value for those foreshocks decreases slightly compared to estimates that included the main shock. This decrease in the b-value from 1.18 to 1.15 is shown Fig. 5.5. In this case, the data follow better the G-R distribution, while the histogram of the number of foreshocks without the main event Fig. 5.6 seems to be more evenly distributed.

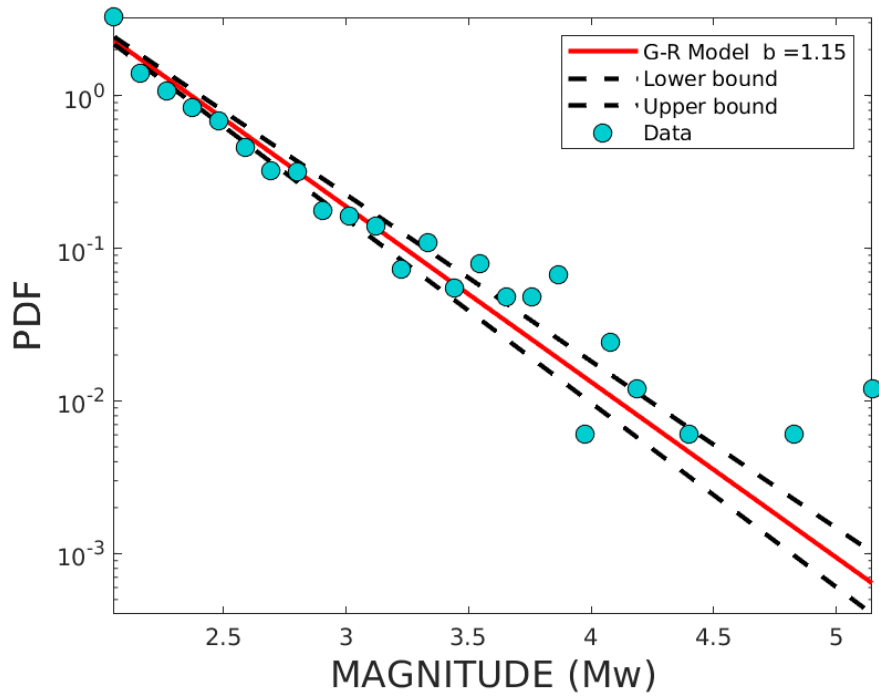


FIGURE 5.5: Histogram of probability density function versus event magnitude for foreshocks, without main event, using logarithmic vertical scale.

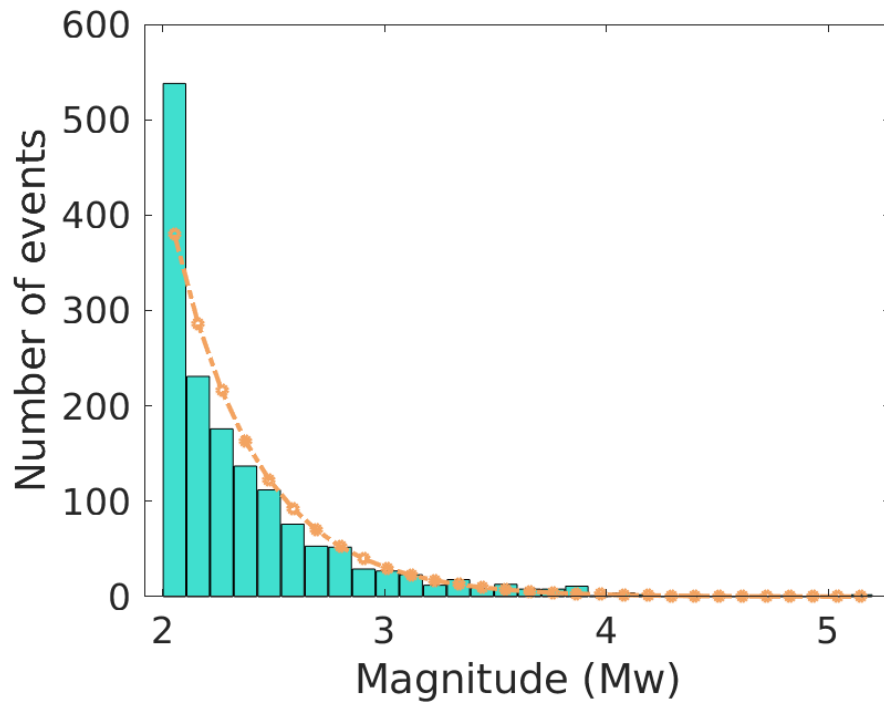


FIGURE 5.6: Histogram of the number of foreshocks without the main shock of $6.6 M_L$ per magnitude and fit to the optimal exponential (GR curve).

5.2.2 Plots of Estimated b-value for Aftershock Sequence

In terms of the aftershock sequence, the M_c used to estimate the b-value equals 2.5. The resulting b-value is 0.998. Figure 5.7 refers to the histogram of PDF versus the magnitude of the aftershocks, including the main shock. Only half of the initial 9666 recorded aftershocks are greater or equal to $M_c = 2.5$. However, in terms of the abundance of the data for processing, having 4700 events is better than the 1260 foreshocks. The adequate amount of data could eventually lead to more reliable results, as shown in Fig. 5.7.

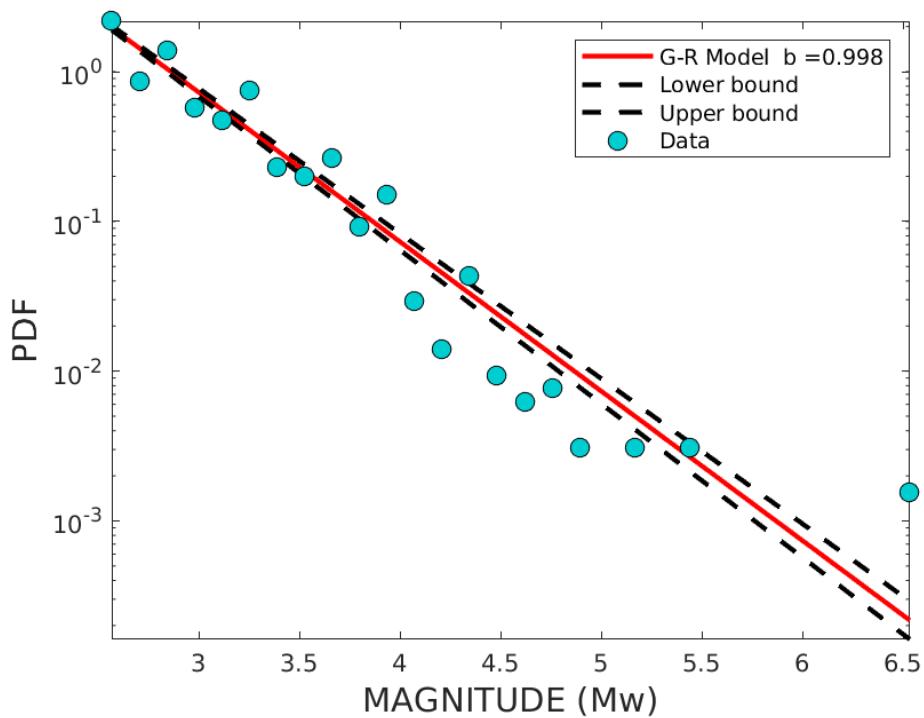


FIGURE 5.7: Histogram of probability density function versus event magnitude for aftershocks, using logarithmic vertical scale.

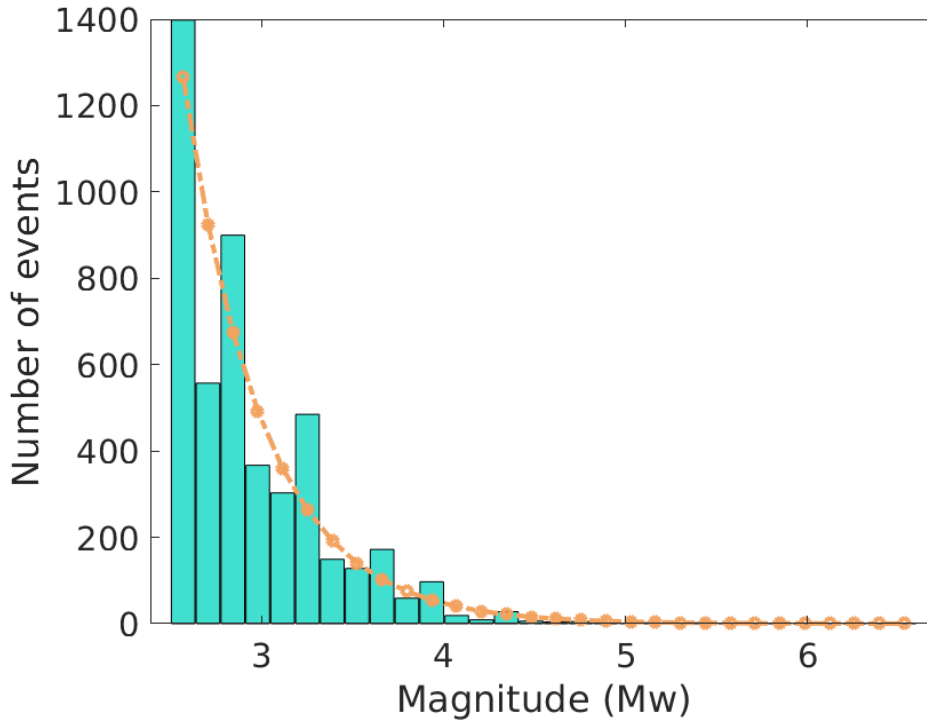


FIGURE 5.8: Histogram of the number of aftershocks per magnitude and fit to the optimal exponential (GR curve).

Using the same parameters, M_c and number of bins, we estimated the b-value, but this time, without the main event. The resulting histogram of PDF 5.9, indicates that the seismic events are more evenly distributed according to G-R Law, in the same way that it was evident in the foreshock set without the main event (Fig. 5.5). Opposed to the foreshock b-value estimation, which decreased by 0.030, the b-value for the aftershocks increased by 0.012 when calculated with or without the main event. In addition, the histogram 5.10 of the number of aftershocks, without the main shock appears smoother.

The b-value for a region reflects the relative proportion of the number of large and small earthquakes in the area and relates to the region's stress condition.

Previous studies concerning Zakynthos have studied the swarm in 2006 and estimated a b-value equal to 1.27 [59]. A b-value slighter higher than our results, since it is usual for b-value to take higher values during earthquake swarms [5].

More recent studies [49] that studied the seismic sequence of 2018; estimated the b-value near and below 1 for the foreshocks and at 1.18 ± 0.12 for the aftershock sequence. Between 2016 and 2017, they characterized that 6-month time-period as swarm-like activity, resulting in higher b-values. We have also estimated those higher b-values in our analysis. In Fig. 5.2, they are represented from the period between September 2016 to April 2017, and correspond to the 3rd, 4th and 5th cluster. While it has been shown by

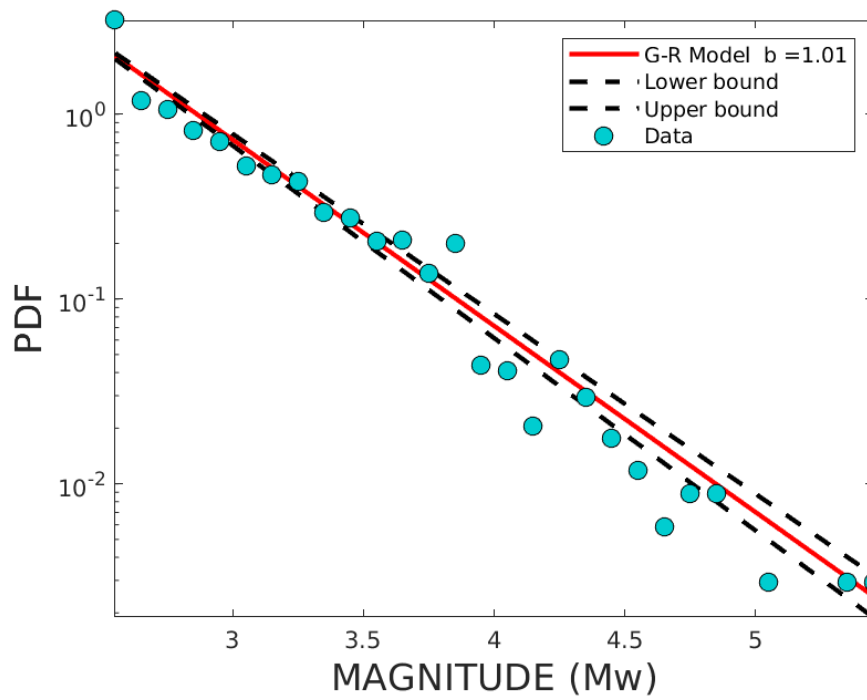


FIGURE 5.9: Histogram of probability density function versus event magnitude for aftershocks, without main event, using logarithmic vertical scale.

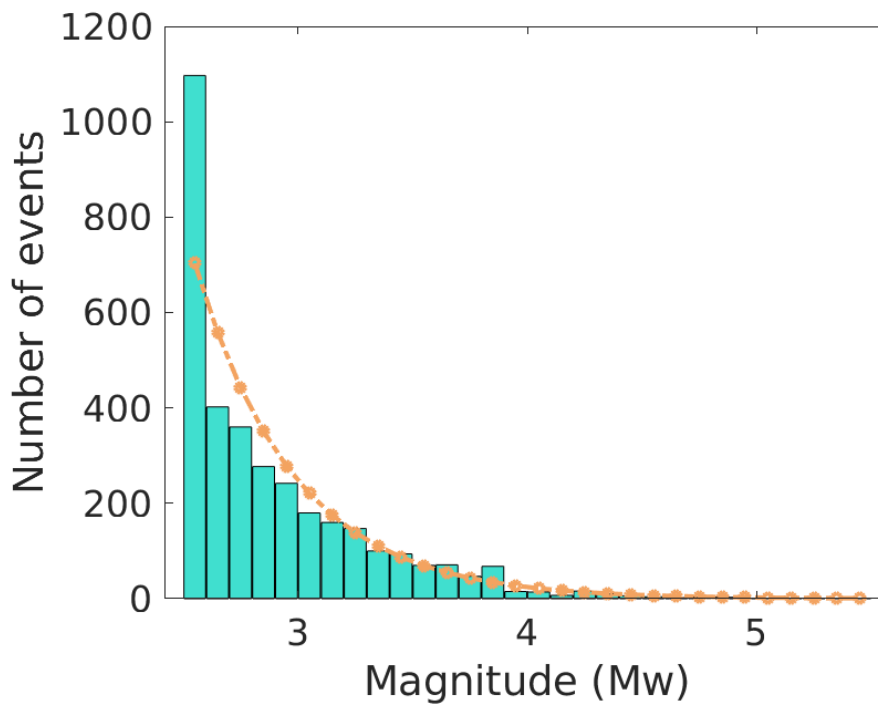


FIGURE 5.10: Histogram of the number of aftershocks without the main shock of $6.6 M_L$ per magnitude and fit to the optimal exponential (GR curve).

[60], that the b-value is smaller for earthquakes prior to the main event, we observe the opposite pattern. Those higher values than expected might be affected by the swarm activity that was observed between September 2016 to April 2017. A more specific analysis, in a manner of time, will probably result in a lower b-values for the foreshocks compare to the b-values of aftershock.

Chapter 6

Interevent Times Probability Distribution

In the present Chapter, the distribution of interevent times between successive earthquakes before the main event and after it is studied. The interevent time is defined as the time (t) between two consecutive events. In our case, interevent times are considered the times between earthquakes greater and equal to $2.0 M_w$ for the earthquakes before the main event and greater and equal to $2.5 M_w$ for the aftershocks. A total of 1262 earthquakes before the main event were obtained from seismic data collected over 2 years and 5 months, while 4692 aftershocks were obtained from seismic data collected over 7 months. Both seismic events before and after the main event were used to estimate the interevent times and represent their distribution over time for the periods from June 2016 to October 25, 2018, and from October 25, 2018 to May 2019, respectively. Different distributions were examined in the R programming environment, using the `fitdistrplus` package.

Before fitting one or more distributions to our data sets, it is useful to choose suitable candidates among a set of distributions. This choice may be guided by the knowledge of stochastic processes governing the modelled interevent times or by the observation of their empirical distribution.

Several papers study the distribution of interevent times between successive earthquakes in various data sets from all around the world [45]. Alvarez [3] proposed the Weibull distribution for the interevent times for a sequence in Turkey during the 20th, where he estimated the parameters via maximum likelihood in conjunction with the transition probabilities. Furthermore, Tomohiro Hasumi *et al.* [76], has shown that the Weibull distribution can describe the distribution of the time intervals for earthquakes occurring on a single fault, and that the Weibull exponent increases with the increase of the magnitude threshold.

In this analysis, we will investigate five different distributions, Weibull, Gamma, Pareto, Exponential, and Lognormal (see section 2.1). The temporal distribution of earthquakes before the main event, and especially for the aftershocks, might reveal interesting key features of the deep rupture complexity or underlying seismicity of the earthquake.

6.1 Interevent Times Probability Distribution For earthquakes before the main event

The time interval between each earthquake is estimated in minutes and it is illustrated in Fig. 6.1. According to our results it requires less than a day, equivalent to 1440 minutes, for a foreshock to be triggered after another foreshock for more than 80% of the interevent times. In addition, more than 65 % of the interevent times differ less than 720 minutes, and 50% of the interevent times occur in less than $\frac{1}{4}$ of a day. This means that the majority of the earthquakes from 1/6/2016 to 25/10/2018 are triggered in less than a day.

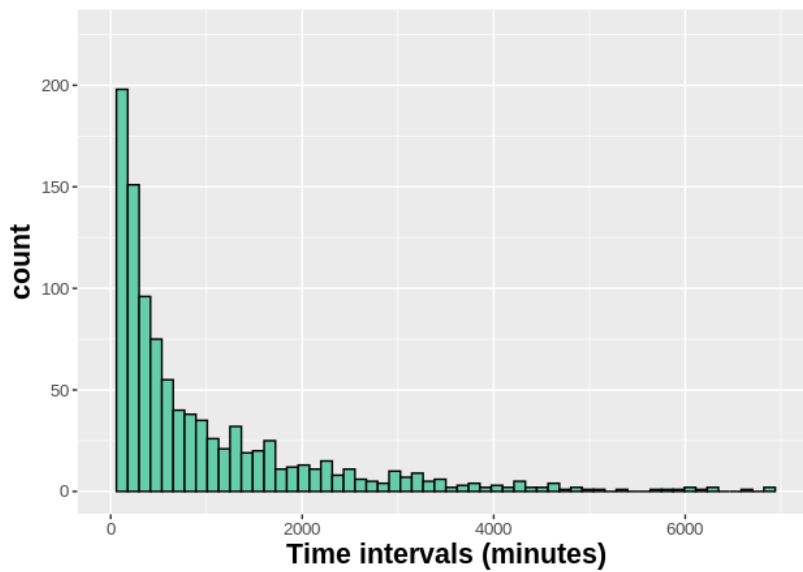


FIGURE 6.1: Histogram of time intervals between earthquakes before the main event. Time intervals are being calculated using in minutes.

In Fig. 6.1 the histogram of the interevent times before the main event is shown. In the following section we present the results for the interevent sequence and the fitted probability distributions (Weibull, Gamma, Pareto, Exponential and Lognormal). The distributions are described in Section 2.1 and their parameters are estimated using the maximum likelihood method (section 2.5).

To compare and choose the optimal model, we used the AIC and BIC (Section 2.18 and 2.19) information criteria. The plots of all the fitted distributions for the interevent times are presented in Fig. 6.2. The red colour refers to the Weibull distribution, the yellow refers to the gamma, the blue refers to the Pareto, the black refers to the exponential, and the pink refer to lognormal distribution. According to AIC (Eq. (2.18)) and BIC (Eq. (2.19)) criteria, the distribution that provides the best fit for the interevent times before the main event is the Weibull distribution, presented in Table 6.1.

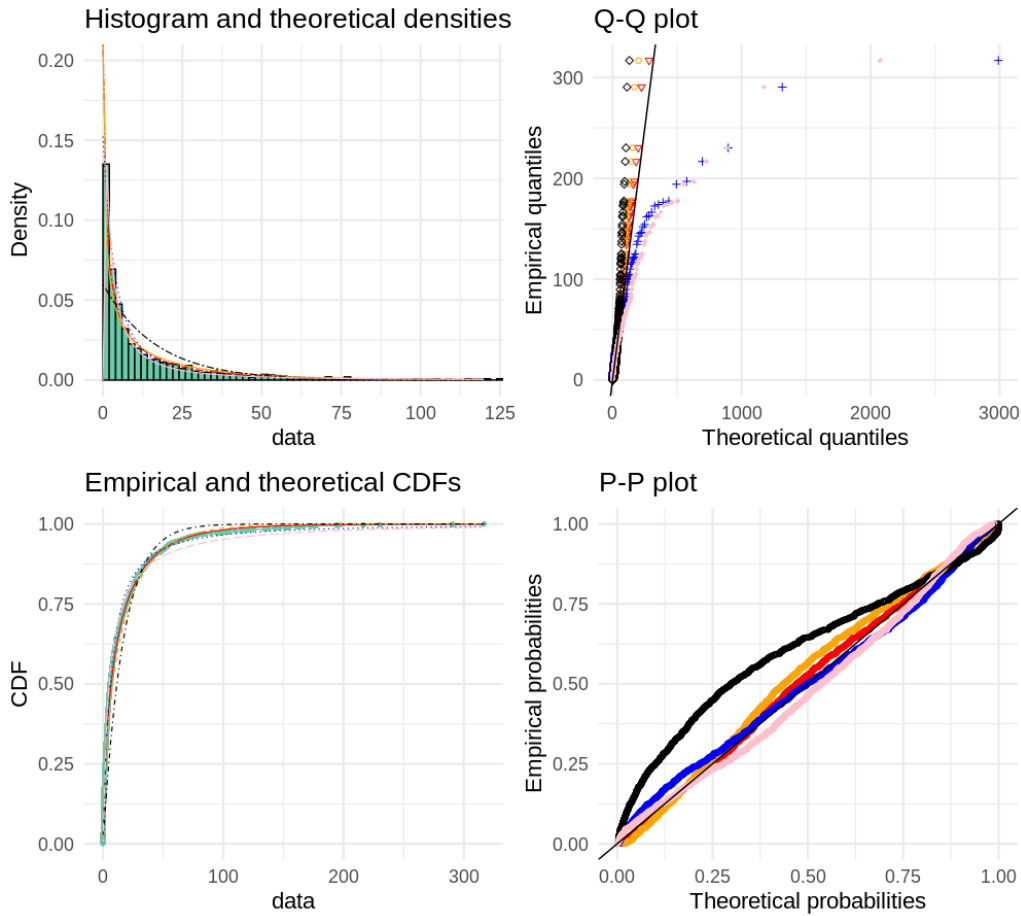


FIGURE 6.2: All distributions fitting our data. Red colour refers to Weibull distribution, yellow to gamma, blue to Pareto, black to exponential and pink to lognormal.

TABLE 6.1: Akaike Information Criterion and Bayesian Information Criterion for the earthquakes before the main event calculated according to Eq.(2.18) and Eq.(2.19) respectively. According to the AIC and BIC criteria the best distribution model for the earthquakes before the main event is the Weibull distribution.

Criterion	Weibull	Gamma	Pareto	Exponential	Log-normal
AIC	9108.861	9181.553	9153.408	9626.907	9155.173
BIC	9119.142	9191.834	9163.689	9632.047	9165.454

The Weibull distribution fitting the interevent time for the earthquakes before the main shock is presented in Fig. 6.3. The histogram of interevent times on a density scale appears on the top left corner of the plot, while the empirical cumulative distribution function(CDF) appears on the bottom left corner. On the right side of the plot, on the top corner appears the quantile-quantile plots or Q-Q plot, which draws the correlation between

a given sample and the distribution, while on the bottom the P-P plot or probability plot of the values is presented. Besides the information criteria, we can also visually observe a good agreement between the interevent times and the fitted distribution. The Weibull shape and scale parameters are presented in Table 6.1. The scale parameter is found at 11.866, and the shape parameter is estimated at 0.649, indicating a decreasing failure rate over time (see section 2.1.4).

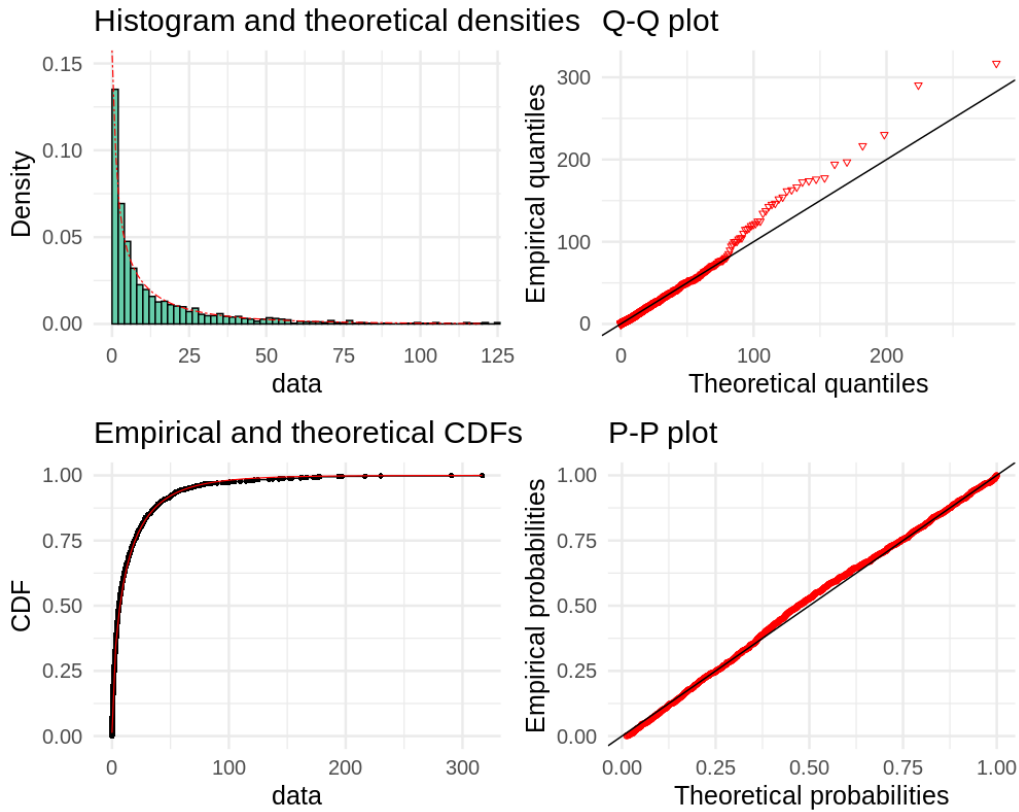


FIGURE 6.3: Fit of the interevent times of the earthquakes before the main event sequence to the Weibull distribution. Top left: Density histogram of the data and fit to the Weibull PDF. Top right: quantile-quantile plot. Bottom left: Cumulative distribution function. Bottom right: P-P plot.

TABLE 6.2: Fitting of the Weibull distribution by means of maximum likelihood

Parameters	estimate	Std. Error
shape	0.649	0.014
scale	11.866	0.544

The rest of the distributions studied herein are attached to the appendix (Fig. 9.3 for Gamma distribution, Fig. 9.5 for Exponential distribution, Fig. 9.6 for Lognormal distribution and Fig. 9.4 for Pareto distribution), since they represent inferior fitted models for the given dataset.

6.2 Interevent Times Probability Distribution For Aftershocks

The time between each aftershock triggered after the main shock, calculated in minutes, is presented in Fig. 6.4. It is clear in the figure that the majority of the events occur with time difference shorter than 100 minutes. Specifically, 80% of the interevent times for the aftershock sequence in Zakynthos differ less than 518 minutes, and more that 50% of the times differ less than 26 minutes. Approximately, the 24% of those interevent times differ less than 10 minutes ($\frac{1}{144}$ of a day). The majority of the aftershock from 25/10/2018 to 31/5/2019, happen in less that $\frac{1}{3}$ of a day.

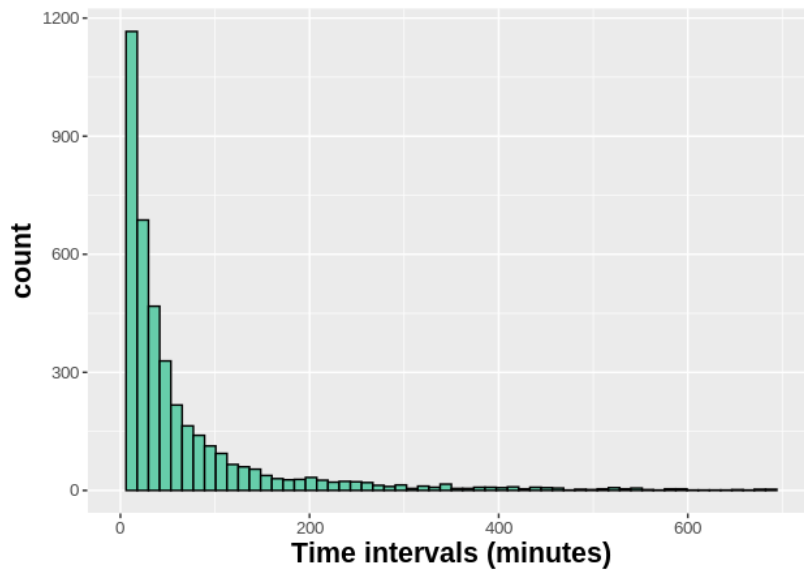


FIGURE 6.4: Histogram of interval times between aftershocks. Time intervals are expressed in minutes.

It is apparent that the aftershocks, in this case, are triggered faster compare to the interval times of the earthquakes before the main event. In the previous Chapters, we observed that aftershock sequence is denser, and in this analysis we confirm that the aftershocks are triggered consecutively.

For the interevent time series after the main event, the same distributions were fitted, and they are presented in Fig. 6.5.

In order to assess the models' performance, the AIC and BIC criteria were used. The results of the criteria are presented in Table 6.3. In the case of the interevent times for the aftershocks, the Pareto distribution gives the best fit.

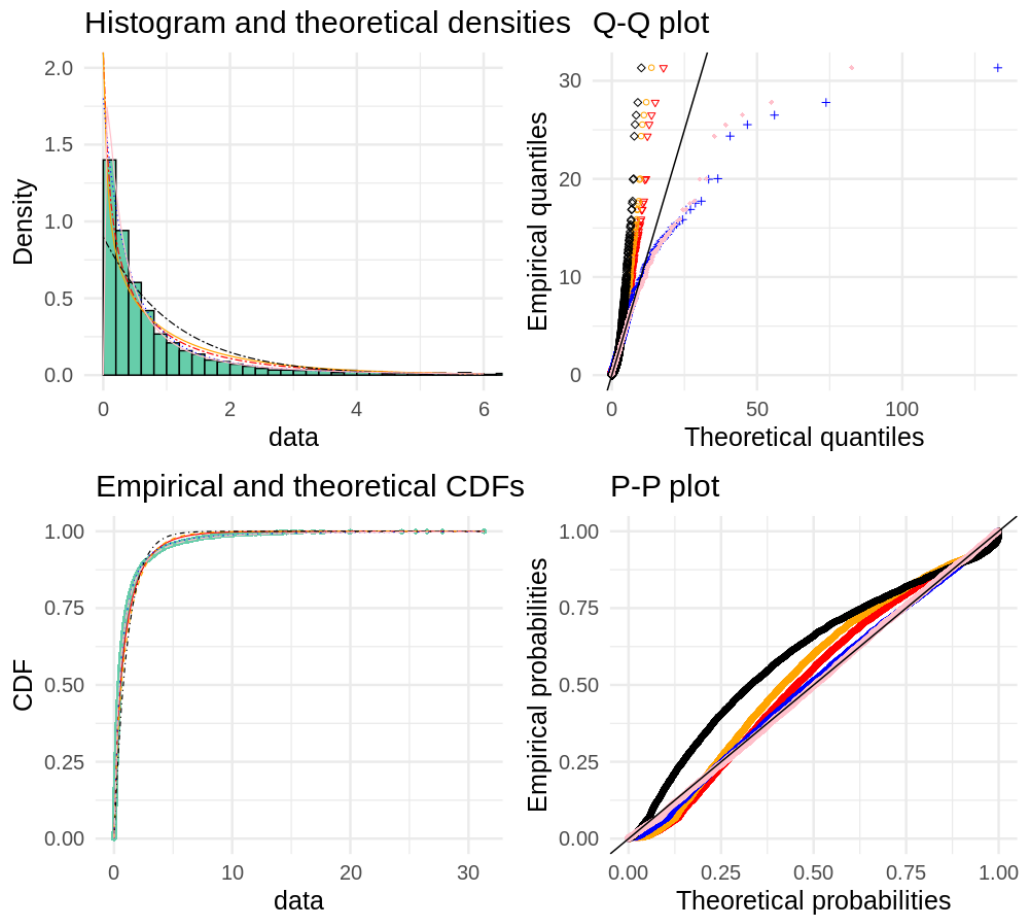


FIGURE 6.5: Fit of the interevent times of the aftershock sequence for the five different distributions. Top left: Density histogram of the data and fit to the Weibull PDF. Top right: quantile-quantile plot. Bottom left: Cumulative distribution function. Bottom right: P-P plot. Red colour refer to Weibull distribution, yellow to gamma, blue to Pareto, black to exponential and pink to lognormal.

TABLE 6.3: Akaike Information Criterion and Bayesian Information Criterion for the aftershocks calculated according to Eq. (2.18) and Eq. (2.19) respectively. According to the AIC and BIC criteria, the best distribution model for the aftershocks is the Pareto distribution.

Criterion	Weibull	Gamma	Pareto	Exponential	Log-normal
AIC	9347.918	9730.835	8844.955	10372.23	8864.526
BIC	9360.825	9743.743	8857.862	10378.68	8877.433

The Pareto distribution fitting the interevent time for the earthquakes after the main shock is presented in Fig. 6.3. The histogram of interevent times on a density scale appears on the top left corner of the plot, while the empirical cumulative distribution function (CDF) appears on the bottom left corner. On the right side of the plot, on the top corner appears the quantile-quantile plots or Q-Q plot, which draws the correlation between a given sample and the distribution, while on the bottom the P-P plot or probability plot of the values is presented. The Pareto shape and scale parameters are presented in the table 6.4, and equal to values 1.885 and 1.04, respectively.

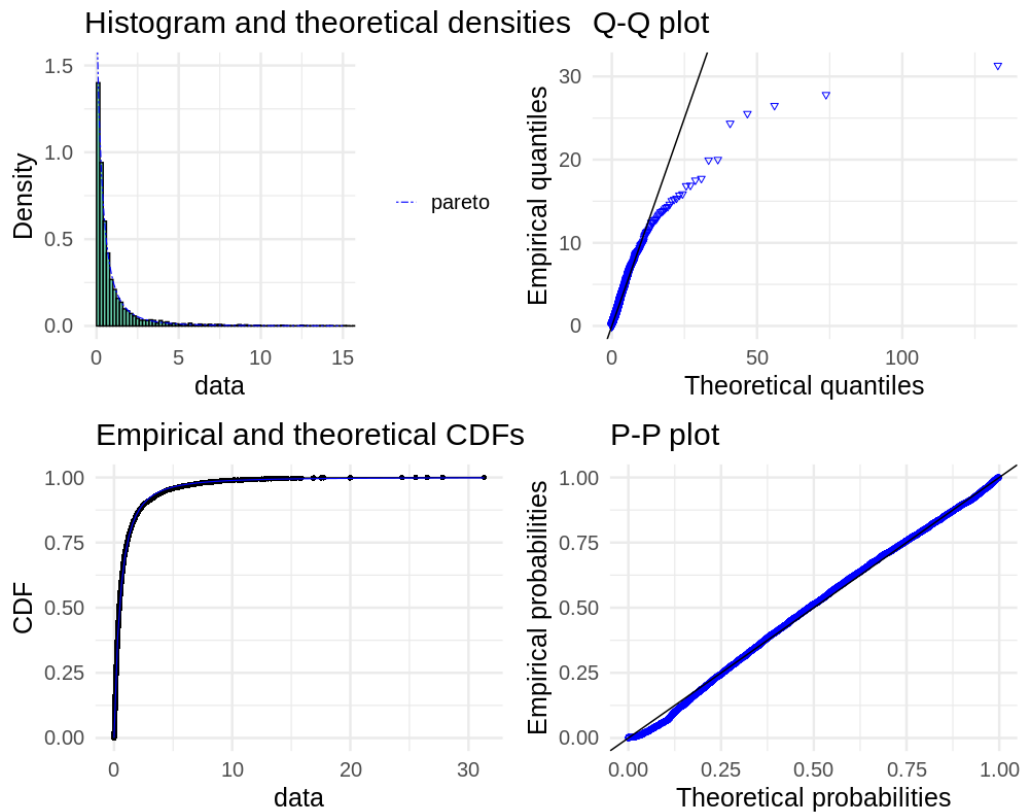


FIGURE 6.6: Fit of the interevent times of the aftershock sequence to the Pareto distribution. Top left: Density histogram of the data and fit to the Pareto PDF. Top right: quantile-quantile plot. Bottom left: Cumulative distribution function. Bottom right: P-P plot.

TABLE 6.4: Fitting of the Pareto distribution by means of maximum likelihood

Parameters	estimate	Std. Error
shape	1.8853	0.0782
scale	1.0469	0.0622

The rest of the distributions studied herein are attached to the appendix (Fig. 9.8 for Gamma distribution, Fig. 9.9 for Exponential distribution, Fig. 9.10 for Lognormal distribution and Fig. 9.7 for Weibull distribution), since they represent inferior fitted models for the given dataset.

The interevent time between two earthquakes expresses the same interevent time between two releases of energy from the fault. Knowing the interevent time between earthquake occurrences can be useful for predicting the next earthquake occurrence. Hence, the interpretation, even if these interevent times are probabilities, provides vital information for humanity.

Chapter 7

Analysis of Aftershock Frequency

It has been known since the beginning of the 20th century that aftershock activities following large earthquakes continue for months, years, or even longer. Omori's [58] proposed formula represents the decay of aftershock activity with time. Seismologists have widely used this formula and its modified form (a.k.a. Omori-Utsu law) as one of the few established empirical laws.

This Chapter presents an analysis of the aftershock sequence's temporal distribution, with the implementation of the Omori-Utsu Law (see section 3.2.2). In addition the three different parameters that express the Omori-Utsu Law (U-O), p , c and k , are estimated. Their dependence on the magnitude of completeness and on time is also investigated. A comparison of the estimated O-U parameters for Zakynthos with Hokkaido-Nansei-Oki O-U parameters, estimated by Utsu, is made because they appear to have similar quantitatively (amount of aftershocks) and temporal (duration of aftershock sequence ≈ 250 days) characteristics. Finally, a comparison is presented for the estimated O-U parameters between Zakynthos, and Kefalonia and Lefkada, which are also islands on the Ionian sea in Greece, and affected by the Hellenic trench.

7.1 Implementation of the Omori Law

Any aftershock sequence can be explained by the Omori or the Omori-Utsu law, which is unique for its power law dependence on time. The power law implies the long-lived nature of activity in contrast to the exponential function present in most decay laws in physics. Sometimes it is difficult to identify an earthquake as an aftershock triggered by the main shock, because it might reflect the background seismicity and not the aftershock sequence. However, according to Omori, the ambiguity in identifying aftershocks does not significantly affect the conclusion in many studies [78].

The aftershock sequence in this study involves all the earthquakes occurred near Zakynthos from 25th of October, 2018 until 31st of May, 2019 in an area of $\approx 20000 \text{ km}^2$. In particular, the aftershock sequence used in the following sections is a subset of the aftershock sequence where the magnitude is equal or greater than the 2.5 M_L magnitude of completeness (see section

5.1). It is imperative to note that a different M_c value will result in different Omori-Utsu parameters. While this magnitude of completeness, M_c generally considered a good estimate, the situation directly after a big earthquake it is often different, as some smaller earthquakes might be missed due to the incapacity of detectors. Both M_c and b-value, which was estimated in previous chapters (see Section 5.2), are prerequisites for the application of the Omori law and Omori Utsu Law analysis.

Regarding the law of Omori and Utsu, the temporal decay of the rate n with time is typically described as :

$$n(t) = \frac{k}{(c+t)^p} , \quad (7.1)$$

where t is the time after the large event, $p \approx 1$ is a rather universal exponent, c is a case-dependent time scale, and k is the productivity that depends on the main shock magnitude.

This means that the number of aftershocks per unit time, $n(t)$, triggered by a main earthquake, decreases at a rate of p . This rate increases significantly in a specific area after large earthquakes. The duration of seismic activity might last for months to even years.

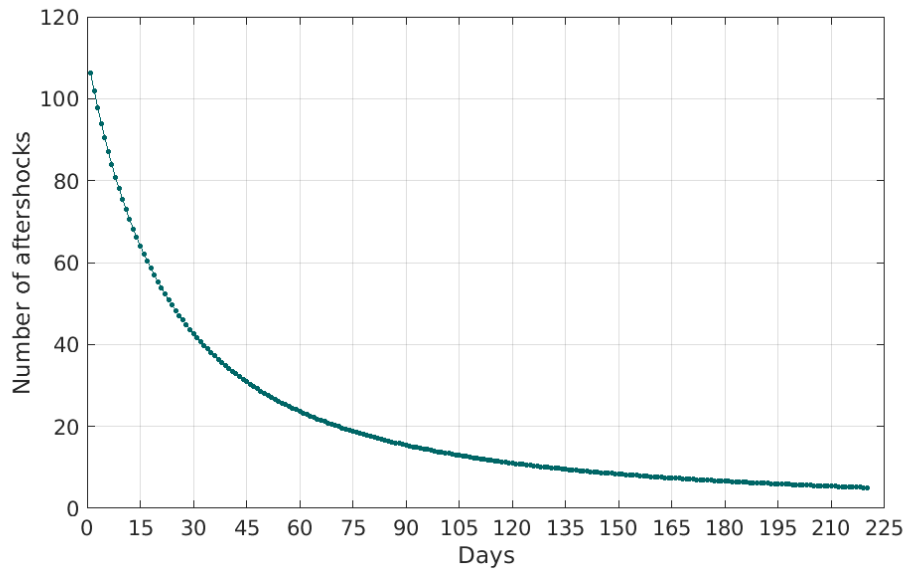


FIGURE 7.1: The decreasing rate of aftershocks since the main shock on 25, October 2018. The bluish-green circles represent the amount of earthquake events with magnitude greater than $2.5 M_L$, which happened per day. The aftershock sequence in this study lasts for 220 days after the main shock.

In Fig. 7.1, we can observe an expected decrease in the number of aftershocks as the days pass. It fits well the aforementioned law. Especially, on the first day after the main event, 109 aftershocks were triggered, as opposed to the last 10 days of the sequence (210th day to 220th day) when

less than 10 aftershocks were recorded per day. Each day after the main shock, fewer earthquakes were recorded.

7.2 Estimation of Omori-Utsu (O-U) Parameters

Continuing with the analysis of aftershock sequence, we proceed to the implementation of Omori-Utsu law. For the Omori-Utsu (7.1) application, a Matlab module called Basic Statistical Seismology [74], created by Brendan Sullivan and Zhigang Peng was used. The following results are illustrated in Fig. 7.2 and the estimated parameters of O-U law are concentrated in table 7.1). Parameters p , c and k describe the optimal predicted curve of Omori-Utsu law that fits the original data of the aftershock sequence of Zakynthos.

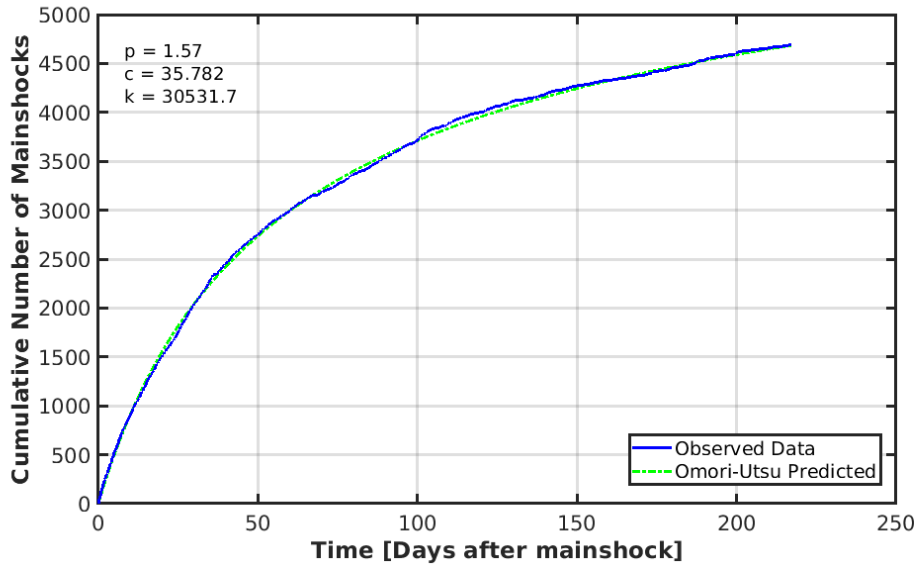


FIGURE 7.2: Estimated Omori-Utsu Law parameters (p , c , k) for the aftershock sequence. Observed versus predicted data in Zakynthos.

Figure 7.2 illustrates the cumulative number of earthquakes versus the time in days. The earthquakes following the main shock of 25 October 2018 are greater than or equal to a magnitude of completeness which equals $2.5 M_L$. This means that all the earthquakes below this magnitude were removed for this analysis. The first curve with the blue colour denotes the observed data, and the second one with the green dashed line indicates the predicted data. The prediction is really close to the observed data as the curves fit very well. In the first 50 days after the main shock we notice approximately 2750 earthquakes, while the following 50 days we see a noticeable decrease, appending another 1000 earthquakes. One hundred fifty days after the main shock until the end of the seismic sequence, only roughly

500 earthquakes were added to the aftershock sequence and as the days pass even fewer earthquakes were recorded. This verifies that the rate of the aftershocks decreases with time, as proposed in the Omori-Utsu empirical Eq. (7.1).

It is important to mention that this Matlab module has some strict boundaries for the estimates of the c and k parameters. This means that the resulting c and k would not represent the true seismic background. For this reason we expanded those limits to 50 and 50000, respectively. Also the p value according to literature is close to 1, and in this Matlab module its value can range from 0.2 to 2.7. During the last 57 years, more than 300 p value estimates have been published in at least 100 papers for aftershock sequences in various parts of the world. According to Utsu [78] p values are distributed from 0.6 to 2.5 with a median of about 1.1.

The parameters for the aftershock sequence lasting 220 days after the main shock are shown in the Table (7.1) below:

TABLE 7.1: Omori-Utsu law parameters for Zakynthos aftershock sequence, as result from the Matlab module **Basic Statistical Seismology**.

p	c	k
1.57	35.79	30531.70

The power law exponent p is equals to 1.57, which is within the range of the stated values. The productivity k is 30.532, and the c parameter, which depends on a variety of physical parameters, is 35.79.

7.3 Investigation of O-U parameters

7.3.1 Dependence of O-U Parameters on M_c

If the p value is significantly dependent on the lowest limit of magnitude M_c , the proportion of small to large aftershocks must vary with time. This means that the b-value of the Gutenberg-Richter formula, or the mean magnitude of the aftershocks, alters with time.

Omori [58], among some other seismologists seem to believe that the size of the aftershocks gradually declines with the frequency. Richter [66] attached little importance to the Omori formula, because he thought that its meaning was doubtful due to "the simple counting" aftershocks without regard to their rapidly diminishing magnitudes.

Richter recommended Benioff's strain release curves, but we rather say that its physical meaning is not clear, because the shape of the curve depends on the choice of the minimum magnitude M_c [66]. Using two examples, he showed that the dependence of the decay constant on magnitude level does not seem to be so systematic.

Utsu [78] investigated the p values for aftershock sequences for the 1957 Aleutian earthquake (9.1 M_w), the 1958 Central Alaska earthquake (7.3

M_w), and the 1958 southeastern Alaska earthquake ($7.9M_w$) by taking three different levels of M_c , and found no evidence that p and c values depend on M_c . This result is consistent with the magnitude stability (constant mean magnitude) during an earthquake sequence reported later by Lomnitz [41], Papazachos [12], and others. Yamakawa [54], who studied the aftershock sequences of the 1963 southern Kuril earthquake and the 1968 Tokachi-Oki earthquake, also suggested that p and M_c are independent. Papazachos in 1968 obtained almost equal p values ($p \approx 0.70$) for the Kremasta reservoir (Greece earthquake of 1966) for three different levels of M_c , 2.3, 2.9, and 3.5 [12]. However, Motoya and Kitagamae [48] reported in 1970 that the p value for the 1969 Hidaka Mountain earthquake increased slightly with increasing M_c ($p = 1.1$ for $M_c \geq 1.8$ and $p = 1.2$ for $M_c \geq 2.8$).

FIGURE 7.3: Maximum likelihood estimates of the parameters of the modified Omori formula for the aftershocks of the 1993 Hokkaido-Nansei-Oki earthquake for various cutoff magnitudes. Retrieved from Utsu [78].

M_z	N	K	p	c (day)
3.2	2,363	906.50 ± 97.52	1.256 ± 0.028	1.433 ± 0.170
3.4	1,582	510.43 ± 54.93	1.250 ± 0.030	0.879 ± 0.124
3.6	902	237.38 ± 26.83	1.242 ± 0.035	0.477 ± 0.088
3.8	449	91.26 ± 10.77	1.235 ± 0.042	0.190 ± 0.052
4.0	210	34.73 ± 4.68	1.246 ± 0.054	0.075 ± 0.034
4.2	117	16.30 ± 2.46	1.304 ± 0.071	0.029 ± 0.024
4.4	81	11.79 ± 2.22	1.310 ± 0.087	0.037 ± 0.033
4.6	54	6.60 ± 1.34	1.157 ± 0.083	0.004 ± 0.024
4.8	30	3.55 ± 0.96	1.107 ± 0.106	0.000 ± 0.031
5.0	14	1.59 ± 0.60	1.283 ± 0.184	0.000 ± 0.035

Utsu analysis Table 7.3 presents the maximum likelihood estimates with standard errors of p , c and k parameters. They concern the aftershock sequence of the Hokkaido-Nansei-Oki, Japan, earthquake of July 12, 1993 ($7.8 M_c$) for various M_c ranging from 3.2 to 5.0 with a 0.2 step. Considering the standard errors, no systematic variation of p with M_c is evident, and a value $p = 1.25$ seems to be appropriate, as the average value for this sequence. On the other hand, the c value decreases with increasing M_c and becomes zero for $M_c = 4.8$.

TABLE 7.2: The dependence of the p value and the other two parameters on the magnitude of completeness (M_c). All aftershocks were used from 25th of October, 2018 till the 31st of May of 2019. N is the number of aftershock for each M_c .

M_c	N	p	c	k
2.4	4693	1.57	35.78	30531.70
2.6	3295	1.59	29.10	24342.97
2.8	2247	1.49	15.49	6993.29
3.0	1471	1.45	8.94	2874.43
3.2	908	1.32	4.50	855.09
3.4	534	1.16	1.66	172.75
3.6	317	1.11	0.99	98.34
3.8	175	1.01	0.37	37.60
4.0	78	1.09	0.20	17.20
4.2	50	1.05	0.25	10

Following a similar analysis, different p , c and k values are estimated using different values of magnitude of completeness, M_c . Table 7.2 concentrates all the variations of the O-U parameters depending on the M_c and counts the number (N) of the included aftershocks each time. It is apparent that all three parameters, more or less, decrease with the increase of the magnitude of completeness.

Specifically, with a consistent increase of 0.2 magnitude (M_c), we can notice a decrease in the p value in almost all cases. Productivity k also shows a decreasing rate with the increase of M_c , because the higher the magnitude the fewer number of aftershocks are included in the formula of Omori-Utsu (N). The c value decreases with increasing M_c and approaches a value close to zero for $M_c = 4$, corresponding to less than 5 hours.

Summing up, the p parameter varies from 1.01 to 1.57, with an average value of $p = 1.28$ and indicates a dependence on the the magnitude of completeness. The c and k parameters follow a more rapid decrease with the increase of the magnitude M_c .

Comparing the results of Zakynthos Table 7.2 with the parameters of the Hokkaida-Nansei-Oki Table 7.3 we came across the following results. Both cases examine the similarity in the duration of the aftershock sequence lasting 262 days in Japan and 220 days in Greece. The magnitude of completeness M_c , in the first case, varies from 3.2 to 5.0 and in the second one from 2.4 to 4.2. We notice that in Hokkaida-Nansei-Oki the M_c generally takes higher values, probably due to Japan's intense seismic background. In both cases, a decaying rate of Omori-Utsu c and k parameters is apparent with respect to the increase of M_c . While in Hokkaida-Nansei-Oki the p value generally remains consistent with a small variation and no indication of dependency on M_c , in Greece, the p values seems to depend on M_c and present a more intense variation. The average p value in our data equals 1.28, a value close to the 1.25 p parameter of Japan analysis. Moreover, c

parameters of Japan tend to have much smaller values in comparison to the c parameters in Zakynthos. This might be explained by the wide boundaries of c parameter inside the Matlab code.

The exact nature of the law parameters and their dependencies are still in discussion. For example, the exact origin of the parameter c is still under debate. The most recent results suggest that it is of physical rather than instrumental origin [63], and it varies according to the faulting system and the underlying stress [51]. In addition, these recent results speculate that c parameter might depend on how aftershocks are defined (dependence with M_c), as opposed to the former opinions of the 20th century.

In the following Figure 7.4, 7.5, and 7.6 the dependence on M_c with each parameter of Omori-Utsu law is presented. The started value of magnitude of completeness is 1.8 with step 0.2.

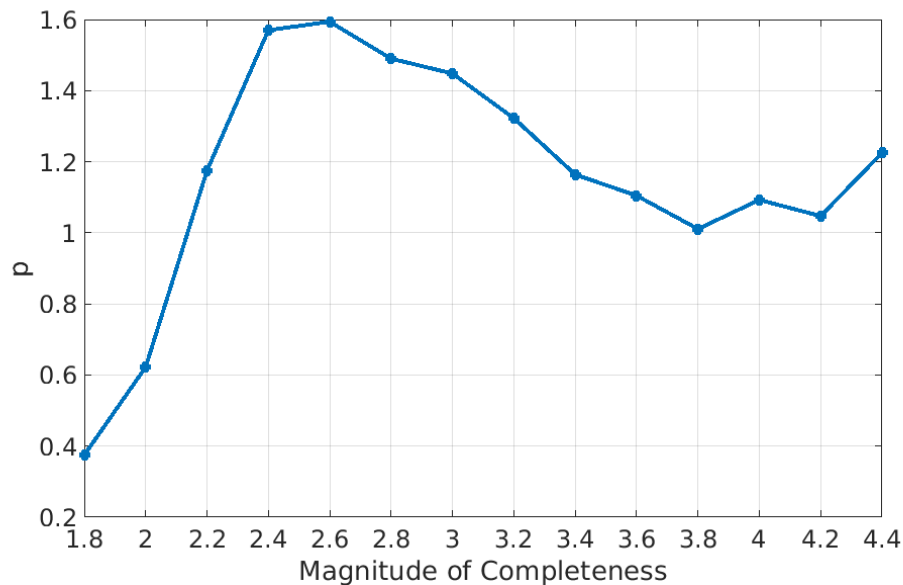


FIGURE 7.4: Dependence on p parameter with magnitude of completeness M_c . The 4.4 M_c include 22 events, while 1.8 M_c , 2 M_c and 2.2 M_c include 8541, 7423, 6111 events, respectively.

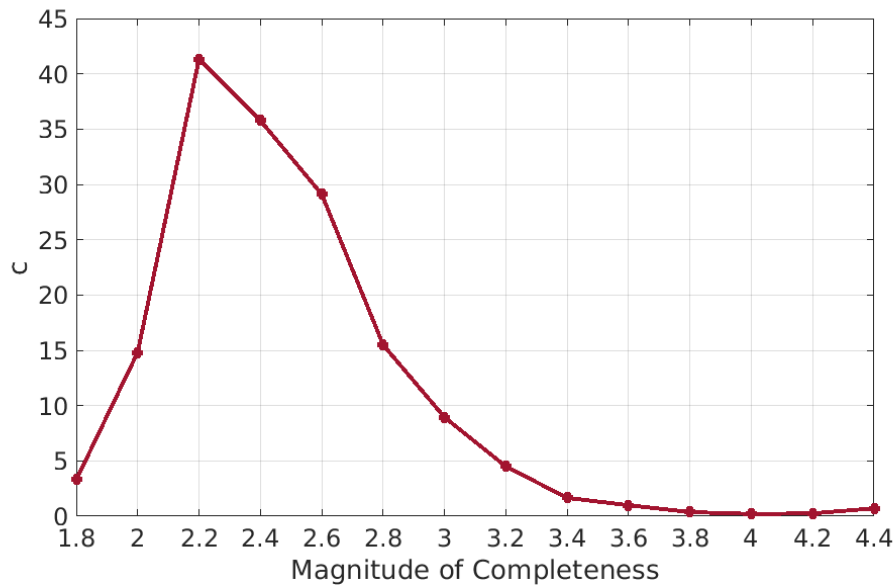


FIGURE 7.5: Dependence on c parameter with magnitude of completeness.

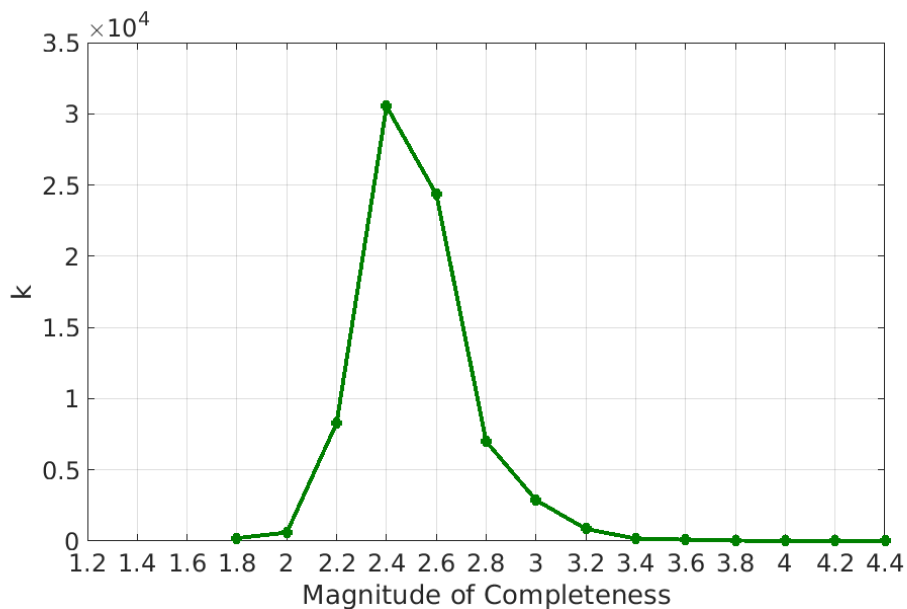


FIGURE 7.6: Dependence on k parameter with magnitude of completeness. With the increase in the values of M_c , fewer aftershocks are included in the formula. For 4.4 M_c we use 22 events.

7.3.2 Dependence of O-U Parameters over time

This section examines the evolution of Omori-Utsu parameters over time and if and how much they depend on it. The following Table 7.3 was created for the estimation of the O-U parameters using a time window of 20 days for the aftershock sequence of Zakynthos. After defining the parameters of Zakynthos, we compare them with the O-U parameters of Kefalonia and Lefkada.

TABLE 7.3: The evolution of Omori-Utsu parameters using a time window of 20 days for the aftershock sequence with M_c equal to $2.5 M_L$. The step that is used is 20 days, from the day after the main shock 25th of October until the 31st of May, 2019.

Days	p	c	k
20	0.38	1.55	172.35
40	0.40	1.88	183.67
60	1.19	22.65	4675.47
80	1.40	27.99	12 167.76
100	1.30	25.76	7817.45
120	1.23	23.45	5559.93
140	1.42	30.03	14 010.73
160	1.52	33.60	23 080.90
180	1.59	36.58	34 094.51
200	1.53	34.17	24 254.59
220	1.57	35.79	30 531.70

The evolution of p parameter as illustrated in Fig. 7.7 indicates a generally upward trend over time. The same behaviour is also noticeable both for c and k parameters as they are illustrated in the same figure. The p parameter is closest to one, two months (≈ 57 days) after the main shock, where c equals 22.65 and k equals 4675.47.

Small p values, as appeared here for a period shorter than 40 days, have often been reported for superposed sequences. The superposed sequences consist of mostly small sized sequences (one or a few aftershocks). A portion of these may not be real aftershocks; they may only represent background seismicity [78]. Relatively small p values have also been found for aftershock sequences in China in a study by Zhao *et al.* [85]. They obtained maximum likelihood estimates of p and c values for 32 aftershock sequences. The p value ranges from 0.63 to 1.54, with a mean of 0.95.

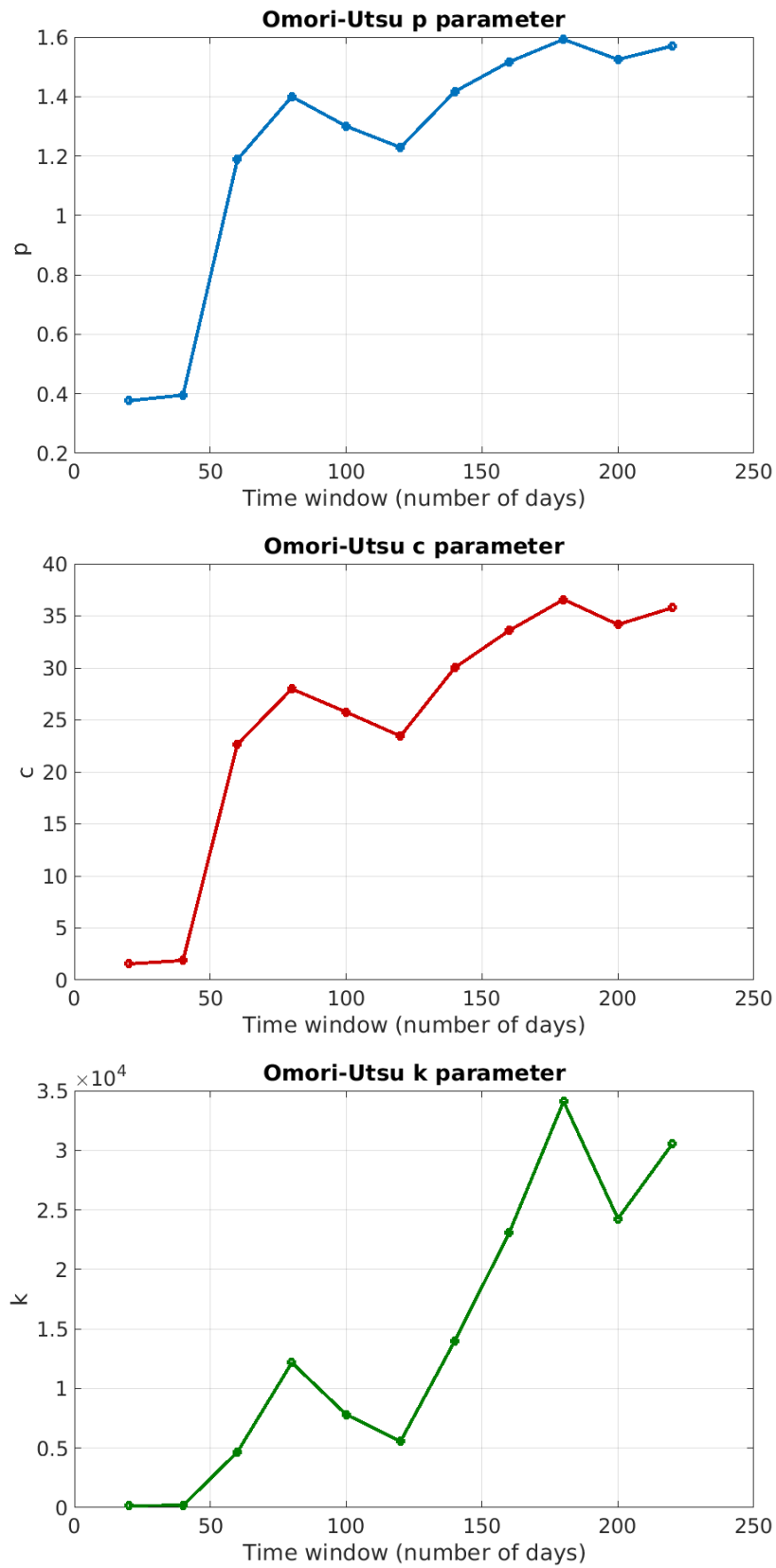


FIGURE 7.7: The evolution of p , c and k parameters over time. Time window of 20 days was used.

7.3.3 Comparison of O-U Parameters with Kefalonia and Lefkada

D. Chorozoglou and E. Papadimitriou [11] investigate the parameters of Omori-Utsu law for Kefalonia and Lefkada, two Ionian islands close to Zakynthos. For Kefalonia, the aftershock sequence started on 26/1/2014 with a main shock equal to $6.1 M_L$, and for Lefkada the main shock of $6.0 M_L$ began on 17/11/2015. Because all three islands belong to a similar, if not the same, tectonic background (Hellenic trench), and are affected by the same faulting systems, we compare the estimated Omori-Utsu parameters in the following Table 7.4. In addition, their main shocks $6.1 M_L$ for Kefalonia and $6.0 M_L$ for Lefkada, are close to Zakynthos $6.6 M_L$ main shock.

TABLE 7.4: Comparison of the Omori-Utsu law parameters of Zakynthos with two Ionian islands. The aftershock sequence lasts for 20 days in each case. The N in the table refers to the cumulative number of earthquakes. The data used for Zakynthos was calculated while for Kefalonia and Lefkada it was retrieved from paper [11].

Case	Days	N	p	c	k
Zakynthos	20	1400	0.38	1.55	172.35
Kefalonia	20	1600	0.46	5	229.1
Lefkada	20	1800	1.08	4.886	1277.1

In Table 7.4, we notice similar results for the cumulative number of earthquakes for all of the islands, with Zakynthos having the fewer. This depends on the choice of M_c ; a high value of M_c might exclude many aftershocks, while a value too low might include a lot more earthquakes than needed. Kefalonia and Lefkada might use a small M_c , which leads more frequent aftershocks with smaller magnitudes.

The parameter p appears to be very low, with values 0.38 for Zakynthos and 0.46 for Kefalonia. Literature suggests that the p parameter expresses the rate of the aftershock sequence and usually takes values close to 1. The low values of Zakynthos and Kefalonia in a time period of 20 days represent a slow rate and may indicate that the aftershock sequence has not finished and perhaps not even started yet. On the contrary, Lefkada's p value equals 1.08 (near 1), which might indicate the end of the aftershock sequence after 20 days. This also agrees with the high productivity in Lefkada compared to Zakynthos and Kefalonia. Usually, a high productivity k corresponds to a high rate.

For strong main earthquakes, the failure of observing systems at stations close to the epicenter makes small events more difficult to detect. In such circumstances, the c value may be overestimated. If the observation of the aftershock sequence starts immediately after the main shock, the true c values become less challenging to estimate. When data is taken from ordinary earthquake catalogs, the estimated c value may partially reflect the effect

of incomplete detection of small aftershocks shortly after the main shock. The exact nature of the law parameters and their dependencies are still in discussion. Finally, more investigation is needed to define the duration of aftershock activity. More specifically, the time required for aftershock activity to decrease to the level of normal background seismicity and, if high or low p , can contribute to that definition.

Chapter 8

Conclusions and Future Directions

In the present study, different statistical and geostatistical tools were applied to the seismic sequence of the island of Zakynthos. The aim was to investigate the intense main shock of October 25th, 2018, measured at 6.6 M_L , which was felt in the entire country. Specifically, the study focuses on the magnitudes and times of the seismic events in the period from June 2016 until May 2019, i.e., a period of three years. The area's seismic activity (as measured by the number of events) was much more intense after the main earthquake. We studied both the earthquakes prior to and after the main event. The study has four distinct objectives.

The first objective was to perform an exploratory analysis of the seismic event sequence. First, we found the optimal relationship between the local magnitude scale and the moment magnitude scale using regression analysis. The events used for the investigation are 55 events around Zakynthos, acquired for an extended time period between backdated from 2010 to 2019. Our results for the relationship between M_L and M_w are based on weighted linear regression, using a weight equal to the square root of the moment magnitude. The estimated transformation (4.2) is in agreement with available empirical equations in the literature. The coefficient of determination R^2 is estimated at 0.866, and the p-value of this model equals $8.13e^{-25}$, indicating high significance of the statistical results.

We then used this empirical relation to derive the moment magnitude from the recorded local magnitudes, for the initial period of this study. By plotting those magnitudes over time, a seismic quiescence was noticed from August 2017 until right before the main shock. Subsequently we estimated the seismic moment, for our initial data set by applying an empirical equation proposed by Papazachos'. Papazachos' equation was used because it refers to an area and earthquakes with the same seismotectonic background and characteristics as the Zakynthos sequence. By plotting the seismic moment, four phases describing the energy release were determined. The first phase was ambiguous, the second appeared stable, and in the third and fourth phases, a small and larger increase in energy release was noticed, respectively.

The second objective focuses on the investigation of the Gutenberg Richter Law. In particular, we determined the magnitude of completeness (M_c) and the b-value from the above earthquake catalog. We studied the sequences

of earthquakes separately before the main event and aftershocks. We tested three different methods for estimating M_c , and we found that their results differ by no more than $\pm 0.1 M_w$, both for earthquakes before the main event and aftershocks. The average values for M_c are $2.1 M_w$ and $2.5 M_w$, respectively. The next step was to apply the estimated M_c in the Gutenberg Richter equation in order to determine the b-value. As expected, different M_c values led to different b-values. We selected as optimal the M_c value which yields a b-value close to 1.

For the earthquake sequence before the main shock the resulting b-value equals 1.18, using M_c equal to $2.0 M_w$. For the aftershock sequence the resulting b-value equals 1.0 using an M_c equal to $2.5 M_w$. Both b-values are generally in agreement with b-values observed worldwide, which are near unit [66]. In addition, they are close to the respective b-values obtained in a recent study by Mouslopoulou *et al.* [49], referring to the same area with a similar period. Their mean b-value of the aftershock sequence is 1.18 ± 0.12 . Moreover, in their analysis, they report a decrease of the b-value calculated for the period from May 2017 until the main shock on October 25, 2018, compared to the b-value estimated for earlier times. This decrease of the b-value appeared also in our study (shown in Fig. 5.2), where we found b-values below 1 during the period from April 2017 to September 2018. While it has been shown [60], that the b-value is smaller for earthquakes prior to the main event than for the aftershocks, in our case, we observe the opposite situation. Those elevated values is probably the outcome of the swarm activity observed from September 2016 to April 2017.

The third objective was to analyze the temporal distribution between earthquakes. We aimed at finding the distribution that fitted best the interevent times, both prior to and after the main event. By applying five different probability distributions (Weibull, Gamma, Pareto, Exponential, and Lognormal) and utilizing the Akaike information criterion (AIC) as well as the Bayesian information criterion (BIC), those distribution models were compared, and the optimal model was selected. The distribution that provided the best fit for the interevent times before the main event was the Weibull distribution, while the one that gave the best fit for the aftershock sequence was the Pareto distribution. These distributions could be used to predict the evolution of the aftershock sequence in the future.

The fourth objective focuses on the analysis of the temporal distribution only for the aftershock sequence of Zakynthos. The analysis was divided into the implementation of both Omori and Omori-Utsu (O-U) Law, and the investigation of the O-U parameters dependencies. The aftershock sequence is related to all the earthquakes near Zakynthos island from 25/10/2018 to 31/5/2019 in an area of $\approx 20000 \text{ km}^2$. Moreover, the sequence used corresponds to values with magnitude equal or greater to the magnitude of completeness, which was found to be $2.5 M_w$. The predicted curve of Omori-Utsu law fitted very well the original data of the aftershock sequence. The resulting O-U parameters for the aftershock sequence of Zakynthos were estimated as $p = 1.57$, $c = 35.79$ (days) and $k = 30531.70$.

Following the analysis of the parameters, the dependence of them on

the magnitude of completeness was tested. Even though many seismologists [78, 54, 41] support the independence between p and M_c , we found a slight dependence of M_c on all three parameters. In particular, we found that an increase of M_c resulted in a constant decrease of the O-U parameters. To confirm our results, a comparison of the estimated O-U parameters for Zakynthos with Hokkaido-Nansei-Oki, Japan parameters, estimated by Utsu [78], was made because they appear to have similar quantitatively (amount of aftershocks) and temporal (duration of aftershock sequence ≈ 250 days) characteristics. The results indicated that the p parameter for Zakynthos depended on M_c , while there was no apparent systematic variation for the Hokkaido-Nansei-Oki p parameter.

Finally, an investigation was performed on dependencies of these O-U parameters for Zakynthos on time (20 days time window) and a comparison with the estimated O-U parameters estimated for Kefalonia and Lefkada (for a 20-day aftershock sequence). These two islands belong to Greece and especially to the Ionian sea, thus they are affected by the Hellenic trench, and they should appear to have the same seismotectonic characteristics. The results indicated that for the 20 days aftershock sequence, Zakynthos' and Kefalonia's p parameters appeared very low (0.38 and 0.46, respectively), while for Lefkada it appeared close to 1. Even though we confirmed the validity of the proposed O-U hypothesis and its parameters fitted very well to the original data for Zakynthos, the parameters dependencies on time and magnitude of completeness need more investigation. While they appear to depend both on time and on M_c , these dependencies might reflect a background seismicity or even express the underlying stress. The exact nature of the law parameters and their dependencies are still in discussion. Finally, more investigation is needed to define the duration of aftershock activity. More specifically, the time required for aftershock activity to decrease to the level of normal background seismicity and, if high or low p , can contribute to that definition.

Future Directions

In future research, the relationship between moment-local magnitude and the distance of the seismic stations could be examined exhaustively. Since there are indications that seismic stations near the epicenter tend to overestimate the magnitudes, more investigation about this dependence is needed.

In addition, a comparison of magnitude data set derived from identical record data sets (describing the same seismic events) could be made by applying both traditional (seismograph) and new standard measurement procedures (seismometer). In this way, it is possible to minimise errors that refer to incapacity and inaccuracy of equipment and create standardized conversion relationships. Another point of interest could be to find if there is any dependency between seismic quiescence and b-value (Gutenberg Richter law). Since both might prelude an earthquake it would be interesting to find a relation, if any, and reduce the boundaries of uncertainty.

The two proposed models from the temporal distribution analysis of the interevent times (Chapter 6), can be further analysed to create models to predict the upcoming seismic behavior or detect any unusual sequence.

Finally, for the estimation of the p parameter (Chapter 7), the Omori Utsu law was used; there are alternative methods that could estimate the p parameter. One of them is the Epidemic Type Aftershock Sequence, ETAS. A model of ETAS could be created to estimate the p , and then the respective values could be compared with those drawn from the present analysis. In the same analysis, additionally, the duration of the aftershock sequence could be investigated. Subsequently, more research need to be done on the p parameter to determine whether it could be treated as an indicator of the duration of aftershock sequence.

Chapter 9

Appendix

Estimation of b-value for the aftershocks with $M_c = 3.5 M_w$.

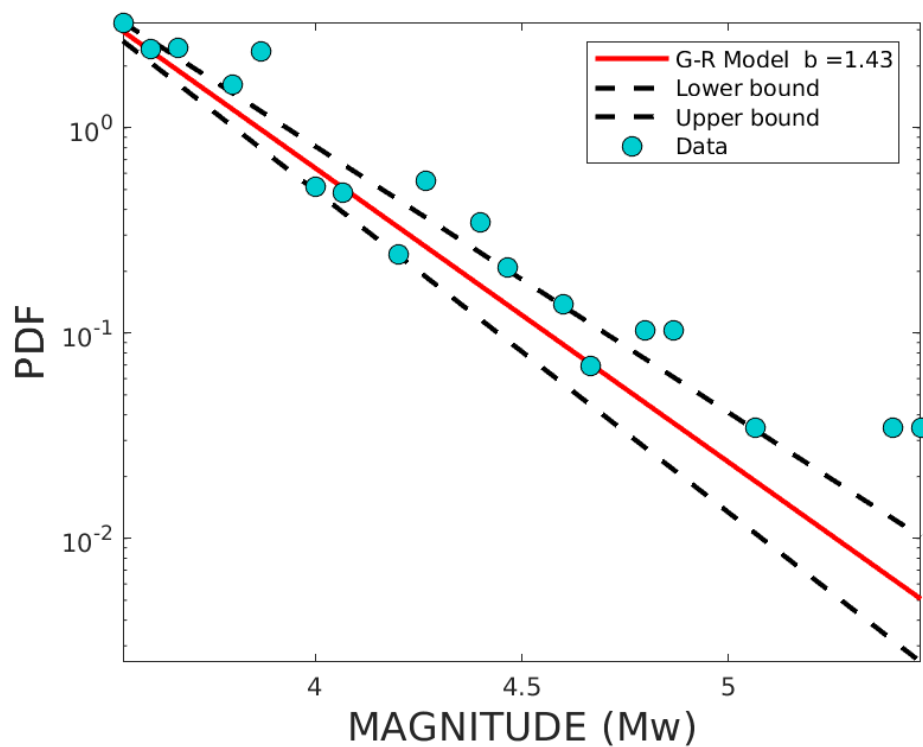


FIGURE 9.1: Histogram of probability density function versus event magnitude for aftershocks (without main event), using logarithmic vertical scale. $M_c = 3.5$

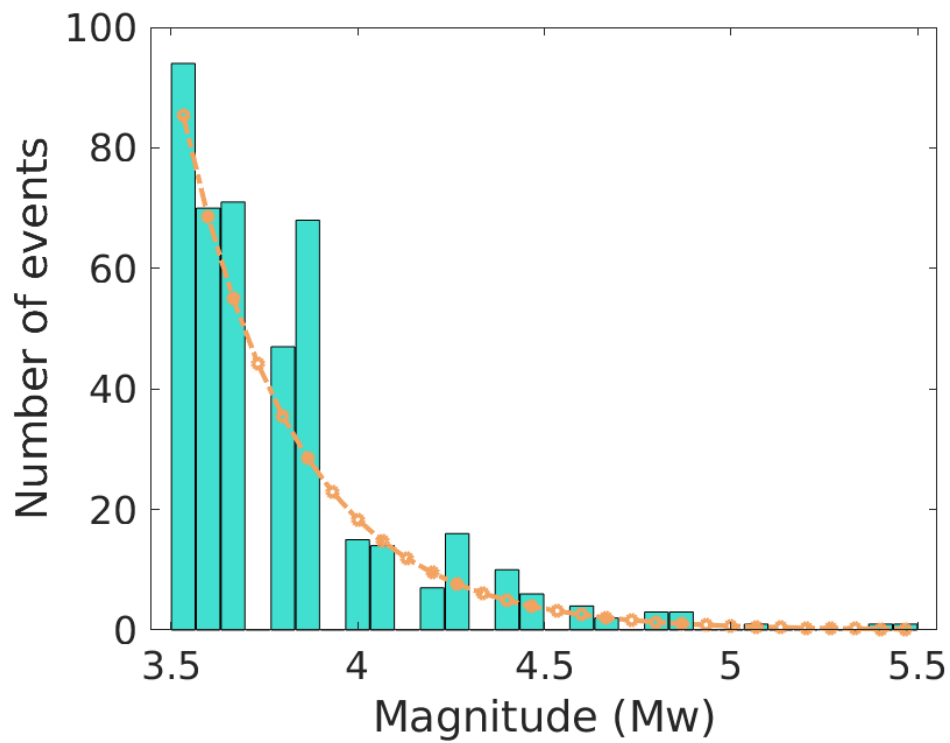


FIGURE 9.2: Histogram of the number of aftershocks without the main shock of 6.6 M_L per magnitude and fit to the optimal exponential (GR curve). $M_c = 3.5$

Different distributions tested for the earthquakes before the main shock.

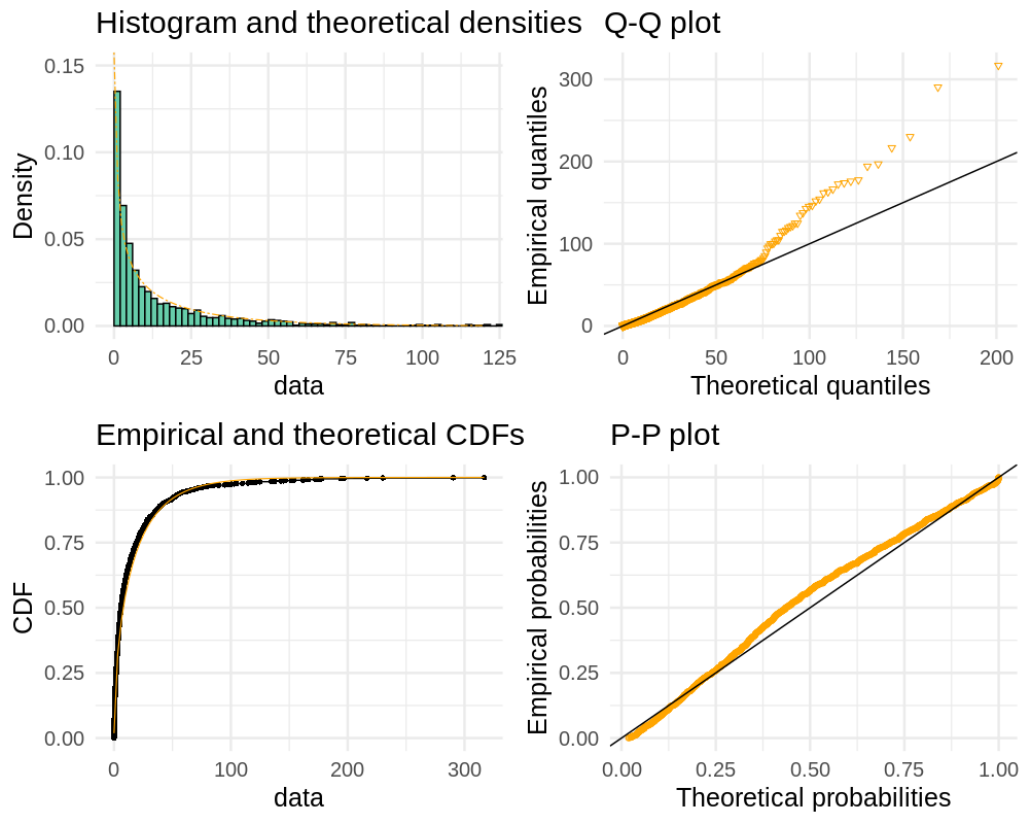


FIGURE 9.3: Fit of the interevent times of the earthquakes before the main event to the Gamma distribution. Top left: Density histogram of the data and fit to the Gamma PDF. Top right: quantile-quantile plot. Bottom left: Cumulative distribution function. Bottom right: P-P plot.

TABLE 9.1: Fitting of the Gamma distribution by means of maximum likelihood

Parameters	estimate	Std. Error
shape	0.5290	0.0175
rate	0.0317	0.00161

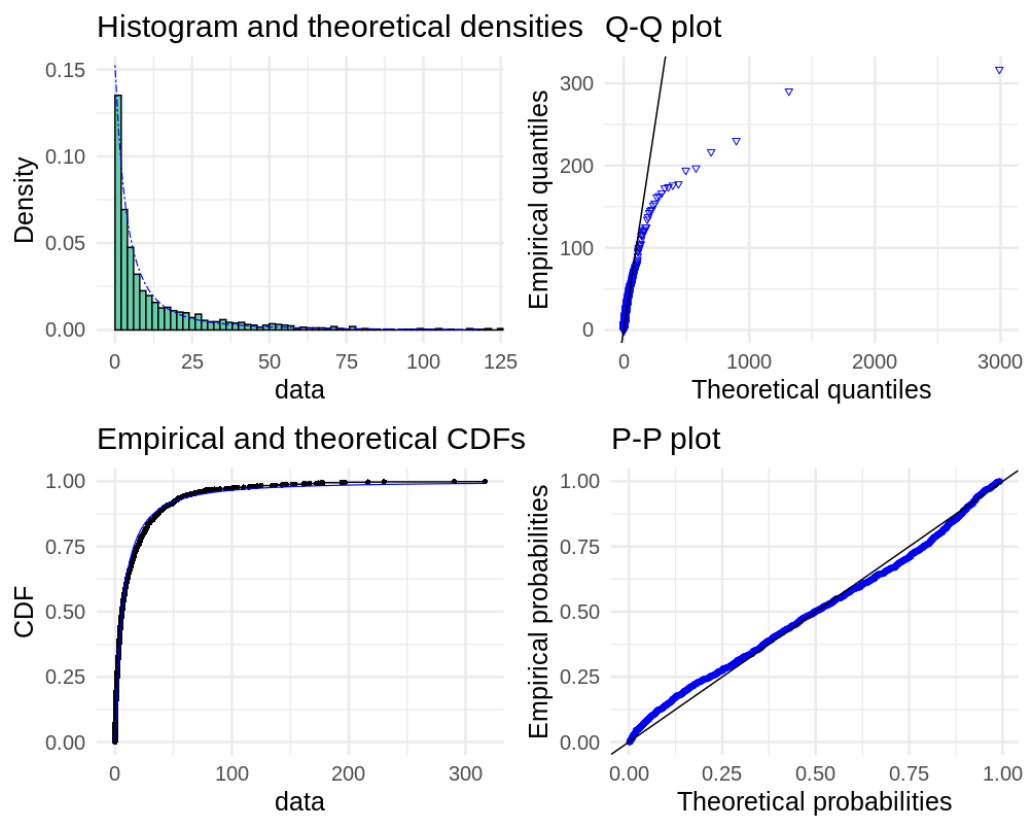


FIGURE 9.4: Fit of the interevent times of the earthquakes before the main event to the Pareto distribution. Top left: Density histogram of the data and fit to the Pareto PDF. Top right: quantile-quantile plot. Bottom left: Cumulative distribution function. Bottom right: P-P plot.

TABLE 9.2: Fitting of the Pareto distribution by means of maximum likelihood

Parameters	estimate	Std. Error
shape	1.3438	0.1018
scale	8.8161	1.0818

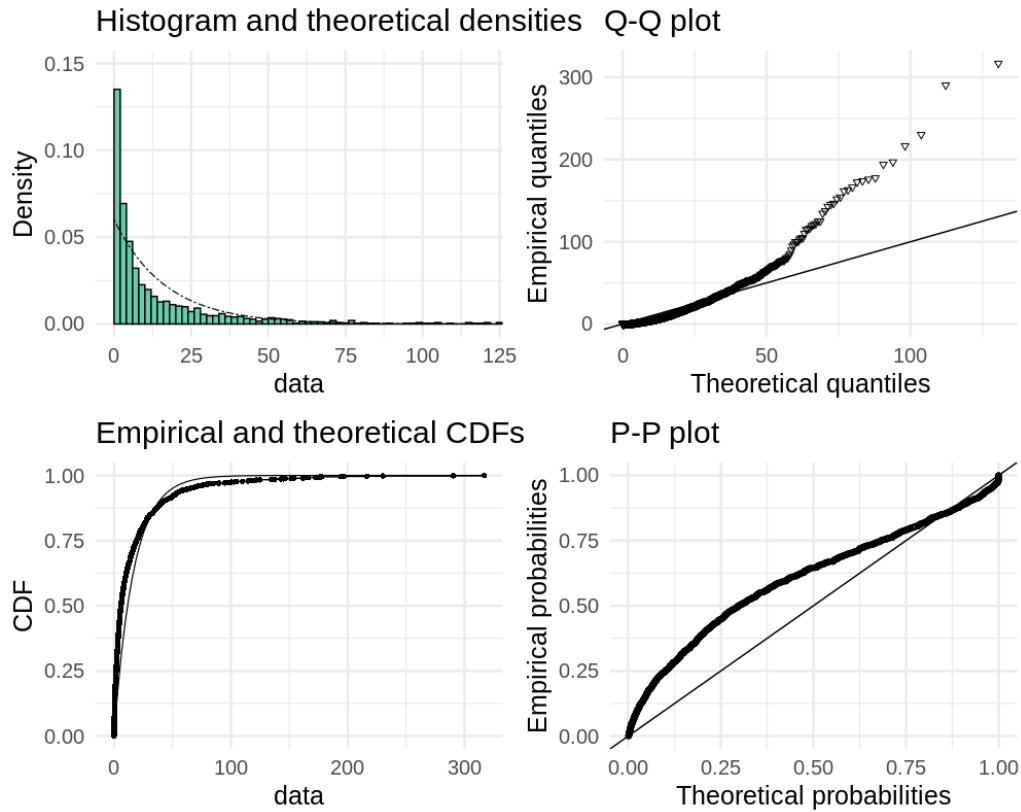


FIGURE 9.5: Fit of the interevent times of the earthquakes before the main event to the Exponential distribution. Top left: Density histogram of the data and fit to the Exponential PDF. Top right: Quantile-quantile plot. Bottom left: Cumulative distribution function. Bottom right: P-P plot..

TABLE 9.3: Fitting of the Exponential distribution by means of maximum likelihood

Parameters	estimate	Std. Error
rate	0.0600	0.0017

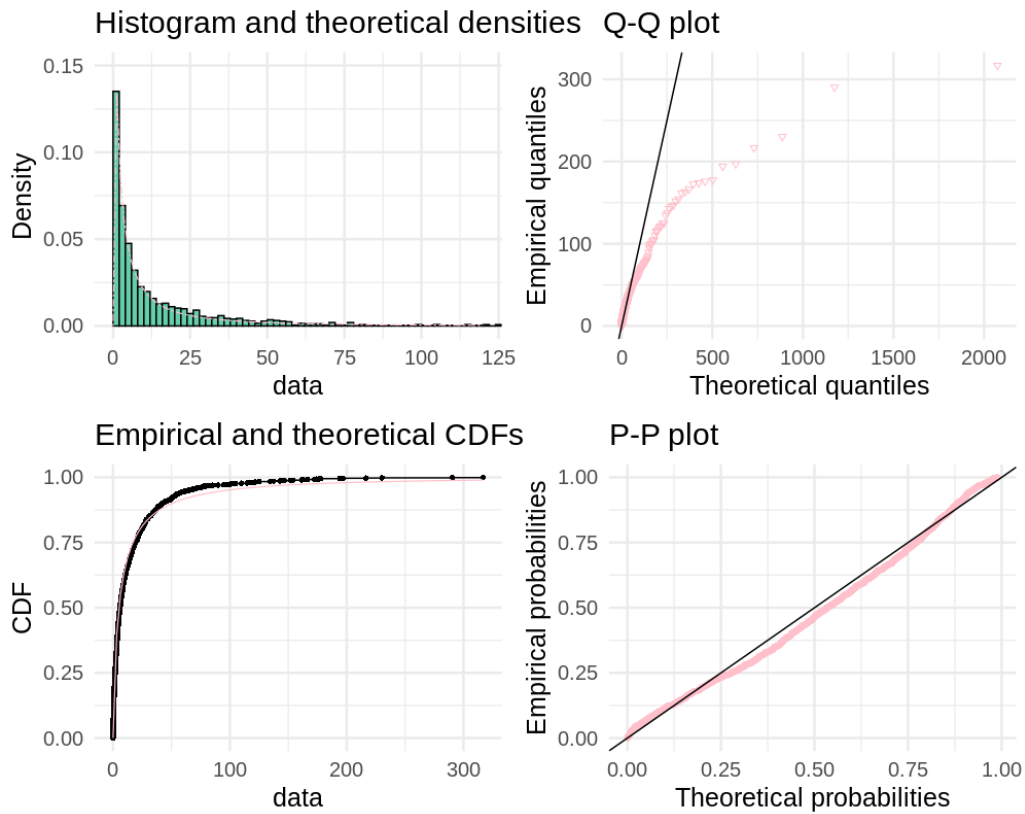


FIGURE 9.6: Fit of the interevent times of the earthquakes before the main event to the Lognormal distribution. Top left: Density histogram of the data and fit to the Lognormal PDF. Top right: quantile-quantile plot. Bottom left: Cumulative distribution function. Bottom right: P-P plot.

TABLE 9.4: Fitting of the Lognormal distribution by maximum likelihood

Parameters	estimate	Std. Error
Logarithmic mean	1.6233	0.0504
Logarithmic standard deviation	1.7922	0.0357

Different distributions tested for the aftershocks.

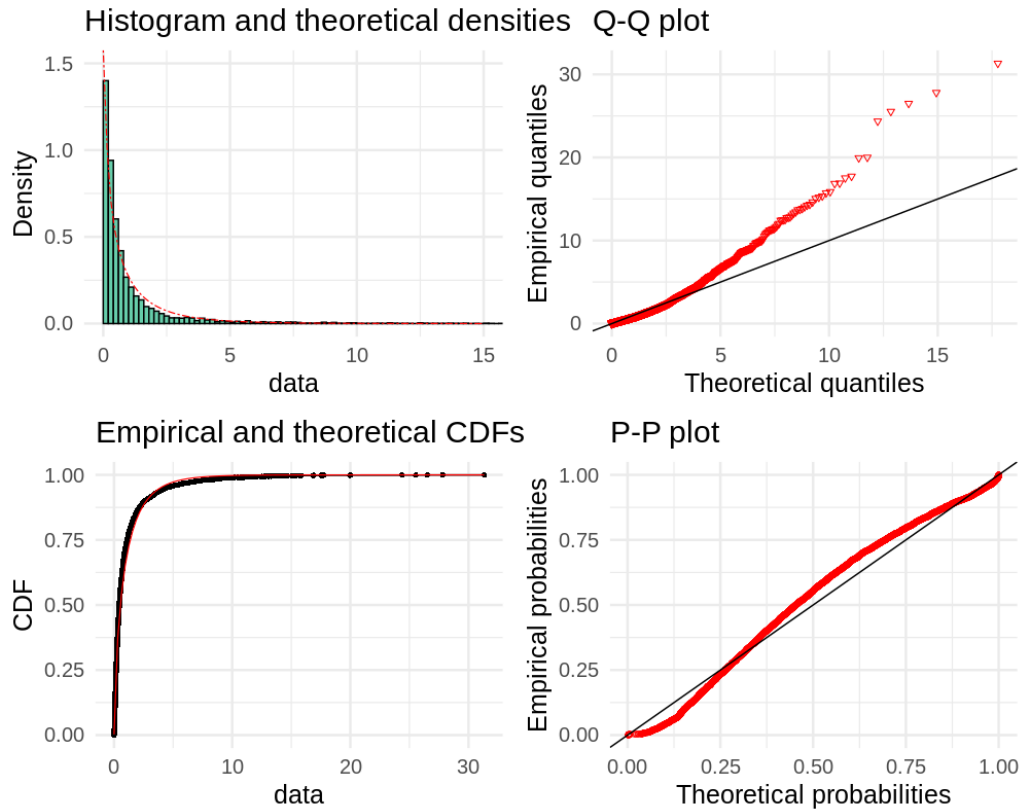


FIGURE 9.7: Fit of the interevent times of the aftershock sequence to the Weibull distribution. Top left: Density histogram of the data and fit to the Weibull PDF. Top right: quantile-quantile plot. Bottom left: Cumulative distribution function. Bottom right: P-P plot.

TABLE 9.5: Fitting of the Weibull distribution by means of maximum likelihood estimation.

Parameters	Estimate	Std. Error
shape	0.73672	0.0077
scale	0.8806	0.0185

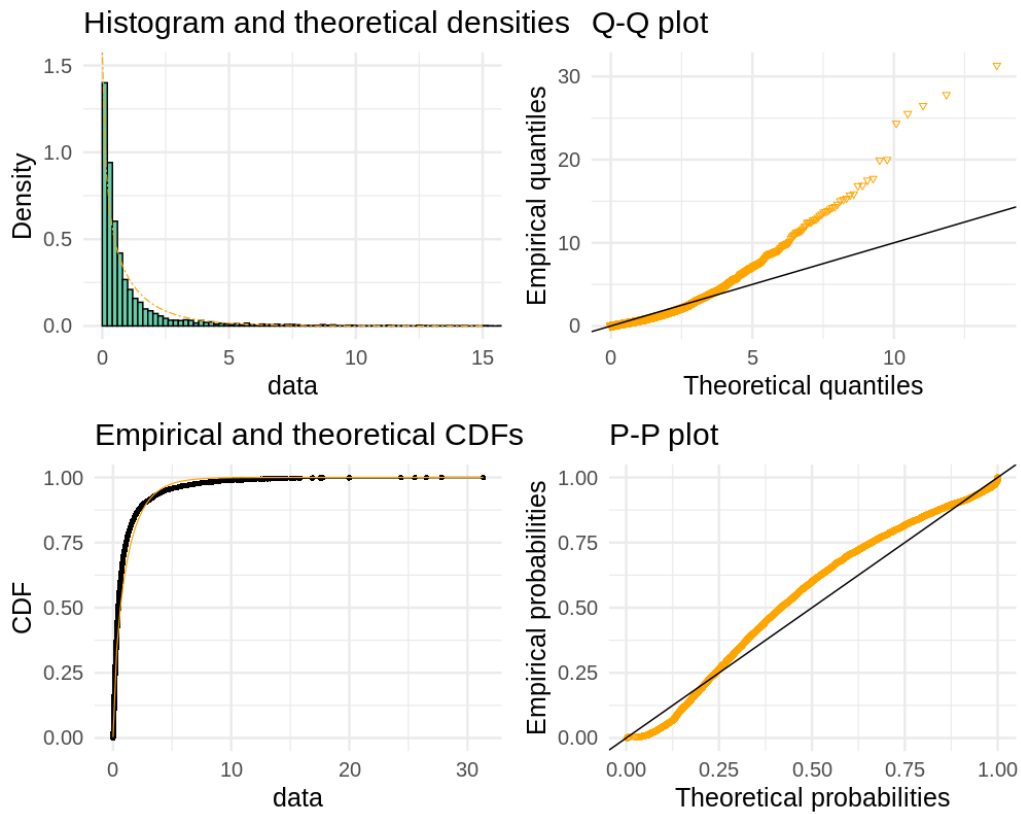


FIGURE 9.8: Fit of the interevent times of the aftershock sequence to the Gamma distribution. Top left: Density histogram of the data and fit to the Gamma PDF. Top right: quantile-quantile plot. Bottom left: Cumulative distribution function. Bottom right: P-P plot.

TABLE 9.6: Parameters of the Gamma distribution obtained by means of maximum likelihood estimation.

Parameters	estimate	Std. Error
shape	0.6581	0.0115
rate	0.5925	0.0149

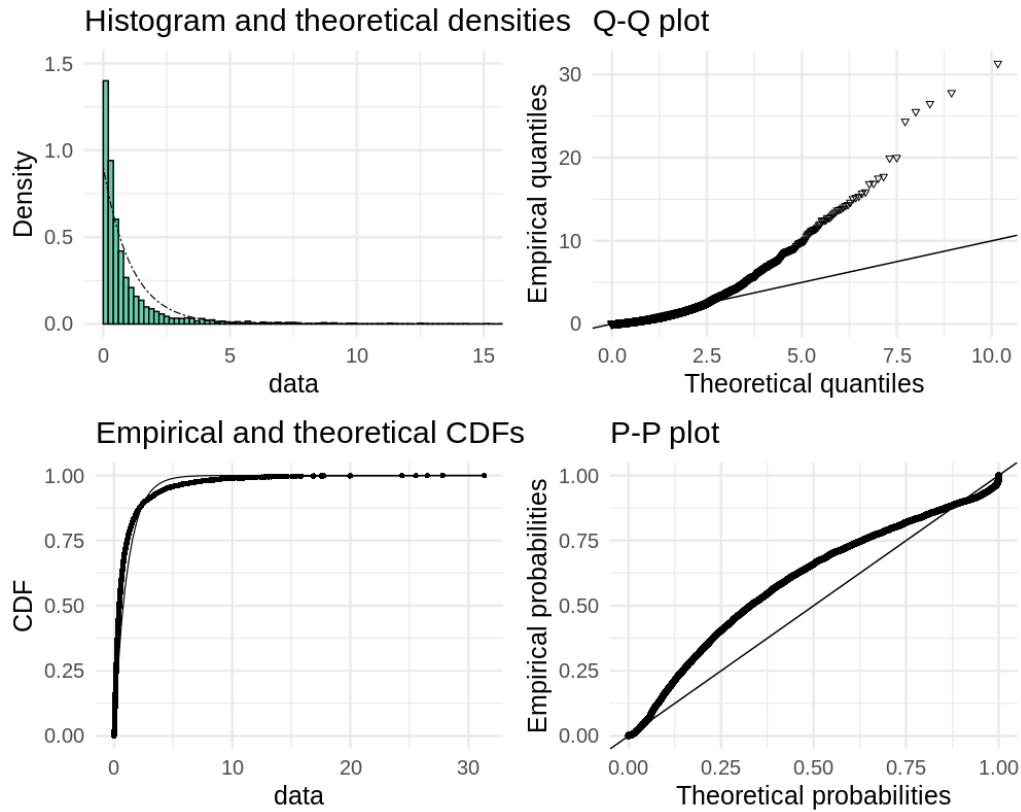


FIGURE 9.9: Fit of the interevent times of the aftershock sequence to the Exponential distribution. Top left: Density histogram of the data and fit to the Exponential PDF. Top right: quantile-quantile plot. Bottom left: Cumulative distribution function. Bottom right: P-P plot.

TABLE 9.7: Fitting of the Exponential distribution by means of maximum likelihood

Parameters	estimate	Std. Error
rate	0.9002	0.0131

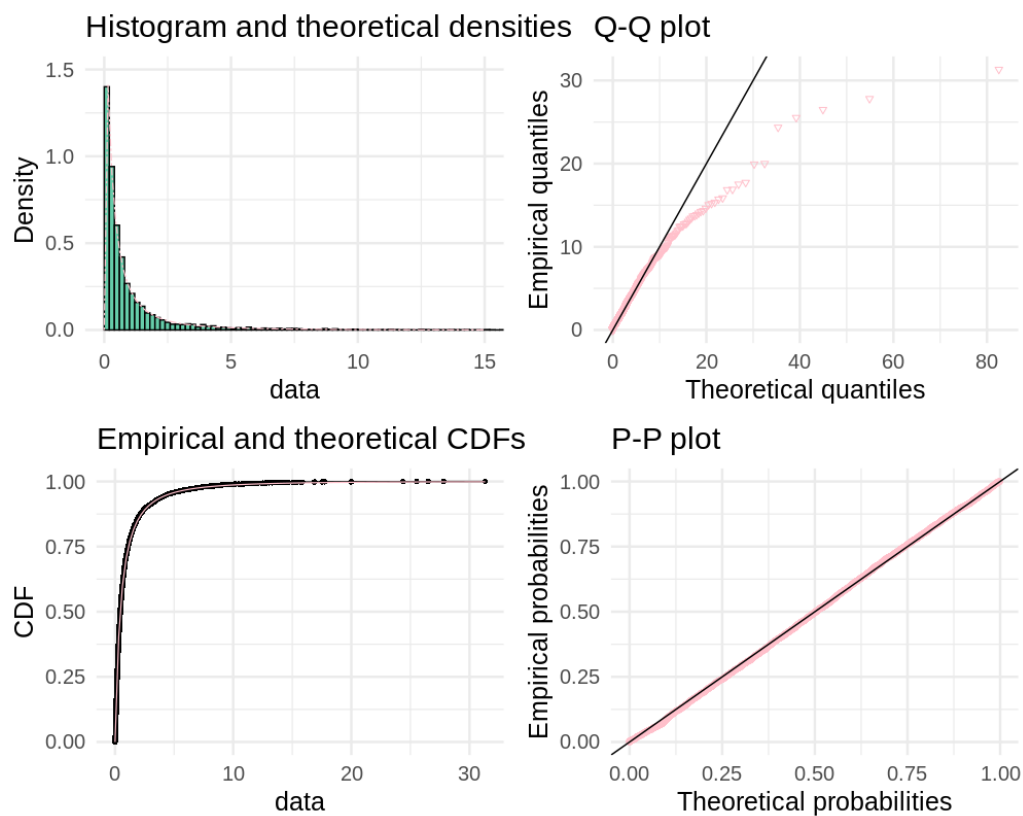


FIGURE 9.10: Fit of the interevent times of the aftershock sequence to the Lognormal distribution. Top left: Density histogram of the data and fit to the Lognormal PDF. Top right: quantile-quantile plot. Bottom left: Cumulative distribution function. Bottom right: P-P plot.

TABLE 9.8: Parameters of the Lognormal distribution estimated by means of maximum likelihood.

Parameters	estimate	Std. Error
Logarithmic mean	-0.8208	0.0206
Logarithmic standard deviation	1.4135	0.0146

Bibliography

- [1] V.D. Agou. Geostatistical Analysis of Precipitation on the island of Crete. Master's thesis, Technical University of Crete, 2016.
- [2] K. Aki. Maximum likelihood estimate of b in the formula $\log n = a - bm$ and its confidence limits. *Bulletin of the Earthquake Research Institute, Tokyo Univ.*, 43:237–239, 1965.
- [3] E.E. Alvarez. Estimation in Stationary Markov Renewal Processes, with Application to Earthquake Forecasting in Turkey. *Methodology and Computing in Applied Probability*, 03 2005.
- [4] P. Avramidis, G. Iliopoulos, K. Nikolaou, N. Kontopoulos, A. Koutsodendris, and G. Wijngaarden. Holocene sedimentology and coastal geomorphology of zakyntos island, ionian sea: A history of a divided mediterranean island. *Palaeogeography, Palaeoclimatology, Palaeoecology*, 09 2017.
- [5] P. Bhattacharya and J. Kayal. Mapping the b -value and its correlation with the fractal dimension in the northeast region of india. *Journal of the Geological Society of India*, 62:680–695, 12 2003.
- [6] P. Bormann, S. Wendt, and D. DiGiacomo. *Seismic Sources and Source Parameters*. Deutsches GeoForschungsZentrum GFZ, 2013.
- [7] L. Brillouin. The negentropy principle of information. *Journal of Applied Physics*, 24(9):1152–1163, 1953.
- [8] M. Båth. Earthquake energy and magnitude. *Physics and Chemistry of the Earth*, 7:115 – 165, 1966.
- [9] S. Castellaro, F. Mulargia, and Y. Y. Kagan. Regression problems for magnitudes. *Geophysical Journal International*, 165(3):913–930, 06 2006.
- [10] J. P. Chilès and P. Delfiner. *Geostatistics: Modeling Spatial Uncertainty*. Wiley series in probability and statistics. Wiley, New York, 2nd edition, 2012.
- [11] D. Chorozoglou and E. Papadimitriou. Investigation of earthquake recurrence networks: the cases of 2014 and 2015 aftershock sequences in ionian islands, greece. *Natural Hazards*, 04 2020.

- [12] P. Comninakis, J. Drakopoulos, G. Moumoulidis, and B. Papazachos. Foreshock and aftershock sequences of the cremasta earthquake and their relation to the waterloading of the cremasta artificial lake. *Annals of Geophysics*, 21:39–71, 06 1968.
- [13] S. Crampin and Y. Gao. The physics underlying gutenbergrichter in the earth and in the moon. *Journal of Earth Science*, 26:134–139, 02 2015.
- [14] T. J. Diccio and B. Efron. Bootstrap confidence intervals. *Statistical Science*, 11(3):189–212, 1996.
- [15] A. M. Dziewonski, T.A. Chou, and J. H. Woodhouse. Determination of earthquake source parameters from waveform data for studies of global and regional seismicity. *Journal of Geophysical Research: Solid Earth*, 86(B4):2825–2852, 1981.
- [16] D. A. Freedman. *Statistical Models: Theory and Practice*. Cambridge University Press, 2 edition, 2009.
- [17] S. Gennady. *Seismic Quiescence and Activation*, pages 1178–1184. Springer Netherlands, Dordrecht, 2011.
- [18] A. V. Guglielmi. Omori’s law: a note on the history of geophysics. *Physics-Uspekhi*, 60(3):319–324, mar 2017.
- [19] B. Gutenberg. Amplitudes of surface waves and magnitudes of shallow earthquakes. *Bulletin of the Seismological Society of America*, 1945.
- [20] B. Gutenberg and C. F. Richter. Frequency of earthquakes in California. *Bulletin of the Seismological Society of America*, 34(4):185–188, 10 1944.
- [21] S. Hainzl and Y. Ogata. Detecting fluid signals in seismicity data through statistical earthquake modeling. *Journal of Geophysical Research: Solid Earth*, 110(B5), 2005.
- [22] T. C. Hanks and H. Kanamori. A moment magnitude scale. *Journal of Geophysical Research: Solid Earth*, 1979.
- [23] F. Hayashi. *Econometrics*. 2000.
- [24] Hellenic Statistical Authority. Estimated population on the 1st january for the years, hellas total, region, departments (2002 - 2019), 2020.
- [25] A. Helmstetter, Y. Kagan, and D. Jackson. Comparison of short-term and time-independent earthquake forecast models for southern california. *Bulletin of the Seismological Society of America*, 96:90–106, 03 2006.
- [26] A. Helmstetter and D. Sornette. Bath’s law derived from the gutenbergrichter law and from aftershock properties. *Geophysical Research Letters*, 30(20), 2003.

-
- [27] D. T. Hristopulos and V. Mouslopoulou. Strength statistics and the distribution of earthquake interevent times. *Physica A: Statistical Mechanics and its Applications*, 392(3):485–496, Feb 2013.
- [28] IASP. International Association of Seismology and Physics of the Earth’s Interior, 2019.
- [29] IRIS. Education and outreach series no. 3, 2019.
- [30] E.H. Isaaks and R.M. Srivastava. *Applied Geostatistics*. Oxford University Press, 1989.
- [31] N. L. Johnson, S. Kotz, and N. Balakrishnan. Lognormal distributions. *New York: John Wiley and Sons*, 11(3), 1994.
- [32] Y. Kagan. Short-term properties of earthquake catalogs and models of earthquake source. *Bulletin of the Seismological Society of America California Kern County Joshua Tree–Landers–Big Bear sequence*, 94:1207–1228, 09 2004.
- [33] H. Kanamori. The energy release in great earthquakes. *Journal of Geophysical Research (1896-1977)*, 82(20):2981–2987, 1977.
- [34] H. Kanamori and Don L. Anderson. Theoretical basis of some empirical relations in seismology. *Bulletin of the Seismological Society of America*, 65(5):1073–1095, 10 1975.
- [35] Vassilis Karakitsios. Western greece and ionian sea petroleum systems. *AAPG Bulletin*, 97, 09 2013.
- [36] C. Karakostas, K. Konstantinidou, V. Lekidis, K. Makra, B. Margaritis, K. Morfidis, C. Papaioannou, E. Rovithis, T. Salonikios, and N. Theodoulidis. Ionian sea earthquake 6.8 M on 25/10/2018 strong ground motion and effects on soil and built environment. 11 2018.
- [37] I. G. Kassaras and V. Kapetanidis. *Resolving the Tectonic Stress by the Inversion of Earthquake Focal Mechanisms. Application in the Region of Greece. A Tutorial*, pages 405–452. Springer International Publishing, Cham, 2018.
- [38] A. Katsuyuki. Magnitude, seismic moment and apparent stress for major deep earthquakes. *Journal of Physics of the Earth*, 30(4):321–330, 1982.
- [39] A. Kiratzi. *Magnitude scales for earthquakes in the broader Aegean area*. PhD thesis, Ph. D. Thesis, 1984.
- [40] A. Kiratzi and E. Louvari. Focal mechanisms of shallow earthquakes in the aegean sea and the surrounding lands determined by waveform modelling: a new database. *Journal of Geodynamics*, 36(1):251 – 274, 2003. Active Faults: Analysis, Processes and Monitoring.

- [41] C. Lomnitz. Magnitude stability in earthquake sequences. *Bulletin of the Seismological Society of America*, 56(1):247–249, 02 1966.
- [42] J. S. Long and P. Trivedi. Some specification tests for the linear regression model. *Sociological Methods and Research - SOCIOLOGICAL METHOD RES*, 21:161–204, 11 1992.
- [43] A. MALLETT. A maximum likelihood estimation method for random coefficient regression models. *Biometrika*, 73(3):645–656, 12 1986.
- [44] K. Mallika, H. Gupta, D. Shashidhar, N. Rao, S. Rohilla, H. Satyanarayana, and D. Srinagesh. Temporal variation of b value associated with m greater and equal to 4 earthquakes in the reservoir-triggered seismic environment of the koyna–warna region, western india. *Journal of Seismology*, 17, 12 2012.
- [45] E Marekova. Analysis of the spatial distribution between successive earthquakes occurred in various regions in the world. *Acta Geophysica*, 62, 12 2014.
- [46] Mercalli. Modified Mercalli intensity scale.
- [47] A. Mignan, M. J. Werner, S. Wiemer, C. Chen, and Y. m. Wu. Bayesian estimation of the spatially varying completeness magnitude of earthquake catalogs. 2011.
- [48] Y. Motoya. Aftershock sequence of the earthquake east off hokkaido on august 12, 1969. *Geophys. Bull. Hokkaido Univ.*, 24:93–106, 1970.
- [49] V. Mouslopoulou, G.M. Bocchini, S. Cesca, V. Saltogianni, J. Bedford, G. Petersen, M. Gianniou, and O. Oncken. Earthquake-swarms, slow-slip and fault-interactions at the western-end of the 1 hellenic subduction system precede the mw 6.9 zakyntos earthquake, greece. 2020.
- [50] K. Z. Nanjo, B. Enescu, R. Shcherbakov, D. L. Turcotte, T. Iwata, and Y. Ogata. Decay of aftershock activity for japanese earthquakes. *Journal of Geophysical Research: Solid Earth*, 112(B8), 2007.
- [51] C. Narteau, S. Byrdina, Peter Shebalin, and Danijel Schorlemmer. Common dependence on stress for the two fundamental laws of statistical seismology. *Nature*, 462:642–5, 12 2009.
- [52] UW News. Documents that Changed the World: Charles Richter’s seismic scale, 1935, 2019.
- [53] NOA. National Observatory of Athens, NOA, 2019.
- [54] Y. Norio. Space and time distributions of aftershocks. *Journal of Physics of the Earth*, 16(Special):63–80, 1968.

- [55] P. Nuannin, O. Kulhanek, and L. Persson. Spatial and temporal b value anomalies preceding the devastating off coast of nw sumatra earthquake of december 26, 2004. *Geophysical Research Letters*, 32(11), 2005.
- [56] Y. Ogata and Koichi Katsura. Analysis of temporal and spatial heterogeneity of magnitude frequency distribution inferred from earthquake catalogs. *Geophysical Journal International*, 113:727 – 738, 04 2007.
- [57] T. Omi, Y. Ogata, Y. Hirata, and K. Aihara. Estimating the etas model from an early aftershock sequence. *Geophysical Research Letters*, 41(3):850–857, 2014.
- [58] F. Omori. On the aftershocks of earthquakes. *Journal of the College of Science*, pages 1–107, 1894.
- [59] E. Papadimitriou, D. Gospodinov, V. Karakostas, and A. Astiopoulos. Evolution of the vigorous 2006 swarm in zakyntos (greece) and probabilities for strong aftershocks occurrence. *Journal of Seismology*, 17, 04 2013.
- [60] B. C. Papazachos, A. A. Kiratzi, and B. G. Karacostas. Toward a homogeneous moment-magnitude determination for earthquakes in Greece and the surrounding area. *Bulletin of the Seismological Society of America*, 87(2):474–483, 04 1997.
- [61] V. Papazachos, B. Papazachos, C. Papazachou, and K. Papazachou. *The Earthquakes of Greece*. Editions Ziti, 1997.
- [62] G. Pappas. On This Day August 12, 1953: Great Ionian Earthquake Devastates Western Greece, 2019.
- [63] Xu Jiren Peng and Z. Zhao. Migration of early aftershocks following the 2004 Parkfield earthquake. *Nature Geoscience*, 2(12):877–881, December 2009.
- [64] Eugénie Pérouse, Michel Sébrier, R. Braucher, Nicolas Chamot-Rooke, Didier Boulès, Pierre Briole, D. Sorel, D. Dimitrov, and Stavros Arsenikos. Transition from collision to subduction in western greece: the katouna–stamna active fault system and regional kinematics. *International Journal of Earth Sciences*, 106, 06 2016.
- [65] C. F. Richter. An instrumental earthquake magnitude scale. *Bulletin of the Seismological Society of America*, 25(1):1–32, 1935.
- [66] C. F. Richter. Elementary seismology. page 768, 1958.
- [67] E. C. Sanchez and P. Vega-Jorquera. Modelling temporal decay of aftershocks by a solution of the fractional reactive equation. *Applied Mathematics and Computation*, 340:43 – 49, 2019.

- [68] O. Schabenberger and C.A. Gotway. *Statistical methods for spatial data analysis*. Chapman and Hall. CRC Texts in Statistical Science. CRC Press, 2004.
- [69] C. H. Scholz. The frequency-magnitude relation of microfracturing in rock and its relation to earthquakes. *Bulletin of the Seismological Society of America*, 1968.
- [70] A. Serpetsidaki, E. Sokos, G.-A. Tselentis, and J. Zahradnik. Seismic sequence near zakynthos island, greece, april 2006: Identification of the activated fault plane. *Tectonophysics*, 480(1):23 – 32, 2010.
- [71] B. E. Shaw. Generalized omori law for aftershocks and foreshocks from a simple dynamics. *Geophysical Research Letters*, 20(10):907–910, 1993.
- [72] Significant Earthquake Database. List of earthquakes in greece, 2020.
- [73] E. Sokos, F. Gallovič, Christos P. Evangelidis, A. Serpetsidaki, J. Plicka, V. and Kostelecký, and J. Zahradník. The 2018 Mw 6.8 Zakynthos, Greece, Earthquake: Dominant Strike-Slip Faulting near Subducting Slab. *Seismological Research Letters*, 91(2A):721–732, 01 2020.
- [74] B. Sullivan and Z. Peng. Basic Statistical Seismology, 2019.
- [75] V. Tobyáš and R. Mittag. Local magnitude, surface wave magnitude and seismic energy, 2019.
- [76] H. Tomohiro, A. Takuma, and A. Yoji. The weibull–log weibull transition of the interoccurrence time statistics in the two-dimensional burridge–knopoff earthquake model. *Physica A: Statistical Mechanics and its Applications*, 388(4):483 – 490, 2009.
- [77] USGS. Search earthquake catalog (DYFI), 2019.
- [78] T. Utsu, Y. Ogata, Ritsuko S., and Mutsaers. The centenary of the omori formula for a decay law of aftershock activity. *Journal of Physics of the Earth*, 43(1):1–33, 1995.
- [79] Hal R. Varian. Bootstrap tutorial. *Mathematica Journal*, 9(3):27, 2004.
- [80] W. Feller V.Feller. *An Introduction to Probability Theory and Its Applications methods for spatial data analysis*. 1957.
- [81] S. Wiemer and M. Wyss. Mapping the frequency-magnitude distribution in asperities: An improved technique to calculate recurrence times. *Journal of Geophysical Research: Solid Earth*, 102(B7):15115–15128, 1997.
- [82] S. Wiemer and M. Wyss. Minimum magnitude of completeness in earthquake catalogs: Examples from alaska, the western united states, and japan. *Bulletin of the Seismological Society of America*, 90:859–869, 09 2000.

-
- [83] J. Woessner and S. Wiemer. Assessing the quality of earthquake catalogues: Estimating the magnitude of completeness and its uncertainty. *Bulletin of the Seismological Society of America*, 95:684–698, 05 2005.
- [84] Max Wyss, Akira Hasegawa, Stefan Wiemer, and N. Umino. Quantitative mapping of precursory seismic quiescence before the 1989, m 7.1 off-sanriku earthquake, japan. *Annali di Geofisica*, 42, 10 1999.
- [85] Matsumura K. Zhao Z., Qike K. and Peng Xu Jiren. p values of continental aftershock activity in China. *Acta Seismologica Sinica*, 5, 11 1992.
- [86] J. Zhuang, S. Werner, D. Hainzl, and S. Zhou. Basic models of seismicity: spatiotemporal models. *Community Online Resource for Statistical Seismicity Analysis*, 2011.